Filipa Alexandra Grifo Cunha

Graduate in Mechanical Engineering Sciences

High strain rate identification of *Pinus pinaster* Ait. on the transverse plane by the image-based inertial impact test

Dissertation submitted in partial fulfillment
of the requirements for the degree of

Master of Science in
Mechanical Engineering

Adviser: Prof. Doutor José Manuel Cardoso Xavier,
Assistant professor,
Universidade Nova de Lisboa

Co-adviser: Prof. Doutor Rui Fernando dos Santos Pereira Martins,
Assistant professor,
Universidade Nova de Lisboa

Examination Committee

Chair: Prof. Doutor António José Freire Mourão
Rapporteur: Prof. Doutor João Mário Burguete Botelho Cardoso

FACULDADE DE
CIÊNCIAS E TECNOLOGIA
UNIVERSIDADE NOVA DE LISBOA

September, 2019

High strain rate identification of *Pinus pinaster* Ait. on the transverse plane by the image-based inertial impact test

This document was created using the (pdf)LaTeX processor, based on the "novathesis" template[1], developed at the Dep. Informática of FCT-NOVA [2].
[1] https://github.com/joaomlourenco/novathesis [2] http://www.di.fct.unl.pt

Aos meus pais e à minha irmã.

Acknowledgements

Em primeiro lugar, gostaria de agradecer ao meu orientador, professor José Xavier, pela sugestão do tema, pela ajuda e pelo conhecimento transmitido. E gostaria também de agradecer ao meu co-orientador, professor Rui Martins, por toda a orientação.

Quero agradecer ao professor Fabrice Pierron e a toda a equipa da Universidade de Southampton pela realização dos ensaios experimentais que integram esta dissertação.

Agradeço à Faculdade de Ciências e Tecnologia da Universidade Nova de Lisboa pela formação e por todos os conhecimentos que adquiri neste trabalho, bem como em todo o curso.

Gostaria de agradecer aos meus colegas toda a ajuda que me deram ao longo dos 5 anos de curso.

Agradeço aos meus amigos que me acompanharam ao longo deste percurso todo o apoio e amizade. Em especial, ao meu namorado pelas palavras de carinho e motivação.

Por fim, um grande agradecimento aos meus pais e à minha irmã, por me terem apoiado, motivado e ajudado neste percurso. Obrigada por acreditarem em mim. Sem vocês nunca teria conseguido.

"Grandes batalhas só são dadas a grandes guerreiros."
Mahatma Gandhi

Abstract

Computer-aided engineering systems typically rely on constitutive models and material parameters to describe the mechanical behaviour of material over a spectrum of high strain rate regimes. The constitutive parameters are to be determined experimentally by suitable test methods. At high strain rate regimes, a few test methods have been proposed, with advantages and drawback. More recently, an image-based inertial impact (IBII) test was proposed to overcome limitation of quasi-static stress equilibrium (neglecting inertia effects) and 1D wave propagation theory (neglecting dispersion effects) of the classical split-Hopkinson pressure bar (SHPB) test. This dynamic test rely on full-field deformation measurements provided by an optical technique and ultra high speed imaging to resolve both spatial and temporal resolutions.

Wood and wood-based products are gaining momentum due to policies of sustainability and green economy. The extension of using such materials under a higher strain rate regimes would be therefore of interest in engineering applications.

This work aims the identification of linear elastic constitutive parameters of *Pinus pinaster* Ait. (maritime pine) wood subjected to high strain rates, using the image-based inertial impact test. In this dynamic test, images of specimen deformation are recorded by means of an ultra high speed camera. The recorded images are processed by the grid method yielding displacement fields over the whole external surface of the specimen. Through the displacements field, the strain and acceleration fields are reconstructed, respectively, by means of spatial and temporal derivations. By using the virtual fields method (VFM), it is possible to identify the constitutive parameters of wood. This characterisation is performed without measuring external forces applied to the specimen under study by selecting VFM admissible virtual fields. This is performed using acceleration fields as a load cell, thereby taking advantage of the non-negligible inertial forces introduced during the dynamic test.

In this work, two experimental analyses are carried out on *Pinus pinaster* Ait. species by using specimens oriented on the *RT* (Radial-Tangential) and *TR* (Tangential-Radial) planes. Data from the experimental tests are further processed by the VFM to identify properties such as Young's modulus (E) and Poisson's coefficient (ν) of the material under study. In this analysis an approximation was performed, having been considered an isotropic constitutive model in the VFM, since the *RT* and *TR* planes have a low anisotropy ratio. In this study, the stiffness components (Q_{xx} and Q_{xy}) of the material were determined, with average values of 2.23 GPa and 0.80 GPa, respectively, for the *RT* specimens. Similarly, the average values for the stiffness components (Q_{xx} and Q_{xy}) are 0.98 GPa and 0.80 GPa for the *TR* specimens. These dynamic elastic parameters are of the same order of magnitude of quasi-static references values. Therefore, it may be concluded that high strain rate loading has a non significant influence on the elastic transverse properties of for the *Pinus pinaster* Ait. species. Taking into account the advent of

digital technology, the image-based inertial impact test may become a conventional test method to study the materials properties of structural engineering when subjected to high strain rate loads.

Keywords: Image-based inertial impact test, Grid method, High strain rate testing, Virtual Fields Method, Wood, Dynamic behaviour.

Resumo

Os sistemas de engenharia assistida por computador geralmente contam com modelos constitutivos e parâmetros do material para descrever o comportamento mecânico do material num espectro de regimes de elevadas taxas de deformação. Os parâmetros constitutivos devem ser determinados experimentalmente por métodos de ensaio adequados. Em regimes de elevadas taxas de deformação, alguns métodos de ensaio foram propostos, com vantagens e desvantagens. Mais recentemente, um ensaio de impacto inercial foi proposto para superar a limitação do equilíbrio de tensão quase-estático (efeitos de inércia negligenciados) e a teoria de propagação de ondas unidimensionais (efeitos de dispersão negligenciadas) do teste clássico de barras de pressão de split-Hopkinson. Este ensaio dinâmico baseia-se em medições dos campos de deformações fornecidas por uma técnica óptica e por imagens de câmaras ultra-rápidas para resolver resoluções espaciais e temporais.

A madeira e os produtos à base de madeira estão a ganhar força devido a políticas de sustentabilidade e economia verde. A extensão do uso de tais materiais sob regimes de elevadas taxas de deformação seria, portanto, de interesse em aplicações de engenharia.

Este trabalho tem como objetivo a identificação de propriedades constitutivas da madeira de espécie *Pinus pinaster* Ait. (pinho marítimo), sujeita a elevadas taxas de deformação, utilizando o ensaio de impacto inercial. Neste ensaio experimental foram registadas imagens da deformação do provete por meio de uma câmara ultra-rápida. As imagens captadas foram posteriormente processadas pelo método das grelhas com a finalidade de serem obtidos os campos de deslocamentos na superfície do provete. Através do campo de deslocamentos determinaram-se os campos de deformações e de acelerações, mediante uma derivação espacial e uma derivação temporal de segunda ordem, respetivamente. Ao utilizar o método dos campos virtuais, é possível identificar os parâmetros constitutivos da madeira sem a medição de forças externas aplicadas no provete em estudo. Esta identificação é efetuada utilizando a aceleração como célula de carga, aproveitando deste modo as forças inerciais não desprezáveis do ensaio dinâmico.

Neste trabalho foram efetuadas duas análises experimentais com o propósito de estudar os parâmetros constitutivos de provetes da madeira de espécie de *Pinus pinaster* Ait. Os ensaios de impacto foram realizados em provetes com a orientação RT (Radial-Tangencial) e com orientação TR (Tangencial-Radial). Os dados provenientes dos ensaios experimentais foram posteriormente processados pelo método dos campos virtuais de forma a serem identificadas as propriedades, como o módulo de Young (E) e o coeficiente de Poisson (ν), do material em estudo. Nesta análise foi realizada uma aproximação, tendo sido considerado um modelo isotrópico e não ortotrópico no método dos campos virtuais, visto que os planos RT e TR apresentam um baixo rácio de anisotropia. Neste estudo foram determinadas as componentes da rigidez (Q_{xx} e Q_{xy}) do material, apresentando valores médios de 2,23 GPa e 0,80 GPa, respetivamente, para os provetes

orientados segundo o plano RT. Do mesmo modo, para os provetes orientados segundo o plano TR, os valores médios para as componentes da rigidez (Q_{xx} e Q_{xy}) são 0,98 GPa e 0,80 GPa.

Esses parâmetros dinâmicos elásticos são da mesma ordem de magnitude que os valores de referência quase-estáticos. Portanto, conclui-se que o carregamento a elevadas taxas de deformação não tem influência significativa nas propriedades transversais elásticas da madeira de *Pinus pinaster* Ait. Considerando o advento da tecnologia digital, o ensaio de impacto inercial pode-se tornar um método de ensaio convencional para estudar as propriedades dos materiais da engenharia estrutural quando submetidos a elevadas taxas de deformação.

Palavras-chave: Ensaio de impacto inercial, Método das grelhas, Elevadas taxas de deformação, Método dos Campos Virtuais, Madeira, Comportamento dinâmico.

Contents

List of Figures

List of Tables

1 | Introduction

1.1 Background

Materials used for structural engineering purposes are subjected to different deformation rates. When subjected to impact, collision or explosion, they are exposed to high strain rates. Therefore, it is important to characterize materials subject to high strain rates as they have a variety of applications, namely in the aeronautical industry, marine shipping, as well as in construction, manufacturing processes and military applications. However, characterizing the behaviour of materials and identifying their properties at high strain rates demonstrate several experimental difficulties. To obtain the constitutive parameters of a material it is necessary to perform experimental tests (Meyers, 2007).

Experimental test methods are carried out at specific strain rates, which refers to the maximum strain value achieved during the test (Ramesh, 2008). Some of the experimental tests used to characterize materials at various strain rates are servo hydraulic testing machine, pressure-shear plate impact and Split-Hopkinson pressure bar.

The quasi-static behaviour of materials has been extensively studied to determine parameters governing the constitutive models for this regime of strain rate. However, data at the high strain rate regimes is more scarce and less consensual. The dynamic behaviour involves inertia effects and load measurements which are more difficult to measure experimentally.

A few test methods have been proposed to address the dynamic mechanical behaviour of materials. Among them the gold standard is the SHPB. In this experimental test load cells are used to measure the force applied to the specimen and the associated strain rates (Zhu, 2015). This experimental test has some limitations that need to be addressed in order to have a more accurate characterization of materials.

Since many years ago, wood has been used by man as a building material. Today there are several utilities in engineering where this biological material is applied (Gibson and Ashby, 1999). Wood is a material that presents unusual characteristics such as anisotropy, variability and great heterogeneity (Kollmann and Côté, 1968). In order to use wood as a structural material, it is important to understand the constitutive properties of this material in its three orthonormal material planes (longitudinal, radial and tangential). Due to its characteristics of anisotropy and variability, conducting experimental tests on wood becomes an arduous task. When it comes to experimental tests at high strain rates, the difficulty of studying this material increases.

In recent years there has been an increase in studies using optical techniques to perform displacement and strain field measurements. This increase is due to the improved computing power and ultra high speed cameras available on the market. Digital image correlation and

the grid method are some of the existing optical techniques in the scientific community (Pierron and Forquin, 2012). In the 80s, optical techniques began to be used in more complex test configurations, as image processing made it possible to process experimental data more automatically. Prior to optical techniques, the processing of data obtained in experimental tests was done manually. These techniques could only provide quantitative measurements of stress and strain distributions from a limited number of points because of prolonged data collection procedures. Thus, these techniques were only used in specialized laboratories (Pierron and Grédiac, 2012). Such techniques have been piquing the interest of the scientific community of experimental mechanics as their potential is seen as revolutionary of experimental material testing. Optical techniques allow the fields of heterogeneous deformation to be obtained in a specimen, and after this analysis it is possible to obtain the constituent parameters of the material in a dynamic test.

Identification of the constituent properties of a material is achievable without measuring external forces applied to the specimen, however this type of process requires inverse techniques. The principle of virtual work was started to be used as a tool to identify the constitutive parameters of materials. Based on this, the virtual field method was used to identify material properties using acceleration as a load cell, thus taking advantage of inertial effects (Pierron et al., 2014). The virtual field method when compared to other inverse methods, such as the finite element model updating method, has a higher computational efficiency, as this technique does not require iterative resolutions (Pierron and Forquin, 2012).

In recent years, an effort has been made to study the effects of strain rates on metal properties, but studies of wood properties have been increasing as it has appeared as a structural material, replacing metal (Polocoser et al., 2017).

1.2 Objectives

The aim of this thesis is to identify the constitutive parameters of *Pinus pinaster* Ait. wood at high strain rates through the image-based inertial impact test. In this experimental and dynamic test, images of specimen deformation will be recorded through an ultra high speed camera. These images will be further processed by the grid method in order to obtain the displacement fields on the specimen surface. Subsequently, the strains and accelerations fields will be determined from the displacements fields, by means of a spatial derivation and a second order temporal derivation, respectively. The virtual fields method will allow to identify the constitutive parameters of the wood without measuring external forces applied to the specimen, using acceleration as a load cell. This will take advantage of the non-negligible inertial forces that exist in the dynamic test. The experimental results of the constitutive parameters will be compared with the reference values and later conclusions will be made about them. Figure 1.1 represents a flowchart of all the procedures and methodologies studied ih this thesis.

1.3 Structure

This thesis is divided into five chapters which are described below. In chapter 2 the theme of dynamic behaviour of materials will be presented. In this chapter will be describe some applications where materials are subjected to high strain rates when they are subjected to impact, collision or explosion. Next, some computer aided engineering systems and their application in some activities will be reported. The finite element method will be detailed as one of the most relevant

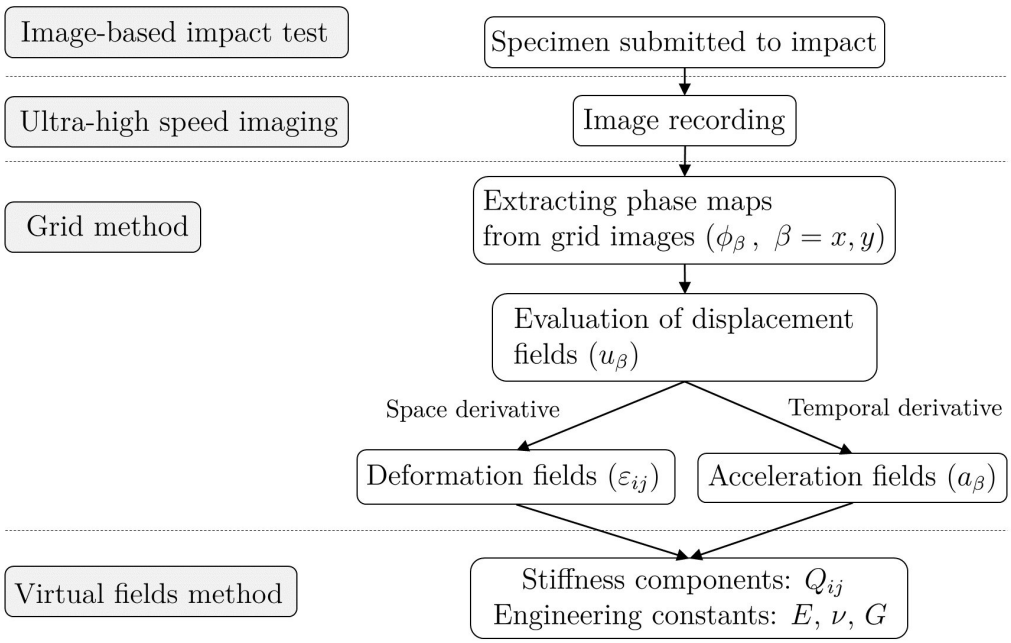

Figure 1.1: Flow chart of procedures and methodologies of this thesis.

CAE techniques. The experimental techniques and associated methodologies to characterize the materials in engineering will be characterized later. First, the servo hydraulic testing machine will be described, then the pressure-shear plate impact and then the split-hopkinson pressure bar. Moreover, emphasis will be given to the data reduction of the classical SPHB based on 1D ware propagation theory and strain gauge measurements to extract the stress-strain behaviour of the materials.

The chapter 3 will present the behaviour and structure of wood. The two types of wood species classifications will be compared to their internal structure: softwood and hardwood. More emphasis will be given to the softwood species as the wood under study, *Pinus pinaster* Ait., is classified as a softwood species. Since *Pinus pinaster* Ait. wood was selected for this study, more emphasis will be given to the softwood species. The macroscopic and microscopic structure of the softwood species will be described, as well as the orthogonal directions and the respective orthogonal planes. Finally, the literature on the dynamic behaviour of wood at intermediate strain rate testing, transverse impact and longitudinal impact at high strain rates will be reviewed.

The chapter 4 will expose the methodologies studied and used in this work. Initially, the image-based inertial impact test will be described as an alternative test to SHPB, in order to determine the dynamic behaviour of materials when subjected to high strain rates. Next, the optical grid method will be presented, in which the principle and grid transfer techniques are emphasized. Next, an optical technique, the grid method, will be presented which will detail the process of elaborating the grid pattern. Ultra high speed cameras will be referred to in this chapter as the sensors used to capture images in the IBII test. Next, will be characterized the ultra high speed camera used in the dynamic test under study. To end with, the VFM will be presented as an inverse method for the extraction of dynamic elastic properties from full-field deformation measurements. The principle of virtual works will be stated as the principle which the method of

virtual fields is based. The constitutive equation for materials with a linear elastic behaviour will be demonstrated. It will be explained how it is possible to use acceleration as a load cell without having to measure applied external loads. Finally, the virtual field method will be developed using the inertial forces, in order to demonstrate the identification of the constituent parameters for an isotropic material and an ortotropic material.

The chapter 5 describes the experimental analysis of the image-based inertial impact test. Two experimental tests will be made in which the specimen has different orientations, RT plane orientation and TR plane orientation. For both experimental tests, the maps of the displacement x and y components, the acceleration x and y components, and the strain x, xy and y components will be presented. The results obtained for the constitutive parameters of the *Pinus pinaster* ait. wood for the different specimens analysed will be exposed and compared with the reference values. Finally, the results obtained for both experimental analyses and conclusions will be discussed.

The chapter 6 will present the conclusions of this thesis and some possible future works.

2 Dynamic impact behaviour of materials

2.1 Introduction

In this chapter, a review on the dynamic impact behaviour of engineering materials is presented. Both numerical and experimental approaches are considered. In particular, the experimental techniques typically used for studying the impact behaviour of materials are summarised, emphasising their application, assumptions and current limitations. Firstly, the materials behaviour at high strain rates is mentioned, emphasizing CAE systems and numerical simulation. Following, some experimental techniques are specified, such as servo hydraulic testing machine, pressure-shear plate impact and split-hopkinson pressure bar.

2.2 Material behaviour at high strain rates

In various engineering fields, materials can be submitted to high strain rate deformations when subject, for instance, to impact, collision or explosion. Some industrial applications are listed as follows:

(i) Infrastructures and transports: Infrastructures such as power stations, large buildings, dams, bridges, must be designed to withstand natural disasters or explosions; transports must be design to sustain a certain level of dynamic impact.

(ii) Manufacturing processes: knowledge of the mechanical behaviour of materials when subjected to high deformation rates is essential to improve manufacturing processes in order to reduce costs and improve quality.

(iii) Civil and military applications: for the design of infrastructures and vehicles subjected to impact, as in an effective shielding project it becomes necessary to know the behavior of the materials at high deformation rates.

Therefore, it is fundamental to address the behaviour of materials at high rate strain regimes, both computationally and experimentally.

2.2.1 Numerical modelling

Computer Aided Engineering (CAE) deals with the use of computer programs to improve product design as well as to solve engineering problems in a wide range of industries (SIEMENS,

2018). CAE systems had been introduced in early stages of computers since 1950. In 1960, companies introduced a system that used the computer to monitor a large number of logic diagrams before the emergence of integrated circuits. At that stage, the term Design Automation or Automated Design was coined. In the same decade, interactive graphics were then developed, giving rise to the designation of Computer Aided Design (CAD) systems. With progressive computer hardware improvements and theoretical consolidation of numerical algorithms, the second and third generation of CAE systems were developed. However, the effective utilization of such computer-based systems into the industry was relatively slow, considering the high prices of computer components at the time. It was not until the end of 1960 that CAE systems grew, due to the decline in computer hardware costs and the advent of minicomputer (Green, 1983). In engineering, generically, the CAE systems are applied in several activities, namely:

(i) Structural, thermal, kinematic, dynamic analysis, vibrations and electromagnetic, using the Finite Element Analysis (FEM).

(ii) Acoustic analysis using the FEM or the Boundary Element Method.

(iii) Analysis of control systems.

(iv) Fluid and thermodynamics analysis using Computational Fluid Dynamics (CFD).

(v) Analysis of mechatronic systems.

(vi) Simulation of manufacturing processes.

CAE systems have several advantages, namely the reduction of cost and time for manufacturing and product development. Research and technological development activities are able to perform numerical simulations with CAE systems, reducing the number of prototypes and experimental tests, mitigating costs and time (SIEMENS, 2018).

The FEM is one of the fundamental techniques of CAE. This method consists, in brief, of modelling and analysing a problem of a continuous medium through several discrete elements. The governing partial differential equations (equilibrium equations, strain-displacement relationships, compatibility equations, constitutive law) can then be solved for a finite number of kinematic or primary variables. It is necessary to specify the component geometry, the constitutive model of the materials and the boundary conditions of the problem (*i.e.* either prescribed displacements or applied tractions). The development of the FEM occurred in parallel to the evolution of CAE systems. The method was eventually established in the 1940's, when Richard Courant had proposed a discretization methodology for continuous elements. In the following decade, the triangle element was introduced, capable to analyse complex geometries with suitable accuracy if numerical convergence could be achieved. The term "Finite Element" arose in 1960, by Ray Clough. In the 1980s, geometry standards were developed through FEA and CAD; thus, the use of 2D drawing has progressed to the use of 3D modelling. Soon after the simulation appeared in 3D; the FEA was introduced in product designs. In the year 1990, the computer and these technologies became accessible in large scale to professional users.

The finite element method can be applied to the analysis and study of many diverse engineering phenomena and problems such as studying vibratory systems, analysing material behaviour, solving heat conduction problems and fluid mechanics, electricity and magnetism, impact, plastic

conformation of materials, metallic and non-metallic structures, dimensioning of large structures, hydrodynamics, aerodynamics, among others.

In the modelling of the behaviour of materials, the finite element method allows taking into account a wide variety of constitutive models, namely, linear elasticity (Hooke's law), plasticity, viscoplasticity, hyperplasticity, thermoelasticity, among others.

The finite element method, through numerical simulation, can identify and predict any design problems. When the material behaviour involves high strain rates, it implies the use of explicit algorithms in the finite element method, which is considered a non-linear analysis. Non-linear phenomena can exhibit three distinct types of behaviour, static, quasi-static or dynamic. The behaviour is said to be static when the load does not vary over time or when the load application time is gradual enough that the accelerations are small. A problem is called quasi-static when the inertial effect is negligible and its response varies over time as it does in static behaviour. Dynamic behaviour is characterized by having significant loading frequencies and inertial forces are not negligible. There are two types of problems of dynamic phenomena: wave propagation and structural dynamics. The wave propagation problem is associated with impact or collision phenomena, ie high frequency temporal phenomena and short analysis periods. The problem of structural dynamics is associated with situations of excitation frequencies of the order of the first natural frequency of the system (Teixeira-Dias et al., 2018).

The effective numerical simulation or prediction of CAE/FEM systems strongly rely on the constitutive models of the materials as well as their input mechanical parameters. These models must be able to simulate the material or structures behaviour for different loading scenarios. The mechanical properties of material are to be determined experimentally through suitable mechanical tests or techniques over a spectrum of strain rate regimes.

2.2.2 Experimental techniques

With the advent of computational mechanics, it is possible to perform increasingly precise numerical simulations of complex problems in engineering. However, it is necessary to validate these models, namely with respect to the constitutive laws and their material parameters. There are several techniques and methodologies associated with experimental mechanics for the characterization of engineering materials (Carlsson et al., 2014). They can be classified as a function of the strain rate at which load is applied, as shown in Figure 2.1 (Ramesh, 2008). The universal and servo-hydraulic test machines allow to perform quasi-static mechanical tests and moderate strain rate tests up, to the order of 200 s^{-1}. Above 10^2 s^{-1}, the inertial effects and acceleration must be taken into account in the material characterisation (Zhu and Pierron, 2016). In the following, the most relevant high strain rate techniques are reviewed with special emphasis to the classical split-Hopkinson pressure bar (SHPB) test and analysis (Chen and Song, 2011).

2.2.2.1 Servo hydraulic testing machine

In recent years servo hydraulic testing machine has become more common, as it has a range of approximately six orders of magnitude of strain rates (10^{-3} to 10^{+3} s^{-1}), as shown in figure 2.2 (Bardenheier and Rogers, 2006).

Servo hydraulic testing machine are used for various types of impact loads such as dynamic stresses, compression, bending or shear loads (Bardenheier and Rogers, 2006). Figure 2.3 is a diagram of the Instron VHS 1000 machine consisting of a typical servo hydraulic testing machine.

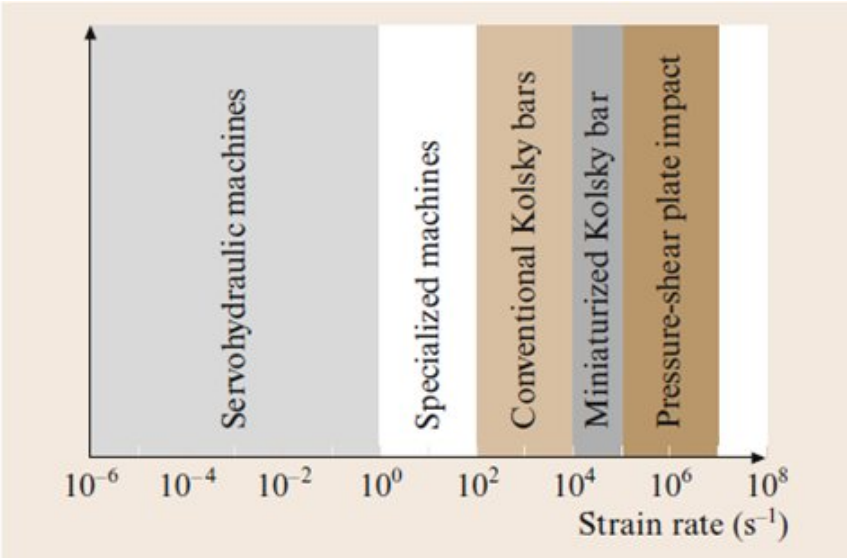

Figure 2.1: Experimental techniques as function of strain rate (Ramesh, 2008).

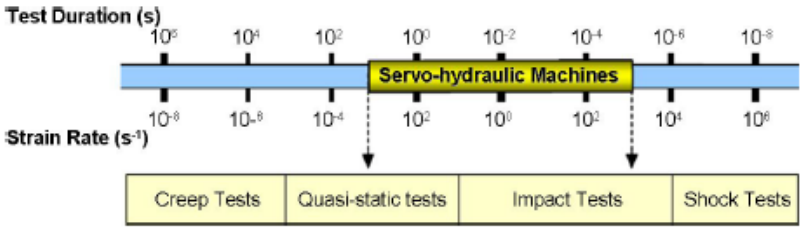

Figure 2.2: Test duration and strain rates for different tests (Longana, 2014).

This machine operates by accumulating oil at a pressure of 280 bars in a pressure cylinder controlled by a proportional valve. One of the advantages of servo hydraulic machines is that they can test materials from quasi-static to intermediate strain rates (Zhu, 2015).

Servo hydraulic testing machine allow the use of samples with dimensions similar to those used in quasi-static tests, thus allowing a suitable surface for full-field strain measurement techniques. With the development of ultra high speed cameras, it is possible to capture images with high temporal resolution during tests of intermediate strain rates, such as servo hydraulic testing machine.

2.2.2.2 Pressure-shear plate impact

The pressure-shear plate impact technique was developed to study the shear behaviour of materials subjected to high strain rates (10^5 to 10^7 s^{-1}). This test consists of the impact of two flat and parallel plates, as shown if figure 2.4. The specimen needs to be thin and flat, which is glued to the flyer. This plate is launched from a barrel of a gas gun towards the fixed plate. The plates may have different angles of incidence (Ramesh, 2008). The analysis of this test consists of measuring the velocity of free particles on the surface opposite the impact (Yuan et al., 2007).

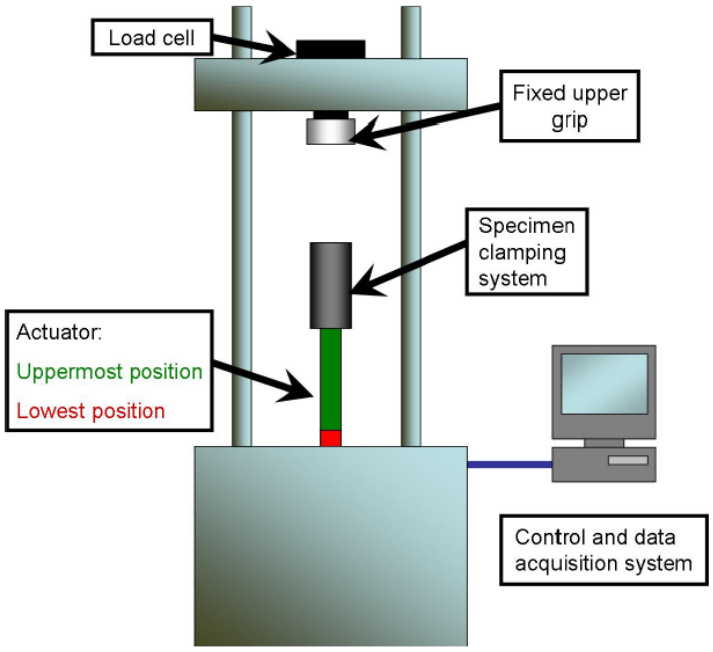

Figure 2.3: Instron VHS machine schematic (Longana, 2014).

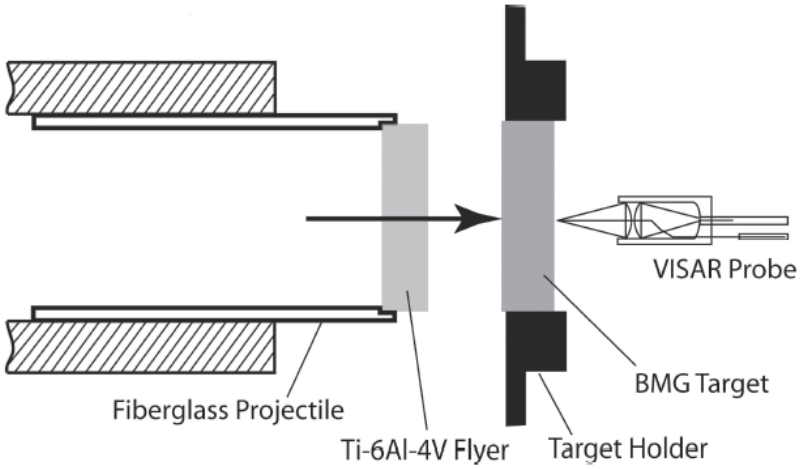

Figure 2.4: Schematic of the normal plate impact test (Yuan et al., 2007).

2.2.2.3 Split-Hopkinson pressure bar (SHPB)

The SHPB, or as it is also so called, the Kolsky bar, is the classical experimental test for material characterisation at high strain rate deformation (Chen and Song, 2011; Ramesh, 2008). The test was first developed in 1914 by Bertram Hopkinson to measure the elastic (stress) wave propagation in a metal bar. Later on, in 1949, Herbert Kolsky refined the original set-up by using two Hopkinson bars in series along with the sample, providing stress and strain measurements during the dynamic test. No recently, modifications were introduced allowing other loading configurations, in both tension and shear (Sudheera et al., 2018). The term SHPB is generally used when dealing with materials subjected to compression, whilst the term Kolsky bar can

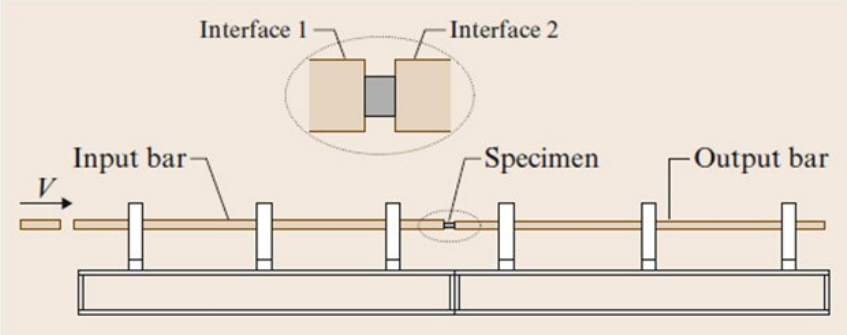

Figure 2.5: Schematic representation of the experimental technique of Split-Hopkinson pressure bar (Ramesh, 2008).

be more broadly used for compression, traction, shear or a combination among them (Ramesh, 2008).

In general, the SHPB test method is designed to achieve a uniform and uniaxial state of stress and strain on the specimen, so a direct or explicit identification can be proposed in the data reduction. The typical set-up is shown in Figure 2.5. This mechanical system consists of three slender cylindrical bars axially aligned with each other. The specimen of the material under analysis is sandwiched in between the so called incident (input) and transmitted (output) bars. The smallest bar, so called striker bar, is fired at the incidence bar at an initial velocity v_0, through a compressed gas gun (consisting of a reservoir of pressurized stored gas). This impact generates a stress wave that propagates along the bars deforming the specimen at a high strain rate. In general, the (striker, incident and transmitted) bars have the same diameter and are made of the same material (*i.e.* aluminium, steel, titanium). It is assumed that their mechanical behave is confined to the linear elastic domain during the impacted test, so no permanent deformation occurs (Ramesh, 2008). The lateral cross-section of the bars together with the specimen loading faces must have flatness and parallelism geometric tolerances and roughness approximating the perfect contact between both striker/incident bars and at the interfaces incident bar/specimen and specimen/transmitted bar. The bars are supported by bearings (to minimize friction effects) and must have coincident axes to ensure that wave propagation is one-dimensional (Chen and Song, 2011). Generally, the material of the bars has a higher stiffness and yield strength with regard to the specimen to be tested (Ramesh, 2008). The analysis of the test assumes that the specimen remain in contact with both the incident and transmitted bars during the period of the dynamic test, guaranteeing the continuity of the displacement field and axial stresses at the interfaces (Fletcher and Pierron, 2018).

The measurement system of the SHPB test consists essentially of two subsystems (Figure 2.5), one for measuring the velocity of the striker bar and another to measure the wave deformation travelling along the bars during the test. The strain signals over time are measured using one-element strain gauges glued at the surface of the incidence and transmission bars at given distance with regard to the interfaces incident bar/specimen and specimen/transmitted bar, so pulses (strain) signals can be perfectly distinguishable with no overlapping effects (Chen and Song, 2011; Meyers, 2007; Ramesh, 2008). Therefore, three pulses are typically recorded: the pulse generated by the projectile over the incident bar; the pulse reflected at the interface incident bar/specimen; and the pulse that is transmitted through the interface specimen/transmitted bar

(Ramesh, 2008). The strain gauge signals are properly amplified and conditioned before being stored in a computer for further data reduction.

On the analysis of the input pulse, created by the impact of the striker and incident bars at a given velocity v_0, it can conclude that two compressive waves are actually generated and propagate at constant speed c (where, $c = (E/\mu)^{-1}$ with E the Young's modulus and μ the bar density) as can be seen by the characteristic lines on the Lagrange diagram of figure 2.6a (Chen and Song, 2011; Meyers, 2007; Ramesh, 2008). On the one hand, a wave is generated which propagates in the incidence bar towards the x axis and, on the other hand, a wave is reflected and propagates in the impact bar in the negative direction of x. This latter wave reaches the free edge of the striker bar and suffers total reflection back in the positive direction of x as a tension wave at the end of the time given by (Figure 2.6a):

$$\Gamma = \frac{2L}{c} \tag{2.1}$$

where L is the length of the striker bar and c is a constant determined as a function of the density and Young's modulus of the bar material. This wave is continuing propagating in the incident bar, determining both the total duration (Γ) and extension (λ) of the input impulse measured by the strain gauge in the bar (Figure 2.6a):

$$\lambda = 2L \tag{2.2}$$

The amplitude of the wave generated on the incidence bar (incident wave) can be determined by applying the linear momentum conservation equation to the system consisting of the striker and incidence bars (Meyers, 2007):

$$\mu A L v_0 = \mu A \lambda v \tag{2.3}$$

in which A is the cross-section area of the bars and v is the velocity at positions: $ct < x < ct + \lambda$, when $t > \Gamma$. By replacing equation (2.2) into equation (2.4) it is conclude that:

$$v = \frac{v_0}{2} \tag{2.4}$$

Considering D'Alembert solution of the 1D wave equation (second-order linear partial differential equation representing the linear momentum equilibrium of the mechanical system) the strain and velocity fields are related by (Meyers, 2007):

$$\varepsilon(x,t) = -\frac{1}{c} v(x,t) \tag{2.5}$$

where $v(x,t)$ represent the position of a particle at position x in the instant t. Therefore, the strain-time signal recorded by the strain gauge mounted on the incident bar ($\varepsilon^I_{\mathrm{SG1}}$) can be obtained by replacing Eq. (2.4) in Eq. (2.6):

$$\varepsilon^I_{\mathrm{SG1}} = -\frac{v_0}{2c} \tag{2.6}$$

In the Lagrange wave propagation diagram for th SHPB set-up is schematically shown in figure 2.6b, neglecting the specimen dimensions (Chen and Song, 2011; Meyers, 2007; Ramesh, 2008). The strain-time signals are represented over time, where the incident strain is denoted by ε_I, the reflected strain by ε_R, and the transmitted strain is denoted by ε_T. The input stress wave

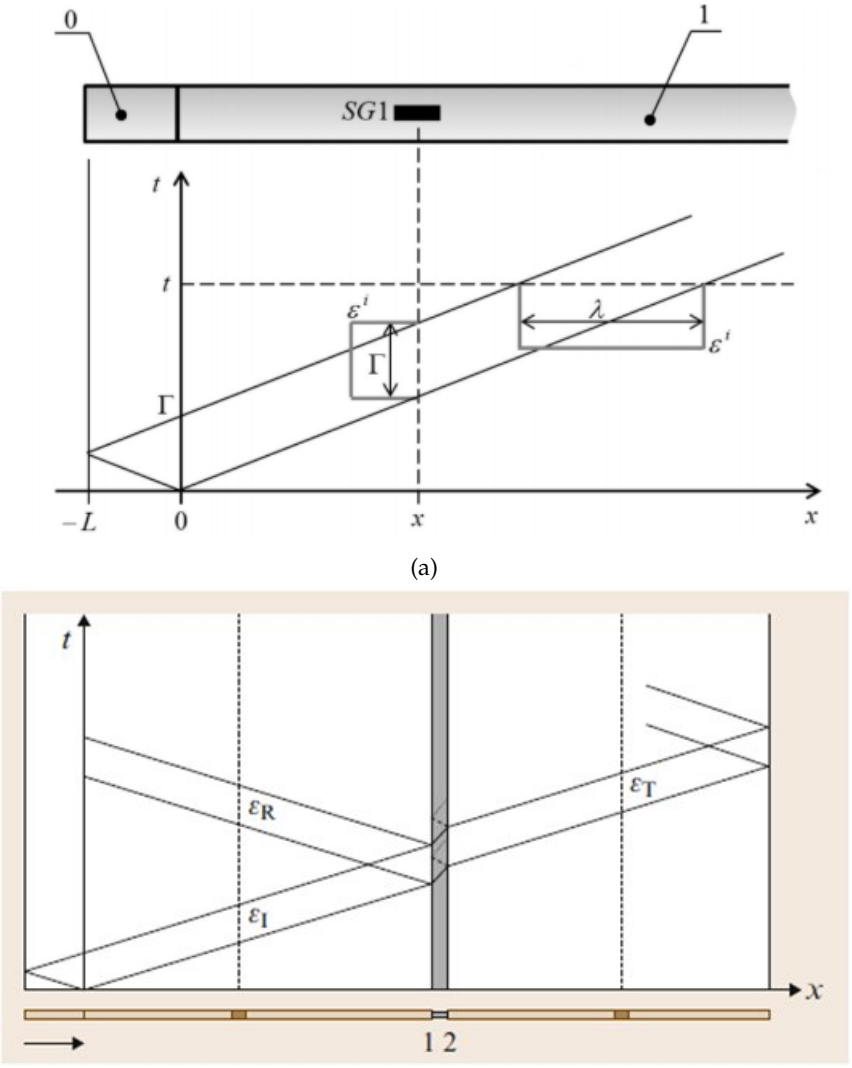

Figure 2.6: Lagrange diagrams: (a) just after the impact on the striker/incident bars; (b) through time and space in the experimental technique of split-Hopkinson pressure bar (Ramesh, 2008).

propagates through the incident bar until reaching the specimen. At the incident bar/specimen, the wave is split; one part is reflected (as a tensile wave propagating in the negative direction of x), since the impedance (geometry and properties) of the specimen (Z_p) is lower than the impedance of the incident bar (Z_I), *i.e.* $Z_p < Z_I$, and another part is transmitted through the specimen. The partially reflected wave is recorded by the strain gauge at the incident bar as a tensile pulse. The transmitted wave, on the other hand, reaches the interface specimen/transmitted bar. Here the wave suffers a similar dispersion behaviour. The assumption of quasi-static stress equilibrium assumes that the stress wave reverberates multiple times at the specimen interfaces with the bars until acceleration is damped out, loading the specimen in compression at high strain rates. Therefore, inertial effects can be neglected in the data reduction. The wave is transferred to the transmitted bar as a compression impulse sine $Z_p < Z_T$ (where Z_T represents the impedance of the transmitted bar). This impulse is recorded by the strain gauge bounded on the transmitted bar. Figure 2.7 shows an example of the strain signals usually recorded on the input and output

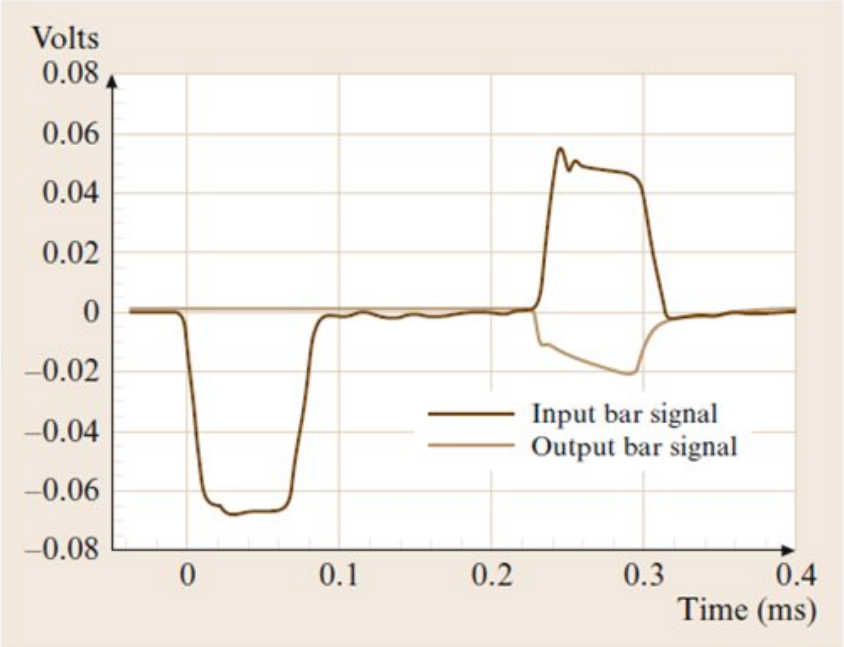

Figure 2.7: Signals usually recorded on strain gauges on the input bar and output bar (Ramesh, 2008).

bars strain gauges.

The analysis of the SHPB assumes that the compressive impulse generated by the striker bar is one-dimensional along the longitudinal axis. The 1D wave propagation theory is therefore proposed as data reduction. In other words, no dispersion of the pulse signal is accounted for. This assumption is never fully achievable in practice and the pulse signals can present therefore osculations (dispersion effects). In order to mitigate this issue, pulse shaping techniques have been proposed (Koerber et al., 2010). On the other hand, the size of the specimen is very short with regard to the length of the bars to ensure the condition of quasi-static equilibrium (Meyers, 2007).

The strain-time impulse signals measured during the impacted test by the two linear strain-gauges, fixed to the incident and transmitted bars, are the basic experimental data measured for the SHPB analysis. The dynamic stress–strain response of the specimen can then be evaluated from these measurements (the incident, the reflected, and the transmitted strain-time pulses). Let's start by analysing the velocity of a particle at the interface incident bar/specimen ($x = 0$) given by the contribution of both incident and reflected waves:

$$v(0,t) \equiv v_1(t) = v^I(0,t) + v^R(0,t) = c[\varepsilon^R(t) - \varepsilon^I(t)] \tag{2.7}$$

In turn, the velocity of a particle at the interface specimen / transmitted bar ($x = L_s$, where L_s is the initial, undeformed length of the specimen) can be obtained by:

$$v(L_P,t) \equiv v_2(t) = -c\varepsilon^T(t) \tag{2.8}$$

Therefore, taking into account mean velocity and considering the linear deformation measure of

the strain, the following expression for the strain rate can be obtained:

$$\dot{\varepsilon}(t) = \frac{\mathrm{d}\varepsilon}{\mathrm{d}t} = \frac{\overline{v}(t)}{L_s} = \frac{v_2(t) - v_1(t)}{L_s} = \frac{c}{L_s}[\varepsilon^I(t) - \varepsilon^R(t) - \varepsilon^R(t)] \tag{2.9}$$

The strain can then be evaluated by just integrating over time the equation (2.9):

$$\varepsilon_s = \frac{c}{L_s}\int_0^t \left[\varepsilon^I(\tau) - \varepsilon^R(\tau) - \varepsilon^R(\tau)\right] \mathrm{d}\tau \tag{2.10}$$

The axial effort (N) at the incident bar/specimen interface can be obtained considering both the incident and reflected waves as given, respectively, by:

$$N_1^I(t) = EA\varepsilon^I(t) \quad \text{and} \quad N_1^R(t) = EA\varepsilon^R(t) \tag{2.11}$$

It follows that the resultant axial effort at the incident bar/specimen interface is given by:

$$N_1(t) = N_1^I(t) + N_1^R(t) = EA\left[\varepsilon^I(t) + \varepsilon^R(t)\right] \tag{2.12}$$

Assuming that this is the stress applied at the cross-section interface in between the incident bar / specimen, the normal stress (2-wave stress) can be evaluated as:

$$\sigma_s^{2w}(t) = \frac{EA}{A_s}\left[\varepsilon^I(t) + \varepsilon^R(t)\right] \tag{2.13}$$

where A_s represents the initial cross-section of the specimen. Following a similar analysis, the axial effort at the specimen / transmitted bar interface can be defined as:

$$N_2(t) = EA\varepsilon^T(t) \tag{2.14}$$

from which the following normal stress (1-wave) can be determined:

$$\sigma_s^{1w}(t) = \frac{EA}{A_s}\varepsilon^T(t) \tag{2.15}$$

To end with, from equations (2.14) and (2.15), another measure of the normal strain can be defined by considering an average of the normal stress (3-wave) given by:

$$\sigma_s^{3w}(t) = \frac{EA}{2A_s}\left[\varepsilon^I(t) + \varepsilon^R(t) + \varepsilon^T(t)\right] \tag{2.16}$$

It is noted that the average normal strain (ε_s, equation 2.10) and normal stress 3-wave ($\sigma_s^{3w}(t)$) can be used to represent the stress-strain mechanical response of the specimen only if the following quasi-static equilibrium condition is fulfilled (Chen and Song, 2011; Meyers, 2007; Ramesh, 2008):

$$N_1(t) = N_2(t) \tag{2.17}$$

Attending to equations (2.12) and (2.14), this equation can be equally written as:

$$\varepsilon^I(t) + \varepsilon^R(t) = \varepsilon^T(t) \tag{2.18}$$

If this condition is verified experimentally, then the strain of the specimen is uniform and can be simply measured as:

$$\varepsilon_s(t) = -\frac{2c}{L_s}\int_0^t \varepsilon^R(\tau)\mathrm{d}(\tau). \tag{2.19}$$

Moreover, the 1-wave (σ_s^{1w}), 2-wave (σ_s^{2w}) and 3-wave (σ_s^{3w}) normal stresses will be uniform in the specimen and simply given by:

$$\sigma_s(t) = \frac{EA}{A_s}\varepsilon^T(t). \tag{2.20}$$

Another issue to be taken into account on the SHPB analysis is the time shifting of the strain impulse recorded at the strain-gauges: $\varepsilon^I_{\text{SG1}}$, $\varepsilon^R_{\text{SG2}}$ and $\varepsilon^T_{\text{SG2}}$ to the instant t when the incident, the reflection and the transmission waves are actually acting simultaneously on the specimen at the bar interfaces. It can be shown that the following time shifting must be applied to the original signals:

$$t_s^I = t + \frac{\Delta L_{\text{SG1}}}{c}\ ; \quad t_s^R = t - \frac{\Delta L_{\text{SG1}}}{c}\ ; \quad t_s^T = t + \frac{\Delta L_{\text{SG2}}}{c} \tag{2.21}$$

where ΔL_{SG1} is the distance of the strain-gauge in the incident bar to the specimen interface, whilst ΔL_{SG2} is the distance of the second strain-gauge in the transmitted bar to the specimen interface.

Although the SHPB test is currently the classical test method to carry out high strain rate testing of materials, it presents several limitations and drawbacks (Field et al., 2004; Pierron et al., 2014). It is essentially a uniaxial loading test, based on homogenous states of stress and quasi-static equilibrium (inertial effects damp out after stress waves reverberation). Transient effects of the applied stress wave occurs at initial stages where the linear elastic behaviour is supposed to be valid. Therefore, the determination of the modulus of elasticity may not be accurate. When testing lower wave speed materials or materials with small ultimate strain (*e.g.* brittle materials) problems may exist because the quasi-static stress equilibrium cannot be fully reached before failure. This can limit of strain rate that can be obtained using standard SHPB.

2.3 Conclusion

In this chapter, the dynamic impact behaviour of materials was briefly analysed. The constitutive models and material parameter requirements for accurate numerical simulations have been pointed out. Moreover, the experimental techniques proposed for the characteristics of the dynamic impact behaviour of engineering materials have been reviewed. In particular, the classical Split-Hopkinson pressure bar (SHPB) technique is recalled, highlighting key assumptions and limitations.

3 | Wood structure and behaviour

3.1 Introduction

Wood has long been one of the most used materials by man, especially for building and other civil and military constructions (Ashby, 2005). Nowadays wood is mostly used in civil construction but is also used for the manufacture of storage boxes, pallets, flooring and furniture for the buildings (Fernando Sanz et al., 2006). There are several materials used in construction, such as light metals and plastics but wood is still used on a large scale. Currently the annual consumption of use of this biological material continues to increase slightly and the trend is that this increase will continue in the future, due to the increase in the price of plastics and the increase in housing construction (FAO, 2009). Wood is considered the only material used in construction that it presents as a material with environmental sustainability, recyclable, renewable and biodegradable (Dinwoodie, 2000). In the last decade, the concept of green building has gained more prominence in the area of civil construction, and this type of construction is being considered as an alternative building, as well as reducing the negative impacts of construction on human health. Wood has been the choice of most sought-after building material because of its low energy incorporation, low carbon impact and increased environmental sustainability (Falk et al., 2010).

In this way, it becomes fundamental to know the constitutive mechanical properties of wood as a biological material for its enhancement as an engineering structural material. In order to study the properties of wood, experimental tests are to be performed. Nevertheless, this is a challenge task to carry out because of wood anisotropy, variability and heterogeneity (Xavier, 2003). Wood consists of a complex and heterogeneous biological structure that is composed of cellulose, lignin, hemicelluloses and smaller amounts of other materials contained in its cellular structure (Lewin and Goldstein, 1991). This biological material presents a high resistance and stiffness to weight ratio which highlights its interest as a structural material. In addition, wood is a material that resists oxidation, acids, salt water and other corrosive agents, has a high recovery value and good collision resistance, which makes it an excellent structural material (Falk et al., 2010).

This chapter starts with a description of the two classes of wood species, known as softwood and hardwood species, heightening their similarities and differences. In the following, more emphasis is given to softwood species with a prominence in the *Pinus pinaster* Ait. specie. In this section, the anatomical structure of softwood, from the macroscopic down to the microscopic levels, the natural variability, as well as the material symmetry directions are reviewed. To end with, the topic of the dynamic behaviour of wood when subjected to high rates of deformation is developed and a literature review is carried out.

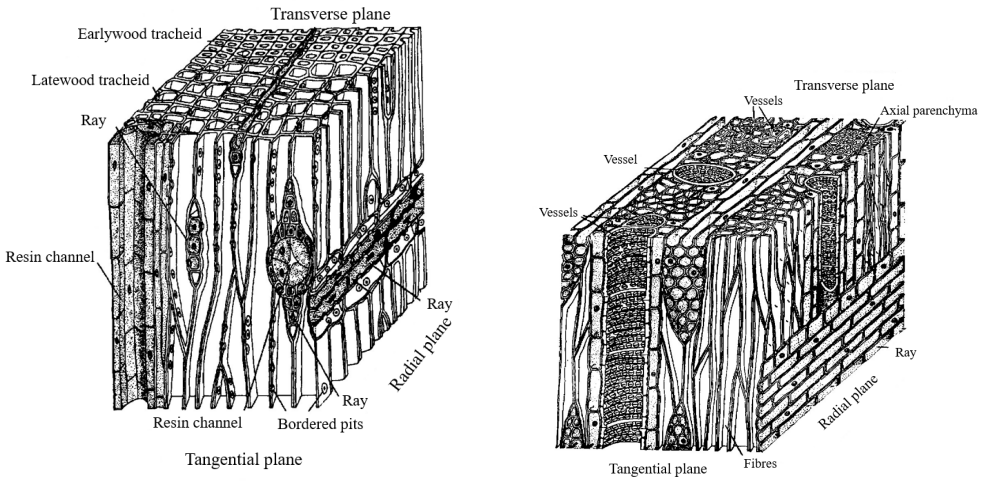

(a) (b)

Figure 3.1: Anatomic structure: a) softwood specie; b) hardwood specie [adapted from (Xavier, 2003)].

3.2 Softwood and hardwood species

The wood structure of trees has suffered evolution over millions of years in order to be an increasingly efficient system that will support the crown, drive the minerals through the trunk and store the food material. According to the internal structure, the wood species are classified as softwood (Gymnospermae) or hardwoods (Angiospermae) (Dinwoodie, 2000). Softwood and hardwood species are dissimilar in terms of their constituent cells. Softwood species contain a simpler structure than hardwood specie, since it only has two types of cells, the longitudinal tracheids and the ray parenchyma. Hardwood species present a bigger structural complexity, since it has a greater number of cell types and considerable variability among them. This difference in structure can be seen in figure 3.1.

Softwood species are basically made of two types of cells, so-called: tracheids and parenchyma (Dinwoodie, 2000). Tracheids are long cells, arranged in a vertical system aligned with the axis of the tree and had conduction and support functions, usually represent more than 95% of the total trunk volume. On the other hand, parencgyma are cells with storage and transport functions, which are organized in a horizontal system, from the centre to the edge of the trunk.

Hardwood species demonstrate four types of cells: tracheids, parenchyma, fibres and vessels (Dinwoodie, 2000). Tracheid cells are present in small amounts and have support and conduction functions. The storage job is made by parenchyma that shows a horizontal direction in the ray zone or vertical direction in the other zones. Fibres are cells that allow the support of the tree, which are thin and long with tapered ends. Conduction is performed by vessels cells, mostly small and wide when compared to other cells. Therefore, while in softwood species the three functions are executed by two types of cells, in hardwood species each function is perfomed by a single cell type.

Hardwood species can be further classified considering porosity as the criterium. Porosity on hardwood species can be classified as ring porosity or diffuse porosity as shown in figure 3.2 (Dinwoodie, 2000). Hardwood species of ring porosity demonstrate vessels in the initial wood

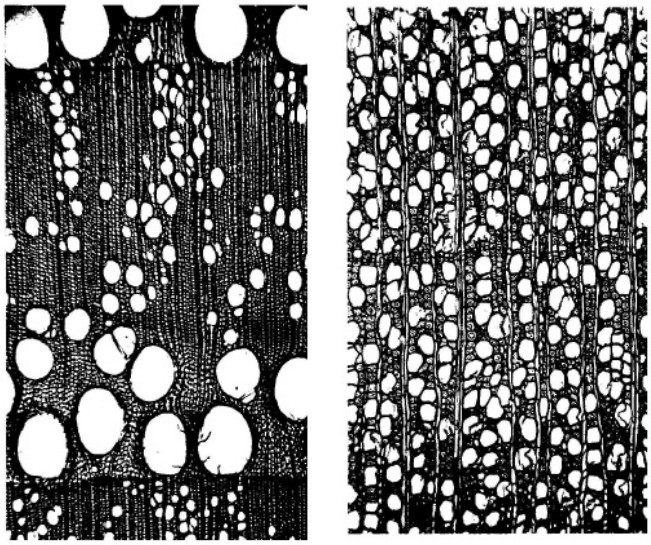

(a) (b)

Figure 3.2: Hardwood species classification: (a) ring porosity; (b) diffuse porosity (Xavier, 2003).

larger than the vessels form in the final wood. While hardwood species of diffuse porosity have vessels if initial wood and final wood of identical magnitude. However, there are some exceptions of hardwood species which present vessels in the initial wood are larger but decrease as it approaches the final wood, in this manner this are called semi-diffuse porosity species (Xavier, 2003).

3.3 Wood of softwood species

The wood specie chosen for study in this report is *Pinus pinaster* Ait., which is a softwood specie. In this way a greater focus will be made to the study of the properties of this species of wood. *Pinus pinaster* Ait. is a conifer specie that can be found in western Mediterranean area and in Atlantic zone of southwest Europe that constitutes forests in France, Spain, Portugal, Italy, Morocco, Algeria and Tunisia (García-Iruela et al., 2016). In Portugal, *Pinus pinaster* Ait. occupies an area of 29% the total forest area. This specie is also known as maritime pine. This specie stands out for its high resistance to sandy and poorly fertile soils as well as for its rapid growth (Sanz, Fernando Latour et al., 2006).

3.3.1 Macroscopic structure

At the cross-section of the tree stem, it is possible to observe annual rings corresponding to the seasonal growth of the tree. These growth rings are typically concentric and of periodic bright and dark regions corresponding to the formation of earlywood and latewood. Earlywood cells are formed at the spring time and have thin walls and large lumens. Latewood, on the other hand, is formed at the autumn period with larger walls and thin lumens (Dinwoodie, 2000).

The three functions that the stem of a tree executes are: support, conduction and storage. The stem must support the crown, region responsible for production of food and seeds, it also has to lead minerals absorbed by roots upwards to crown, as well as to store the manufactured

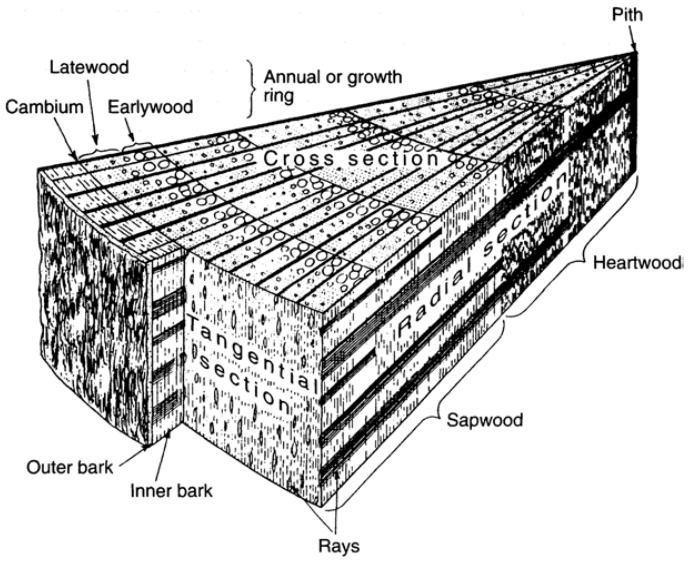

Figure 3.3: Macroscopic structure of the trunk of a softwood specie (Dinwoodie, 2000).

foods (Dinwoodie, 2000). The stem is composed of several materials in concentric bands which is divided into two distinct zones: sapwood and heartwood. These constituent elements of the stem are shown in figure 3.3. Sapwood consist in live and active wood that conducts water or sap from roots to leaves through the parenchyma cells, but also stores and performs synthesis of biochemicals. This zone has a lighter colour compared to heartwood that has a darker colour. Heartwood has long term storage function of many varieties of biochemicals.

Outer bark provides mechanical protection to inner bark, this is smoother and helps limit loss of evaporated water. Inner bark is the tissue whose foods are produced by photosynthesis and transported from leaves to roots. Cambium is the layer next to the inner bark which is responsible for formation of new wood cells, producing two tissues for years. Pith or medulla in the centre of stem is the result of the initial growth of the tree before the wood is formed.

3.3.2 Microscopic structure

At the microscopic level, softwood species demonstrate a relatively simple structure. The axial or vertical system consists of tracheids cells while the radial or horizontal system is composed of rays cells, which are mainly composed of parenchyma cells. In the Figure 3.4 it is possible to observe cells components from microscopic structure of softwood species. Tracheids cells are much longer than wide being these the main component of softwood species, making more than 90% of the volume of wood. These satisfy the conductive and the mechanical needs of softwood species. The thickness of walls of these cells differ throughout the year, increasing firmly from spring to autumn. Tracheids have circular holes to allow the passage of water through these cells. Parenchyma ray cells own a rectangular structure and form the rays which function primarily in synthesis, storage and transport of biochemicals (Dinwoodie, 2000).

A plant cell has two domains: the protoplast and the cell wall. The protoplast consists of the sum of living components that are limited by the cell membrane. The cell wall is a non-living element which consist of a carbohydrate matrix extruded by protoplast to outside of the cell membrane. The cell wall also provides mechanical support to the plant in general. The lumen

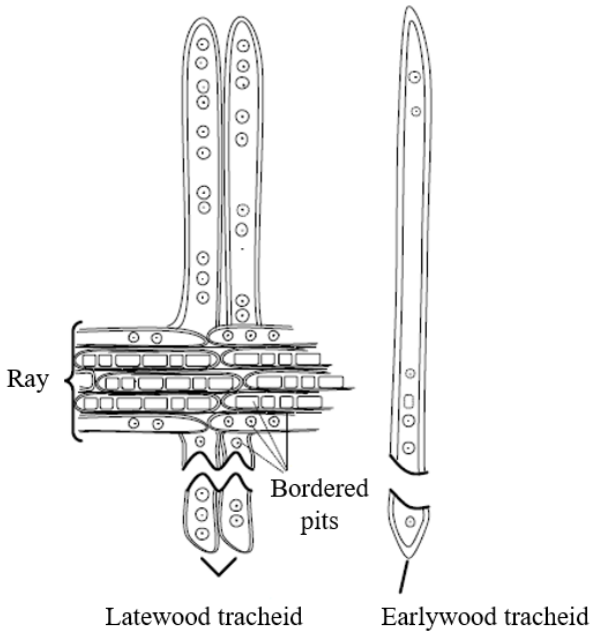

Figure 3.4: Microscopic aspects of the wood of softwood species (Garrido, 2004).

does not have a physical structure since it consists of the empty space inside the cell. In this way, wood has two domains: empty space and cell walls of the components of cells.

The cell wall consists of three main zones: the middle lamella, the primary wall and the secondary wall, as shown in Figure 3.5. In each region, the cell wall consists from three main components: lignin, hemicelluloses and cellulose microfibrils. The first zone is the middle lamella also called the intercellular layer, since it is disposed between two adjacent cells and consists about 80% of its volume in lignin and hemicelluloses and the cellulose is practically absent from its constitution. The second region is the primary wall which has a large amount of lignin, a considerable amount of hemicelluloses and about 20 to 25% of its cellulose volume. The secondary wall is divided into three layers, called S1, S2 and S3. The S1 is considered the thinnest however the layer S2 is the thickest and the layer S3 has the smallest percentage of lignin in the three layers (Dinwoodie, 2000). The distribution of the cell types and their sizes are used to identify the wood as well as its various properties.

3.3.3 Variability in structure

Wood is a biological material with a huge variability, both among and within species. This variability is reflected on wood proprieties, either physical or mechanical. Therefore the identification of mechanical properties of wood is typically associated with a large scatter (Dinwoodie, 2000).

Several types of wood variability can be distinguished: (i) the variability that occurs between species, which exists due to the genetic differences between the diverse species, (ii) the variability that occurs between trees of the same species due to genetic factors, (iii) the variability that which occurs within the tree due to external factors, such as climate, soil and nutrient availability (Pereira et al., 2014; Pereira, 2013).

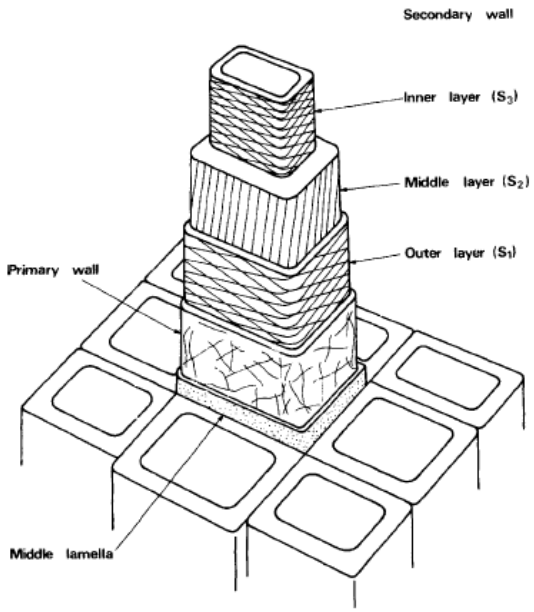

Figure 3.5: Representation of the cell wall structure (Dinwoodie, 2000).

In the stem of the tree there are distinct patterns of variation that contribute to structural differences. Showing large variations from the centre to the bark, and the basis for the canopy, are aspects such as the length of the cells, cell wall thickness and density, the angle formed between the cells to the longitudinal axis of the tree and the location of the microfibrils of the S2 layer of the cell wall relative to the vertical axis (Dinwoodie, 2000). However, there are also differences between juvenile and mature wood in relation to the variability of their structure. Juvenile wood has larger tracheids and thicker cell walls than mature wood, which converts to a higher average density (Pereira, 2013).

3.3.4 Directions of wood material symmetry

At the macroscopic level, clear wood can be modelled as an anisotropic material. It means that its mechanical behaviour at a given point in the solid, depends on the direction of solicitation. Observing the material structure at the cellular tissue level, three main axes of material symmetry are revealed. These axis defines an orthonormal coordinate system that is typically used in wood and fracture mechanics analysis (Smith et al., 2003). In practice, wood is usually modelled as an orthotropic material with three orthogonal directions (Figure 3.6): the longitudinal direction (L), according to the direction of fibers; the radial direction (R), axis perpendicular to the rings of annual growth; and the tangential axis (T), parallel to the rings of annual growth and perpendicular to the other two directions of symmetry (Dinwoodie, 2000; Kollman and Côté Jr., 1984). These material axes will define three main planes: the transverse plane (RT), the radial plane (LR) and tangential plane (LT). These orthogonal planes are determined through the structure of the wood and the way in which the cells of microscopic structure are arranged (Falk et al., 2010).

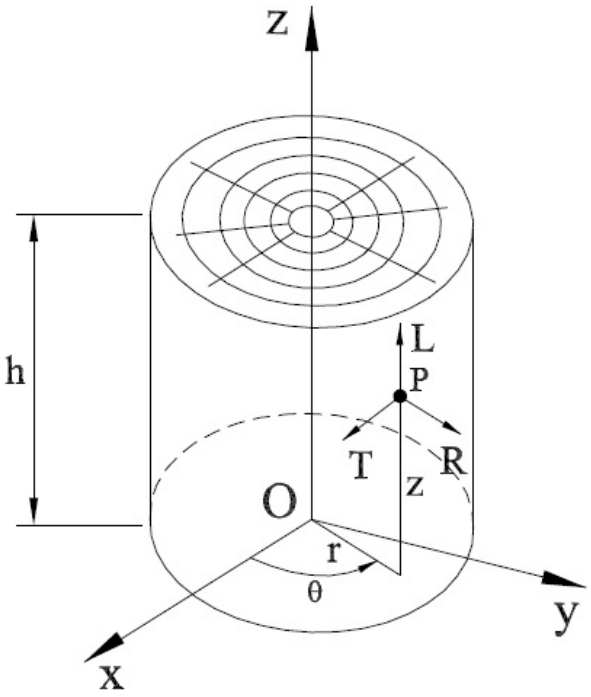

Figure 3.6: Orthonormal material symmetry direction of wood within the stem (Xavier, 2003).

3.4 Wood characterization at high strain rates

3.4.1 Intermediate strain rate testing

The range of intermediate strain rates is between 0,01 and 1 s^{-1} and incorporates most possible applications in engineering. For the study of materials subject to intermediate deformation rates, hydraulic servo machines are normally used.

Nakamura et al. in 1980 conducted tests on a shaking table of a one-stage steel structure subject to accelerations, which allowed to conclude that the deformation rates of a seismic event are between 0.01 and 1 sec, range of intermediate strain rates. Therefore, it is relevant to understand the dynamic behaviour of the wood when subjected to intermediate deformation rates, since this biological material is often used for civil construction.

Liska in the year 1950 introduced the concept of duration of load (DOL) and concluded with his scientific research that the tensile strength increases with the decrease of time until the failure of the sample. Subsequently, Liska found that the wood showed a tensile strength 1.26 to 1.28 higher in the static tests than in the dynamic tests for the loading rate that was being used.

Madsen (1975) showed the importance of carrying out tests with samples of structural size, in order to obtain results closer to the properties of the material in its authentic size. After the Madsen reports, the wood science community has implemented more research on structural size samples for this biological material in order to obtain more values for future projects (Polocoser et al., 2017).

3.4.2 Transverse impact

In impact events, almost all follow the same scenario, that is, following the impact a wave is propagated from the point of impact. This wave can be of two types: longitudinal or compression wave, and transverse or cut wave.

The transverse impact is studied almost exclusively for beam like structures, which can be simply supported, elastically supported or centrally impacted. The longitudinal impact is a type of set of experimental tests for high rates of deformation of materials subjected to compression or traction.

The cross impact tests consist of a falling mass, but an experimental test to study the wood in transverse impact has not yet been standardized. This type of test is usually used to determine the strength of a sample of wood.

Rayleigh in the year 1906 has shown that if the duration of the force is long in comparison with the natural frequency of the structure, then the vibrations induced in the oscillatory system will be few. This is one of the reasons why the machines of the cross impact test have enormous dimensions.

Elmendorf in 1916 used the Hatt-Turner drop tower to perform dynamic cross-tests on samples of wood beams, and this machine is one of the numerous machines used in cross-impact tests.

Wilson (1922) continued the work done by Elmendorf in 1916 and compared the results of three tests performed on cross-impact machines, Hatt-Turner drop tower, single-blow and pendulum using wood samples. These three impact tests consist of breaking the sample with a single blow. In addition to these three devices described, very few cross-impact tests exist or are described. In this study, the investigator concluded that the value of rupture stress in dynamic tests is about double the value in static tests.

In 1933 Koehler studied the comparison between the result of the impact on the wood in the tangential direction and in the radial direction. A detailed review of wood resistance of different species was carried out. A conclusion reached in this study regarding the morphology was that a variation in the orientation angle of the fibres in relation to the line of action of the applied force affects the resistance of the wood. In addition, the presence of defects in the wood, such as knots, affect its strength.

Later, Pettifor (1942) compared both directions and concluded that the wood when it suffers the impact in the tangential direction is harder than in the radial direction. This conclusion was later verified by Keith in 1964 who studied Douglas fir (Pseudotsuga menziesii), verifying that it is stronger when impacted in the tangential direction, however, the position of the earlywood or latewood ring in relation to the traction or had no significant difference. In this study Keith considered that this result was derived from the curvature of the growth rings and the existing density gradient from the marrow to the shell.

Drow et al. (1958) found that the ring orientation presented a substantial influence for softwoods tested in tangential and radial impacts but showed insignificant differences for hardwoods.

Kloot in the year 1954 studied the influence of the water content on the wood in the values of the resistance when it undergoes an impact. In this investigation it was concluded that the resistance of the wood of the species tested was minimal when it had a water content of 12% to 16%.

James in 1962 concluded that green wood is stronger than dry wood when it is subject to

impact. This conclusion shows the influence of the moisture content on the wood project subject to impact (Polocoser et al., 2017).

3.4.3 Longitudinal impact: high strain rate

In the years 1879 and 1892, Pochhammer and Chree, respectively, worked separately with the objective of finding a specific solution for the longitudinal impact on the wood at high rates of deformation. Both presented the same solution, the Kolsky bar as an important experimental trial to study the wood when subjected to impact.

In 1970, there was an increase in the number of experimental tests using the Split-Hopkinson pressure bar in dynamic tests. This experimental technique requires samples of small size, however in the case of wood, this sample size does not represent the values for the wood in its structural size. In this way, samples of wood of small size, but also of larger sizes, should not only be studied.

In the year 1986, William Johnson carried out a review of the various dynamic and historical uses of wood, including wood machines used in warfare. In this study, a relation between the velocity of the projectile and the depth of penetration of the same in the wood was presented.

Stephen R. Reid and Changsheng Peng in 1997 studied the static and dynamic behaviour of wood when subjected to crushing. The researchers were the first investigators to test the wood using the Kolsky test with a compressed air gun at high speeds to obtain higher deformation rates. In this study the properties of the wood were analyzed when it was requested perpendicularly and parallel to the grain. It has been assumed that the properties of the wood do not depend on the rates of deformation to which it is subjected in the experimental test and that the differences between the static and dynamic tests are due to the inertial effects.

Bragov and Lomunov in 1997 carried out a study confirming the study by Peng (1991), in which an experimental test was carried out with several species of wood, in which they were subjected to rates of deformation in the order of 1×10^3 and 1×10^4 s^{-1}. It was found that the properties of the biological material do not depend on the rate of deformation in the directions parallel and perpendicular to the fibres.

In 2004, the researcher Svante Widehammar carried out a study on the spruce wood (Picea sp.) On the radial, tangential and axial faces. For this, he used the servo-hydraulic machine for the test at intermediate strain rates and the Kolsky bar for the test at high strain rates. The research took into account three moisture contents, dry kiln, saturated fibre and fully saturated (green). The investigator inferred that wood exhibits a marked viscoelastic behaviour through tests at high rates of deformation and that the Young modulus is minimally affected by the deformation rates at which the material is subjected.

Mohammad R. Allazadeh and Sylvanus N. Wosu conducted tests in the Split-Hopkinson pressure bar in 2012 to study the influence of the depth of the wood sample on the behaviour of the deformation rate. With the increase of the depth of the sample to double, the deformation rate of the material increased four times. In this study it was concluded that with the increase of the depth of the sample to double, the deformation rate of the material increased four times.

In 2013, Christopher G. Gilberstson and William M. Bulleit studied the proportions of the sample in order to reduce the inertia and friction effects of the of the Split-Hopkinson pressure bar test. However, there is as yet no consensus on the constitutive model for wood when subjected to high rates of deformation (Polocoser et al., 2017).

3.5 Conclusion

This chapter starts with a description of the wood structure, following a hierarchical path from macroscopic down to microscopic levels. Softwood and hardwood species were compared in relation to their anatomical structure. However, emphasis was given to softwood species, since *Pinus pinaster* Ait. wood was selected for this study. Subsequently, the anisotropy and heteregeneity of wood was discussed since their importance in the mechanical behaviour of wood. Finally, the characterisation of wood when subjected to high strain rate testing was discussed. A literature review was presented highlighting main conclusions on the subject.

4 | Methodologies

4.1 Introduction

This chapter begins with a description of the image-based inertial impact test (IBII) developed in the PhotoDyn project[1]. The IBII test was designed to address the dynamic behaviour of materials when submitted to high strain rate loading. The tests was proposed as an alternative to the classical split-Hopkinson pressure bar (SHPB) test, overcoming some issues associated to the restrictive requirements of quasi-static stress equilibrium (neglecting inertial acceleration effects) and 1D wave propagation theory (no dispersion effects) (Fletcher and Pierron, 2018). All physical components of the set-up are described and their mode of operation is detailed.

The IBII test rely on an optical method to retrieve displacement, strain and acceleration kinematic fields directly from images recorded by an ultra-high speed camera. The grid method is used for that purpose. To start with, its principle is reviewed. This white-light optical technique relies on the geometric deformation of a regular pattern that is fixed to the external surface of interest of the sample (Grediac et al., 2018). The grid transfer and grid light modelling are presented. Moreover, the technology of ultra high speed cameras is highlighted, since this is a requirement of the IBII test, *i.e.* having both suitable spatial and temporal resolutions (Fletcher et al., 2019). The different high and ultra high speed cameras currently available on the market, as well as the various techniques used in cameras are provided. Some considerations to deal with when setting up an image acquisition device are described. The digital image sensors used in the ultra high speed cameras are also referred.

To end with, the virtual field method (VFM) is evidenced as a material identification technique. The VFM was firstly developed to the characterisation of linear elastic orthotropic behaviour (Grédiac et al., 2006). More recently, however, applications were developed in the area of dynamics through studies on harmonic loads, relative to vibrations. The first application of this methodology in an experimental impact test was published in 2011 (Pierron and Grédiac, 2012). More recently, this inverse technique was used to identify the constituent properties of materials at high strain rates through the kinematic fields generated by an inertial impact test (Blitterswyk et al., 2018; Fletcher and Pierron, 2018; Fletcher et al., 2019). Firstly, the constitutive law for isotropic and orthotropic materials is presented, and an elastic linear behaviour is assumed. The concept of using the acceleration field to identify the constituent parameters of the material is also described. Two case studies are addressed considering isotropic and orthotropic material models. From the Principal of Virtual Work, test functions so–called virtual fields are manually selected to yield a linear system of equilibrium equations for the unknown material parameters.

[1] PhotoDyn – *Innovative photomechanical approaches in identification of the dynamic mechanical behaviour of materials* http://photodyn.org/

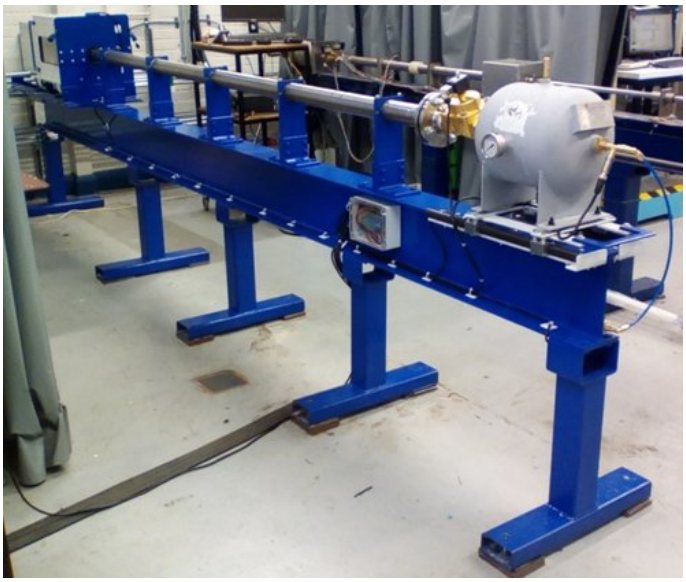

Figure 4.1: Inertial impact test (from PhotoDyn project).

4.2 Image-based inertial impact test

The IBII test was recently proposed as part of the PhotoDyn project, which refers to innovative photomechanical approaches on the identification of dynamic behaviour of materials. The project aimed at designing a new dynamic test method, based on digital imaging technology, to allow the measurements of kinematic fields, in the form of both strain and acceleration, at high strain rates. Using this information together with an efficient inverse identification technique such as the VFM, it is possible to develop a new experimental methodology to identify the constitutive parameters in the high strain rate regimes. This test is intended to be a new generation of dynamic tests in alternative for instance to the classical SHPB test. Therefore it represents a disruptive innovation in relation to current experimental tools for characterizing the dynamic behaviour of materials.

The IBII set-up is a gas gun facility consists of pressure reservoir, a barrel and an impact chamber, as shown in figure 4.1 (Blitterswyk et al., 2018; Fletcher and Pierron, 2018; Fletcher et al., 2019). The waveguide and specimen are located in the impact chamber in which a high speed camera is mounted to observe the external surface of the specimen. This surface must have a period pattern suitable to apply the grid method, with accurate spatial resolution.

This test has been successfully applied to the study of quasi-fragile or fragile materials. The figure 4.2 shows the physical components required for the experimental technique, which are a sample, a waveguide, a projectile and a base from which the projectile is launched.

The test begins with the impact of the projectile on the sample, which is charged with a compression pulse, $F(t)$, as shown in figure 4.3 (Fletcher and Pierron, 2018). The projectile is launched by means of a compressed air gas gun which is capable of launching the projectile at impact speeds in the order of 100 m/s.

The compressive tension wave coming from the impact pulse travels through the sample and reflects, becoming elastic. When the wave reflects on the free surface of the sample, it fails. During the propagation of the voltage wave, displacement field measurements are obtained through the use of the image and its processing. Displacement measurements during the dynamic

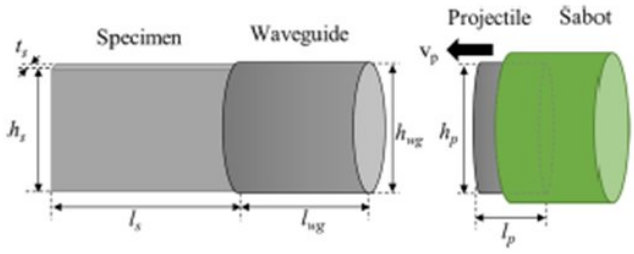

Figure 4.2: Representative scheme of the physical components of inertial impact test (Fletcher and Pierron, 2018).

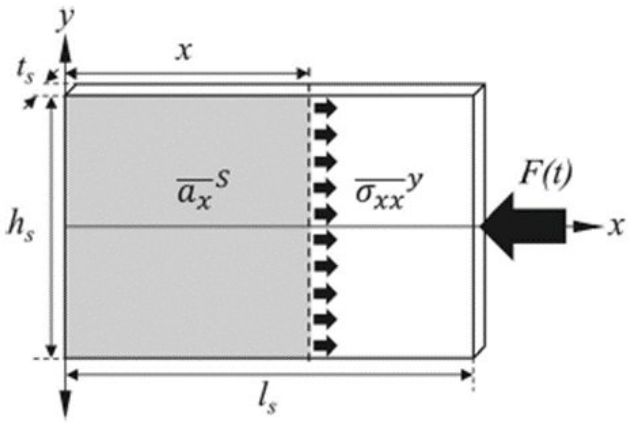

Figure 4.3: Representative scheme of inertial impact test sample when loaded with a compression pulse (Fletcher and Pierron, 2018).

test are performed by the grid technique using an ultra-fast chamber. Based on the displacement field measurements, the acceleration field is obtained by a temporal derivation and the strain field is obtained by spatial derivation. Estimated kinematic fields will be used to determine the constitutive properties of the material through the use of VFM (Fletcher and Pierron, 2018).

The test allows to explore the inertial effects generated on high strain rate loading (Blitterswyk et al., 2018). For displacement field we used the grid method, because this experimental technique provides better spatial resolutions when compared with alternative techniques such as digital image correlation (DIC). The figure 4.4 shows all components required for the operation of the inertial impact test (Fletcher and Pierron, 2018).

4.3 Grid Method

Optical techniques of total field measurement are common in experimental mechanics. With the constant improvement of these techniques and the coupled procedures, it has been simpler to improve the characterization of materials and structures. Because of their ease of use, white light techniques have become more popular in experimental mechanics. Two white light techniques that are now generally accepted are digital image correlation (DIC) and grid method (Grédiac et al., 2016).

The grid method translates into a non-interferometric optical technique used to measure displacement and strain fields in experimental mechanics. This consists of an application of

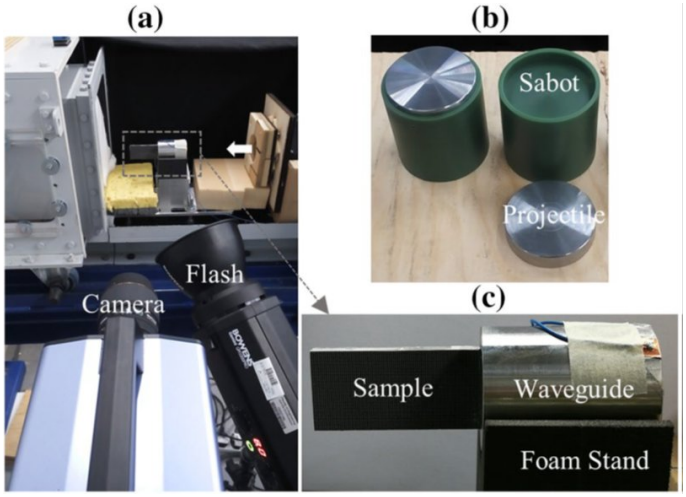

Figure 4.4: (a) Photograph of experimental ultra high speed camera, light flash and sample. (b) Projectile and its base. (c) Test specimen of the wave and foam support (Fletcher and Pierron, 2018).

Figure 4.5: Illustrative image of: (a) cross grid, $I(x,y)$; (b) grid with vertical lines, $I_x(x,y)$ (proporcional a $u_x(x_1,x_2)$); (c) grid with horizontal lines, $I_y(x,y)$ (proportional to $u_y(x_1,x_2)$) (Xavier, 2007).

a regular pattern on the surface of the sample (Grediac et al., 2018). The grid method uses a periodic pattern, while the digital image correlation uses a random pattern. In this way, the method presents a better relation between spatial and deformation resolutions than digital image correlation (Fletcher and Pierron, 2018). The periodic pattern of the method consists in a grid, which is a set of periodically spaced lines (Avril et al., 2004b). Grid lines should be as short as possible (Avril et al., 2004a). Figure 4.5 shows an example of a cross grid, whose vertical and horizontal lines are proportional to the components of the horizontal and vertical displacement, respectively. The grid is defined by a periodic pattern of dark and contrasted lines, characterized by a spatial frequency vector $\mathbf{F} = \mathbf{n}/p(lines/mm)$, where $\mathbf{n}$ represents the orthogonal vector to the grid lines and defines the pitch grid. Thus, a cross grid (overlapping of vertical and horizontal lines) can be used to simultaneously obtain the two components of the displacement.

In figure 4.5 it is possible to observe unidirectional grids and a bidirectional grid, this technique uses bidirectional grids allowing to detect oblique fractures, being applied in directions i and j, with only a single image of the grid. The use of a single image allows monitoring fractures in damaged structures over a period, thus becoming the main advantage of the method under study (Avril et al., 2004a).

The regular pattern, as shown in figure 4.6, is obtained by printing the grid on a transparent sheet and then transferred to the sample surface, which was previously painted white (Avril et al., 2004a). In this procedure of constitution of the grid can appear defects in the same, as

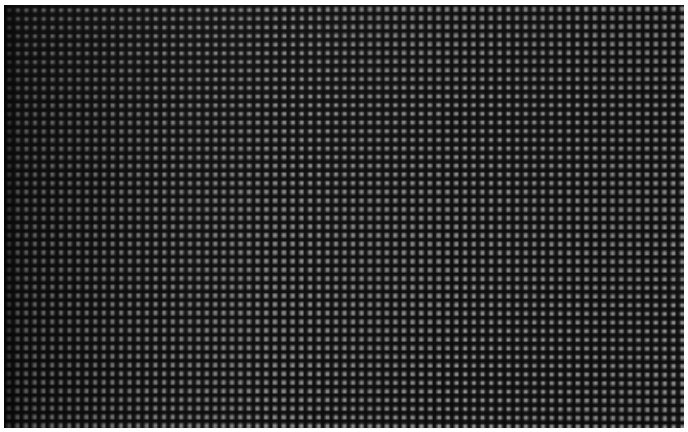

Figure 4.6: Example of a grid (from PhotoDyn project).

a result of bubbles in the glue used to join the grid to the sample. Within the confines of the sample surface defects may appear in view of the transfer process of the grid. This application of a regular pattern in the sample consists of the main disadvantage of the grid method. However, a new method was developed to add the grid to the sample. This new procedure allows the grid to be printed directly onto the sample through an inject printer, thus reducing the occurrence of grid defects (Fletcher and Pierron, 2018). In order to measure the total displacement field with the grid method, two images are required, since the displacement vector is calculated by the difference of two patterns, the initial and final configuration (Avril et al., 2004a).

Grid Images assume that the horizontal and vertical lines of the grid are aligned with the lines and columns of the camera's sensor pixels in the grid images. The intensity of the light $s(x,y)$ at each point (x,y) is considered a quasi-periodic signal, which can be modelled by the following expression:

$$s(x,y) = \frac{A}{2}\left(\left(2+\gamma.frng\left(2\pi fx+\phi_x\left(x,y\right)\right)+\gamma.frng\left(2\pi fy+\phi_y(x,y)\right)\right)\right) \tag{4.1}$$

In this expression, A corresponds to the mean global field illumination, γ is equivalent to the contrast of the oscillatory pattern, which comprises values between 0 and 1, $frng$ consists of a real periodic function with amplitude 2π for 1 and average value for 0, f is the frequency, is defined as the inverse of the step pattern, p, $\phi_x\left(x,y\right)$ and $\phi_y\left(x,y\right)$ represent the carrier phase modulations defined as the modulo 2π along the x and y axes, respectively (Grédiac et al., 2016). The $frng$ function in the equation 4.1 admits a Fourier series development. The phase detection algorithm (associated with the spatial position of the grid at a given instant) should eliminate higher order harmonics typically present in $frng$. It should be noted that the grate image can be acquired experimentally with a slight blurring so that the grid lines, of rectangular profile, may appear slightly fuzzy, justifying the simplified hypothesis of a sinusoidal profile. The calculation of the phase field at each instant, from the image of light intensities reflected on the grid, determines the spatial position of the grid (Blitterswyk et al., 2018).

Considering $u = (u_x, u_y)$ the direct displacement field and $U = (U_x, U_y)$ reverse displacement field thus a point with coordinates $x(x,y)$ after a deformation corresponding to a point of coordinates $x + u(x)$, as can be seen in figure 4.7. Since both fields are connected through the

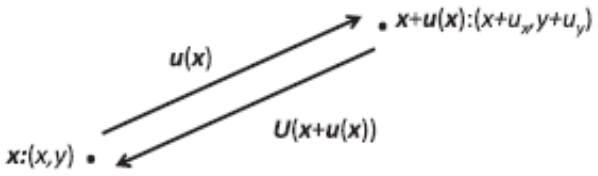

Figure 4.7: Displacement of a physical point (Grédiac et al., 2016).

following equations:

$$\begin{cases} u(x) = -U(x+u(x)) \\ U(x) = -u(x+U(x)) \end{cases} \tag{4.2}$$

The displacement field can be determined from the phase difference between the two initial and final states by the following relation:

$$\Delta\phi(x) = -2\pi f u(x) \tag{4.3}$$

Where p is the pitch of the grid, $\Delta\phi(x)$ represents the phase variation. The direct displacement field u cannot be estimated directly from the phase variation $\Delta\phi(x)$, since this entity depends on u. In this context, two approaches are possible:

1. Procedure: the approximate approach

   In this approach the direct displacement field u is calculated from the following mathematical equations:

   $$u(x) = -\frac{p}{2\pi}\left(\phi^2(x) - \phi^1(x)\right) \tag{4.4}$$

   instead of

   $$u(x) = -\frac{p}{2\pi}\left(\phi^2(x+u(x)) - \phi^1(x)\right) \tag{4.5}$$

   The displacement of physical points is neglected, which is permissible for small displacements, which is what happens in real cases.

2. Procedure: the rigorous approach

   Considering that the direct displacement field u is the solution of a fixed point and that the initial estimate u_0 is possible, then the direct displacement field u can be iteratively refined by an algorithm, as described in the following expression:

   $$u^{n+1}(x) = -\frac{p}{2\pi}\left(\phi^2(x+u^n(x)) - \phi^1(x)\right) \tag{4.6}$$

The phases are extracted from the grid images, however the gross phase distributions are known to have a 2π module. Thus, discontinuities occur in the raw phase images as soon as the displacement has a spatial fluctuation greater than the grid pitch, this discontinuous distribution is called wrapped. To make these phase distributions spatially continuous an unwrapping algorithm must be applied (Grédiac et al., 2016).

Considering that the first harmonic of the $frng$ function of the equation 4.1 has three unknowns, therefore a minimum sample of three pixels per period is necessary. However, it is considered that having five pixels per period shows a good compromise for practical experience. This number when increased to values greater than five shows a deterioration in the phase estimation due to the reduction of spatial resolution (Rossi and Pierron, 2012). Thus, the number of grid periods can be determined by the expression:

$$\text{Grid periods} = \frac{\text{Camera resolution}}{\text{Pixeis by period}} \tag{4.7}$$

In this way, it is possible to define the pitch of the grid as follows (Longana, 2014):

$$\text{Grid Pitch} = \frac{\text{Sample size}}{\text{Grid periods}} \tag{4.8}$$

Each pixel has a certain amount of grey on a scale ranging from 0 to 255, with 0 representing black and 255 representing white.

The results of the measured displacement field are influenced by the measurement system, the lighting conditions and the grid pattern. The measuring system consists of the lenses, the Charge Coupled Device (CCD) camera and the image correlation software (Lecompte et al., 2006). In the digital camera, each image is associated with an array of CCD sensors, and each pixel of the image obtained corresponds to a CCD camera sensor (Rossi and Pierron, 2012). In the inertial impact test an ultra-fast velocity chamber is used to collect the deformed images, and the grid method is applied later (Blitterswyk et al., 2018). Optical techniques have been increasingly used in experimental mechanics because of the reduced cost of ultra-fast cameras and improved performance, which provide better measurements of displacement or strain fields (Grédiac et al., 2016).

4.3.1 Ultra high speed imaging

Ultra high speed cameras are used to capture images of phenomena not visible to the human eye. This visualization of phenomena of high speed in images with high temporal resolution allows to the user to obtain information quite detailed. In this way, ultra-high-speed cameras are a tool used in many applications. Due to the increasing technological development in the last years, the researchers need to register phenomena faster and more detailed (Kondo et al., 2013). These cameras began with film versions and now present digital versions, with this change it was possible to use the computational analysis of the images in order to obtain quantitative information of the event (Reu, 2011).

Over the last two decades, due to the advancement of digital image sensor technology coupled with the availability of image processing algorithms, it has been possible to obtain more quantitative information from experiments, such as the deformation of a large number of points on the surface of a sample (Zhu, 2015). In the inertial impact test, the capture of images for the measurement of the displacement field is carried out by cameras of ultra high temporal velocity (Fletcher et al., 2019).

The graphic of figure 4.8 identifies the ultra high speed cameras currently available on the market (Reu and Miller, 2008). In this graph the cameras are classified by the number of frames per second (frame rate, fps) on the horizontal axis and by the total number of recorded images, on the vertical axis. Each rectangle is proportional to the size of the digital camera sensor and the

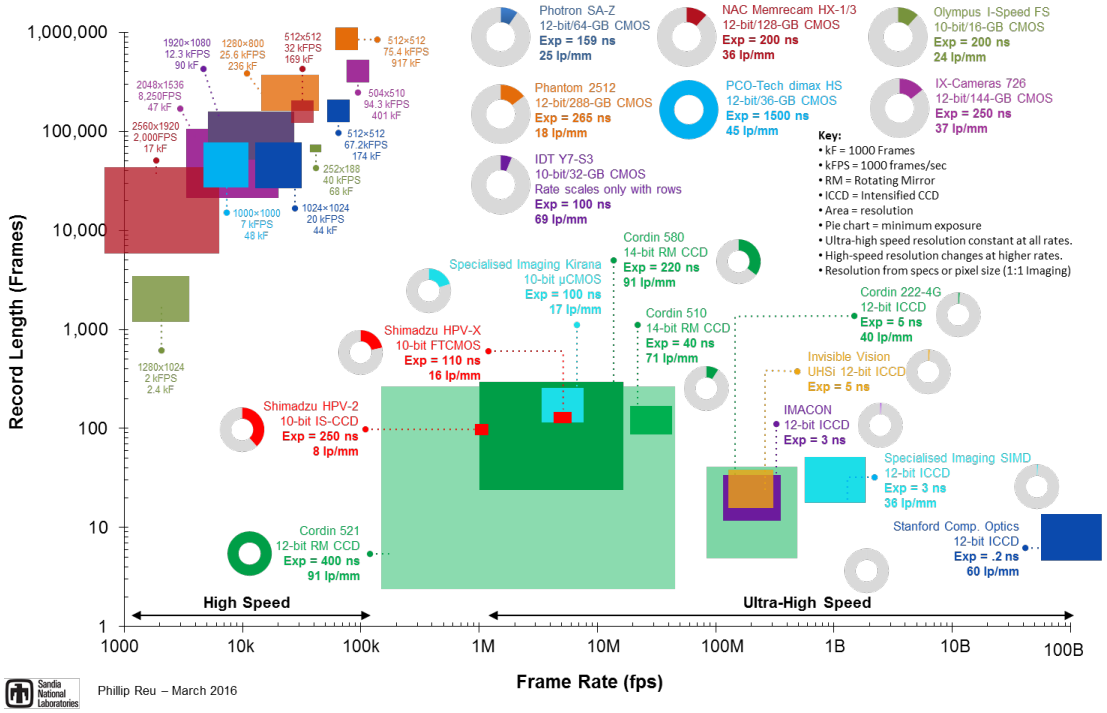

Figure 4.8: High speed and ultra high speed cameras available on the market [adapted from (Reu and Miller, 2008)].

coloured circular sectors represent the total acquisition times. High speed cameras occupy the top left-hand side of the graph considering the high number of image recordings but limited by the number of frames per second. In the lower part of the graph are the ultra high speed cameras, presenting these smaller number of images per test or recording, but with a high number of frames per second (Fletcher and Pierron, 2018).

In order to perform this type of experimental tests in which the materials are subjected to high deformation rates, with the use of optical techniques it is necessary to obtain images at high frame rates (Longana, 2014). The main limitation of ultrafast cameras is the frame rate at which the pixels can be read by the detector. This being the reason why in order to increase the frame rate of the cameras the resolution has to decrease (Reu, 2011). Currently, there are many commercial cameras that are available to capture dynamic images at different frame rates. So to achieve high frame rates, the critical issue is the speed of data reading (number of pixels x frame rate). Nowadays, this issue is being solved with the use of different techniques, such as rotating mirrors, beam dividers and some image sensors (Zhu, 2015).

Ultra high speed cameras can be composed of three different techniques: rotating mirror, optical paths divided by a beam and memory in spline. The rotating mirror method and optical paths divided by a beam use an optical system to replicate or move the image to obtain multiple images on different detectors at high frame rates. Rotating mirrored cameras presents a problem in recording and image distortion. The sliver memory method uses a built-in memory in the image detector, which eliminates the problems of image distortion introduced. The quality of the images captured by the ultrasound cameras is a problem intrinsic to all cameras because of their configuration and the limits of physics (Reu, 2011).

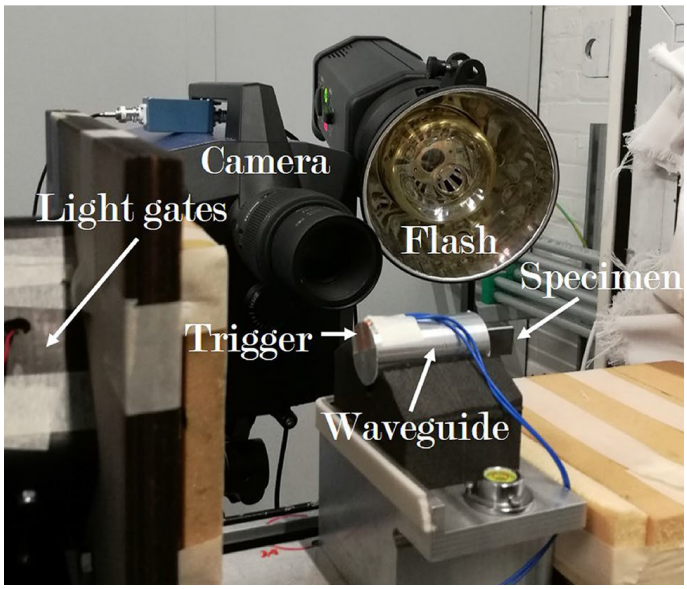

Figure 4.9: Ultra high speed camera and flash experimental setup (Fletcher and Pierron, 2018).

Ultra high speed camera system consists of a camera, a power supply unit, and a computer (Kondo et al., 2013). The experimental setup of the camera, flash and sample is shown in figure 4.9.

To set up an imaging device for optical total field measurement techniques, the following considerations must be considered:

- Focusing: the entire surface of the sample should be properly focused and photographed;
- Grey scale distribution: it is fundamental to ensure that the image has a grey scale distribution suitable for the subsequent application of image correlation techniques. This appropriate grayscale distribution is achieved by regulating the amount of light;
- Depth of field: consists of the distance between the farthest point and the closest point of the object that appears sharp in an image;
- Shutter speed: this is the time the optical sensor takes to capture the image;
- Illumination: in order to obtain a suitable image for the use of correlation techniques, the aperture of the lens diameter and the exposure time, and therefore, to maximize light intensity, should be minimized;
- Frame rate: in ultra high speed camera, if the sensor resolution is reduced, that is, if the number of active sensors in the matrix is reduced, it is possible to perform a recording with a higher frame rate (Longana, 2014).

4.3.1.1 Sensors

In the last decade, with the development and improvement of devices for capture through electromagnetic radiation, it has become possible to develop sensors capable of recording images with higher quality, less time and at different visible light frequencies (Longana, 2014). High speed cameras are all manufactured using similar technology (Reu, 2011). However, there are

two similar technologies of digital image sensors: CCD and CMOS. The CCD sensor consists of a coupled charge device that is made up of a photoactive region where the electric charge is proportional to the intensity of light. In an array of digital signals, each pixel corresponds to a sensor of the CCD array. The CMOS sensor comprises a set of sensor arrays based on complementary metal oxide semiconductors that are used to capture light energy at a high frame rate (Longana, 2014).

Recently, three other types of digital imaging sensors have emerged, such as ISIS CCD, FTCMOS and Kirana. The use of these new technologies eliminates problems related to image distortion introduced by rotating mirror cameras and beam splitters (Reu, 2011).

ISIS CCD technology uses a CCD type storage image sensor that features a built-in memory in the detector itself. This type of sensor consists of a photo-active area of each small pixel and a high energy consumption. At low or intermediate frame rates, it is impossible to set short exposure times, which leads to image blur.

The FTCMOS digital imaging sensor uses CMOS sensor technology, which consists of an array of pixels and two spatially separated memory arrays. This configuration allows hiding the region of the memory with a shield for the light, soon the degradation of this caused by the high illumination does not occur.

The Kirana sensor combines the advantages of CCD and CMOS. CCD sensors have a limited data reading because they read data from each pixel through a single reading, while CMOS sensors can read data from multiple pixels simultaneously. The energy consumption of the CCD sensors is higher compared to the consumption of the CMOS sensors. In terms of image quality and sensitivity to light, CCD sensors show advantages over CMOS sensors (Zhu, 2015).

4.3.1.2 Shimadzu HPVX ultra high speed camera

Ultra high speed camera used in the test is a Shimadzu HPVX camera (figure 4.9). This technology incorporates a high speed FTCMOS image sensor, which employs CMOS image sensor technology. It is capable of recording 10 million images per second, so this camera allows users to view a wide variety of ultra-high-speed phenomena that previously could not be viewed (Kondo et al., 2013). The camera records 128 images at 5 Mfps. In the future, an improvement in ultra high speed camera technology is expected, with larger pixel arrays, more frames captured and longer recording time, reducing measurement errors and allowing more complex experimental trials to be developed (Fletcher and Pierron, 2018).

Table 4.1: Shimadzu HPVX camera specifications.

Sensor	FTCOMS
Pixel array size	400×128
Total frames	128
Lens	Sigma 105 mm
Flash	Bowers Gemini 1000Pro

4.4 Virtual Fields Method

4.4.1 Virtual Works Principle

The method of the virtual works is based on the principle of virtual works, according to the expression:

$$-\int_{V_m} \sigma : \varepsilon^* \mathrm{d}V + \int_{\partial V_m} \vec{T}.\vec{u}^* \mathrm{d}S = \int_{V_m} \rho \vec{a}.\vec{u}^* \mathrm{d}V \tag{4.9}$$

where σ represents the Cauchy stress tensor, $\vec{T}$ is the Cauchy stress vector acting on the boundary surface ∂V_m, $\vec{u}^*$ a vector function defined as the field of virtual displacements, ε^* the virtual strain tensor, ρ the density of the material, $\vec{a}$ is the acceleration vector that is given by the second-order derivative of the displacement vector ($\vec{a} = \partial^2 \vec{u}/\partial t^2$). The operator "." represents the scalar product of vectors, while ":" represents the scalar product of arrays. This equation is verified for any cinematically permissible virtual field (Grédiac et al., 2006) and expresses the global dynamic equilibrium of a given solid (Pierron et al., 2011).

Subsequently, some simplifying hypotheses were considered, such as:

- density, thickness and stiffness are constant in space;
- the kinematic fields are uniform in the direction of sample thickness;
- the sample is in plane stress state.

Under these conditions, the Virtual Works Principle (equation 4.9) takes the form following:

$$-\int_S \sigma : \varepsilon^* \mathrm{d}S + \int_{\partial l} \vec{T}.\vec{u}^* \mathrm{d}l = \rho \int_S \vec{a}.\vec{u}^* \mathrm{d}S \tag{4.10}$$

In this equation, S represents the surface of the region of interest, l the boundary boundaries. Then, it is necessary to replace the tension tensor with a constitutive model of the material, the most common being the isotropic or orthotropic elastic linear (Fletcher and Pierron, 2018).

There are two methods used to introduce this principle. The first method is more generic because it corresponds to the weak form of equilibrium equations. The second method is based on calculating the work done by a load when a virtual offset is applied to a solid.

4.4.1.1 Method 1: From Local Equilibrium Equations to the Virtual Work Principle

Based on equilibrium equations, which are valid at any point in the domain under consideration. These equations can be multiplied by any arbitrary function denoted by g_i, $i = 1 \ldots 3$. These products yield three equations that can be added to give the following equation:

$$\int_V \sigma_{ij,j} g_i \mathrm{d}V + \int_V b_i g_i \mathrm{d}V = \int_V \rho a_i g_i \mathrm{d}V \tag{4.11}$$

Then a piecewise integration is performed to eliminate the stress divergence involved in the first integral, as shown below

$$\int_V (\sigma_{ij} g_i)_{,j} \, \mathrm{d}V - \int_V \sigma_{ij} g_{i,j} \, \mathrm{d}V + \int_V b_i g_i \mathrm{d}V = \int_V \rho a_i g_i \mathrm{d}V \tag{4.12}$$

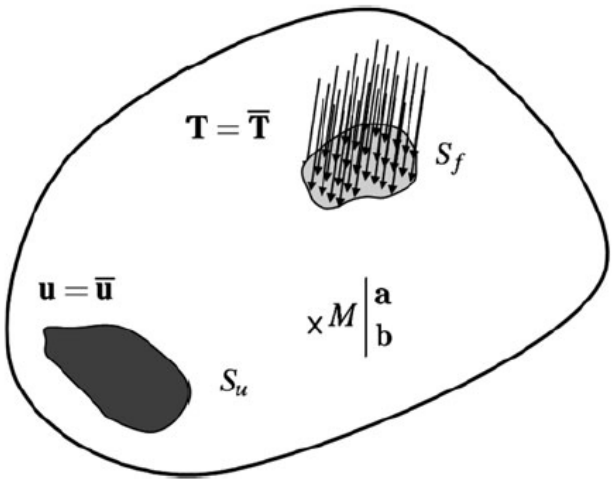

Figure 4.10: Solid shape subject to mechanical load (Pierron and Grédiac, 2012).

Subsequently, several integrations are performed, thus leaving the equation written as follows:

$$-\int_V \sigma_{ij} g_{i,j}^{sym} \mathrm{d}V + \int_S T_i g_i \mathrm{d}S + \int_V b_i g_i \mathrm{d}V = \int_V a_i g_i \mathrm{d}V \tag{4.13}$$

Equation 4.13 is mentioned as the weak form of equilibrium equations. It is weakly named because the order of continuity required to obtain an acceptable solution of this equation is smaller because the order of the derivatives is smaller. S can be divided into several subsurface, in which case S will be replaced by S_f, on which the load is applied. In this case, the equation can be described as follows:

$$-\int_V \sigma_{ij} g_{i,j}^{sym} \mathrm{d}V + \int_{S_f} T_i g_i \mathrm{d}S + \int_V b_i g_i \mathrm{d}V = \int_V \rho a_i g_i \mathrm{d}V \tag{4.14}$$

4.4.1.2 Method 2: Principle of Virtues through Charge

It is now considered a second method for introducing the principle of virtual work. Taking into account the body shown in figure 4.10, it is subject to applied forces, T, at its limit, S_f, and to volumetric forces, b, acting on its mass, V. If the body moves, a certain distribution of acceleration. Due to these accelerations, the body can have a multitude of different configurations that satisfy the displacement boundary conditions. These configurations induce a certain displacement distribution relative to the actual location of the body points. Since this offset is referred to as the virtual offset, denoted by u^*.

This virtual offset is distinct from the actual offset, u, which occurs when the defined load is applied. Actual displacement is measured relative to the initial setting, which is defined when the body is at rest, while virtual displacement is considered relative to the actual location of the body points once the load has been applied. It is now considered the virtual work performed by the load when the body is subject to a virtual displacement. Since virtual work is defined as the work performed by the load in the field of virtual displacement, the following equation is defined:

$$W^* = \int_S \bar{\mathbf{T}} \cdot \mathbf{u}^* \mathrm{d}S + \int_V \mathbf{b} \cdot \mathbf{u}^* \mathrm{d}V - \int_V \rho \mathbf{a} \cdot \mathbf{u}^* \mathrm{d}V \quad \forall \mathbf{u}^* KA \tag{4.15}$$

After several integrations it is possible to obtain the equation that leads to the principle of virtual work:

$$\int_V \sigma : \varepsilon^* \mathrm{d}V + \int_V \bar{\mathbf{T}} \cdot \mathbf{u}^* \mathrm{d}V + \int_V \mathbf{b} \cdot \mathbf{u}^* \mathrm{d}V = \int_V \rho \mathbf{a} \cdot \mathbf{u}^* \mathrm{d}V \quad \forall u^* KA \tag{4.16}$$

The following definitions are generally presented:

$$\begin{cases} W^*_{int} = \int_V \sigma : \varepsilon^* \mathrm{d}V & \text{Internal virtual work} \\ W^*_{ext} = \int_V \bar{T} \cdot u^* \mathrm{d}S + \int_V b \cdot u^* \mathrm{d}V & \text{External virtual work} \\ W^*_{acc} = \int_V \rho a \cdot u^* \mathrm{d}V & \text{Virtual work done by the acceleration} \end{cases} \tag{4.17}$$

Thus, equation 4.16 can be described as follows (Pierron and Grédiac, 2012):

$$W^*_{int} + W^*_{ext} = W^*_{acc} \quad \forall u^* KA \tag{4.18}$$

Thus two different methods were demonstrated, both capable of introducing the principle of virtual works. Being a more mathematical and a more physical method.

4.4.2 Constitutive equation of elastic linear behaviour

Given the plane state of stress, in indexed notation, the stress tensor (σ) and the strain tensor (ε) can be denoted by (Pierron and Grédiac, 2012):

$$\sigma : \begin{bmatrix} \sigma_x \\ \sigma_y \\ \sigma_s \end{bmatrix} \quad \varepsilon : \begin{bmatrix} \varepsilon_x \\ \varepsilon_y \\ \varepsilon_s \end{bmatrix} \tag{4.19}$$

Optical field techniques allow measurements on the external surface of the test specimen, so it is necessary to ensure that the external surface response represents the volume. In this way, thin plates subjected to a flat state of stress are used. The field of stresses relates to the field of deformations through the constitutive equations. The relationship between the stress and the linear deformation of a thin plate consisting of an orthotropic material subjected to a plane stress state according to the Hooke Law can be expressed by:

$$\begin{bmatrix} \sigma_x \\ \sigma_y \\ \sigma_s \end{bmatrix} = \begin{bmatrix} Q_{xx} & Q_{xy} & 0 \\ Q_{xy} & Q_{yy} & 0 \\ 0 & 0 & Q_{ss} \end{bmatrix} \begin{bmatrix} \varepsilon_x \\ \varepsilon_y \\ \varepsilon_s \end{bmatrix} \tag{4.20}$$

where Q_{ij} are the stiffness matrix components in the material coordinate system, σ_i, $(i = x, y, s)$ the stress tensor components and ε_i the strain tensor components. In the case of constitutive models for orthotropic materials a global coordinate system is defined. Figure 4.11 represents the global and local coordinate systems, where $x - y$ is the global coordinate axis system and θ represents the angle between the two coordinate systems. The local coordinate system is also defined as the axis system that displays the fibre orientation of the material.

For a material with isotropic elastic linear behaviour the equation 4.19 is simplified to:

$$\begin{bmatrix} \sigma_x \\ \sigma_y \\ \sigma_s \end{bmatrix} = \begin{bmatrix} Q_{xx} & Q_{xy} & 0 \\ Q_{xy} & Q_{xx} & 0 \\ 0 & 0 & \dfrac{Q_{xx} - Q_{xy}}{2} \end{bmatrix} \begin{bmatrix} \varepsilon_x \\ \varepsilon_y \\ \varepsilon_s \end{bmatrix} \tag{4.21}$$

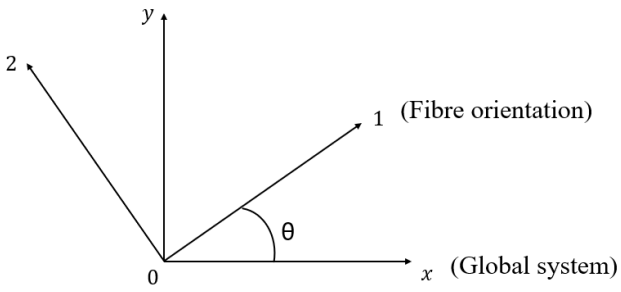

Figure 4.11: Global and fibre coordinate system.

on what,

$$\begin{cases} Q_{xx} = Q_{yy} \\ Q_{xy} = Q_{yx} \\ Q_{ss} = \dfrac{Q_{xx} - Q_{xy}}{2} \end{cases} \tag{4.22}$$

Thus, the constitutive equations for isotropic materials require only two independent parameters, Q_{xx} and Q_{xy}. These components can be described as a function of engineering constants, Young's modulus (E) and Poisson's ratio (ν) through the following expressions:

$$\begin{cases} \nu = Q_{xy}/Q_{xx} \\ E = Q_{xx}(1-\nu^2) \end{cases} \tag{4.23}$$

Substituting the constitutive law described earlier in the principle of virtual work (equation 4.9) gives the following equation:

$$\begin{aligned} Q_{xx}\int_S(\varepsilon_x\varepsilon_x^* + \varepsilon_y\varepsilon_y^* + \frac{1}{2}\varepsilon_S\varepsilon_S^*)\mathrm{d}S + Q_{xy}\int_S(\varepsilon_x\varepsilon_y^* + \varepsilon_y\varepsilon_x^* - \frac{1}{2}\varepsilon_S\varepsilon_S^*)\mathrm{d}S \\ = \int_{\partial S} T_i u_i^* \mathrm{d}L - \int_S \rho a_i u_i^* \mathrm{d}S;\ i \in (x,y) \end{aligned} \tag{4.24}$$

In orthotropic materials, the constitutive equations depend on four independent parameters, Q_{xx}, Q_{xy}, Q_{yy} and Q_{ss}. In the global coordinate system, the relationship between stress and strain is given by the following expression:

$$\begin{bmatrix} \sigma_x \\ \sigma_y \\ \sigma_s \end{bmatrix} = \begin{bmatrix} Q_{xx} & Q_{xy} & Q_{xz} \\ Q_{xy} & Q_{yy} & Q_{yz} \\ Q_{xz} & Q_{yz} & Q_{ss} \end{bmatrix} \begin{bmatrix} \varepsilon_x \\ \varepsilon_y \\ \varepsilon_s \end{bmatrix} \tag{4.25}$$

Substituting in the equation 4.25 the components of the stiffness for the equivalent expressions as a function of Young's modulus and Poisson's ratio, we get the expression:

$$\begin{bmatrix} \sigma_x \\ \sigma_y \\ \sigma_s \end{bmatrix} = \begin{bmatrix} \dfrac{E_x}{1-\nu_{xy}\nu_{yx}} & \dfrac{-\nu_{yx}E_x}{1-\nu_{xy}\nu_{yx}} & 0 \\ \dfrac{-\nu_{xy}E_y}{1-\nu_{xy}\nu_{yx}} & \dfrac{E_y}{1-\nu_{xy}\nu_{yx}} & 0 \\ 0 & 0 & G_{xy} \end{bmatrix} \begin{bmatrix} \varepsilon_x \\ \varepsilon_y \\ \varepsilon_s \end{bmatrix} \tag{4.26}$$

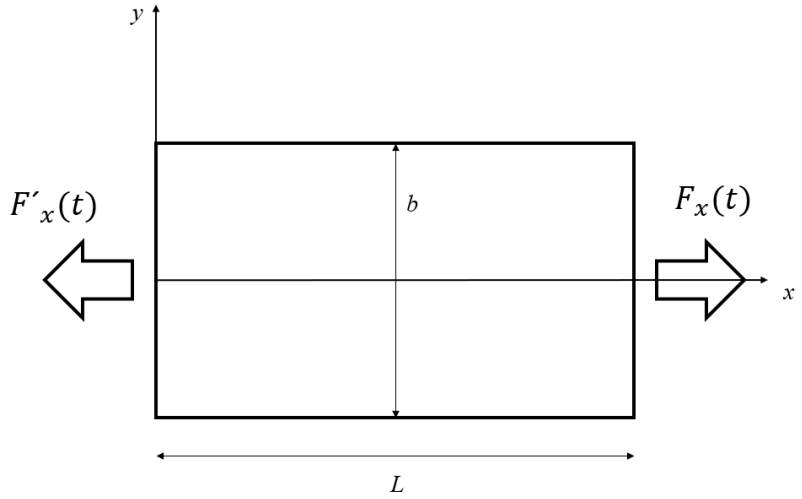

Figure 4.12: Schematic representation of a dynamic uniaxial test, adapted from (Pierron et al., 2014).

Thus, the four stiffness components relate to Young's modulus and Poisson's ratio through the following mathematical equations:

$$\begin{cases} E_x = Q_{xx} - \dfrac{Q_{xy}^2}{Q_{yy}} \\ E_y = Q_{yy} - \dfrac{Q_{xy}^2}{Q_{xx}} \\ \nu_{xy} = \dfrac{Q_{xy}}{Q_{yy}} \\ G_{xy} = Q_{SS} \end{cases} \tag{4.27}$$

Poisson's ratio can also be related to Young's modulus with the following expression (Zhu, 2015):

$$\nu_{yx} = \nu_{xy} \frac{E_y}{E_x} \tag{4.28}$$

The objective is to identify the stiffness components, such as Q_{xx}, Q_{xy}, Q_{yy} and Q_{ss}, which are related to E and ν, which are necessary for possible identification of the stress-strain curve of the material under study (Fletcher and Pierron, 2018).

4.4.2.1 Using acceleration as a load cell

In order to describe the concept of using acceleration as a load cell, one must take into account the configuration of figure 4.12. Assuming that the material under study is homogeneous and has a density called ρ. An external time dependent force is applied to the right end of the thin sample of thickness h. Considering that L is the length of the sample and b is the width. In this scheme a load cell is used to measure the load exerted at the other end of the sample (Zhu, 2015).

According to Newton's Law, the following equation can be written:

$$F_x + F'_x = \rho h \int_0^L \int_{-b/2}^{b/2} a_x(x,y)dxdy \tag{4.29}$$

Where x and y are referred to as the field of view coordinates, F_x is considered to be the applied external force and F'_x is taken to be the force measured through the load cell at a given moment and a_x is designated as the longitudinal acceleration.

The forces applied at the ends of the sample may be expressed as:

$$\begin{aligned} F_x(t) &= h \int_{-b/2}^{b/2} \sigma_x(x = L, y, t)dy \\ F'_x(t) &= -h \int_{-b/2}^{b/2} \sigma_x(x = 0, y, t)dy \end{aligned} \tag{4.30}$$

The total deformation of the specimen is measured in a large number of spatially distinct areas, but with similar sizes. Thus, if the spatial density of these measurements is high enough, equation 4.30 can be described as follows:

$$\rho h \int_0^L \int_{-b/2}^{b/2} a_x(x,y)dxdy \approx \rho L b h \bar{a}_x(x) \tag{4.31}$$

In this equation $\bar{a}_x$ is called the spatial average of the acceleration component x over the study region. Thus, equation 4.29 can be rewritten as follows:

$$F_x + F'_x = m\bar{a}_x(x) \tag{4.32}$$

Considering m as the mass of the sample under study. Associating equations 4.30 and 4.32, if the force F'_x and the acceleration field are measured simultaneously for any transverse part along the x axis, we have the following expression:

$$bh\bar{\sigma}_x(x,t) = \rho x b h \bar{a}_x(x) - F'_x \tag{4.33}$$

In this expression, $\bar{\sigma}_x(x,t)$ it represents the mean of the longitudinal stress over the cross-section of the region of interest along the longitudinal axis of the sample and $\bar{a}_x(x)$ represents the spatial average of the longitudinal acceleration over the section between the free end and the cross-section of the region of interest. Equation 4.33 shows that while the force of each end and the acceleration fields are measured simultaneously, the mean longitudinal stress can be produced at any cross section along the x axis, where the density of the material is known (Zhu, 2015). In this way, it is possible to construct the stress field, and later, the average strain, calculated by the strain measured in the section of interest, is obtained. Thus it is possible to develop the local stress-strain curves corresponding to each transverse region. The modulus of elasticity and the tensile strength of the material can be removed from the aforementioned curves without the need to use any a priori constitutive model (Pierron et al., 2014). If the forces F_x or F'_x are not measured, the analysis shown above would elaborate an equation with two unknowns, in which both could not be calculated. In cases where only one external force is applied at one end of the sample, equation 4.33 can be simplified to the following expression:

$$\bar{\sigma_x}(x,t) = \rho x \bar{a_x}(x) \tag{4.34}$$

The field of mean stresses at any point along the longitudinal axis of the sample can be restructured from the acceleration field without the need for any external force measurement. Thus, stress-strain curves can be constructed at any sample position to be used to extract the modulus of elasticity (Zhu, 2015).

4.4.3 Virtual Fields Method Using Inertial Forces

Equation 4.9 represents the principle of virtual works on dynamic. Most existing full-field measurement techniques only allow deformation on the outer surface of the body. Therefore, samples need to be designed so that the surface response is representative of the volume response which, however, is a standard for material testing. Generally, a thin plate is used under a flat state of tension. In the case of experimental tests where h represents the thickness of the volume specimen V_m and the flat surface S, the principle of virtual works equation can be described as follows:

$$-h\int_S \sigma : \varepsilon^* \mathrm{d}S + h\int_{\partial S} \vec{T}.\vec{u}^* \mathrm{d}L = h\int_S \rho\vec{a}.\vec{u}^* \mathrm{d}S \tag{4.35}$$

In equation 4.35, the first member of the expression is called the internal virtual work, the second member represents the external virtual work, and the third member is the virtual work of inertial forces (Zhu, 2015).

Given that one of the major difficulties of experimental testing of materials subjected to high strain rates is the measurement of impact forces, with the use of virtual fields these measurements are not needed. If virtual fields are used in order to nullify the contribution of the external virtual work of equation 4.35, the constituent parameters of the materials are identified without the need to measure the applied external forces, thus using the load cell acceleration described above (Pierron and Forquin, 2012).

Several virtual fields will be described to be used to identify the stiffness matrix components, which will later be related to Young's modulus and Poisson's ratio (Fletcher and Pierron, 2018).

There are three rigid body virtual fields that are capable of producing a null virtual strain field. These virtual fields, when replaced in equation 4.35, result in equations that are used to determine the stress-strain curves of the material under study. Since these equations do not require a prior formulation of a model, then this methodology is called a non parametric methodology (Aloui et al., 2008).

The first virtual field of the rigid body is presented in equation 4.36. Based on figure 3.1, the external virtual work produced by the loads F_x and F'_x at the ends of the specimen is equal to $F_x + F'_x$ since $u^*_x = 1$ and the virtual acceleration work only depends on the longitudinal component since $u^*_y = 0$.

$$\begin{cases} u^*_x = 1 \\ u^*_y = 0 \end{cases} \quad \begin{cases} \varepsilon^*_x = 0 \\ \varepsilon^*_y = 0 \\ \varepsilon^*_S = 0 \end{cases} \tag{4.36}$$

Thus, equation 4.32 expressed above can be obtained. The shear force and moment profiles can be reconstituted in the same way using the virtual fields represented in equations 4.37 and

4.38, respectively.

$$\begin{cases} u_x^* = 0 \\ u_y^* = 1 \end{cases} \quad \begin{cases} \varepsilon_x^* = 0 \\ \varepsilon_y^* = 0 \\ \varepsilon_S^* = 0 \end{cases} \tag{4.37}$$

$$\begin{cases} u_x^* = y \\ u_y^* = -x \end{cases} \quad \begin{cases} \varepsilon_x^* = 0 \\ \varepsilon_y^* = 0 \\ \varepsilon_S^* = 0 \end{cases} \tag{4.38}$$

The process of reconstituting acceleration-based stress profiles for the purpose of identifying Young's modulus, E, is accessible, but only for simple uniaxial experimental tests. In cases of heterogeneity, this method does not allow direct identification of Young's modulus. In this way a more general process will be described.

4.4.3.1 Identification of constituent parameters for an isotropic material

For a two-dimensional isotropic linear elastic model and considering that the stiffness component is constant throughout the sample, the principle of virtual Work equation can be simplified to the following mathematical expression:

$$\begin{aligned} Q_{xx} \int_S (\varepsilon_x \varepsilon_x^* + \varepsilon_y \varepsilon_y^* + \frac{1}{2}\varepsilon_S \varepsilon_S^*) \mathrm{d}S + Q_{xy} \int_S (\varepsilon_x \varepsilon_y^* + \varepsilon_y \varepsilon_x^* - \frac{1}{2}\varepsilon_S \varepsilon_S^*) \mathrm{d}S \\ = \int_{\partial S} T_i u_i^* \mathrm{d}L - \int_S \rho a_i u_i^* \mathrm{d}S;\ i \in (x, y) \end{aligned} \tag{4.39}$$

In this equation, the components of stiffness Q_{xx} and Q_{xy} are unknown, however, the stress and acceleration fields are calculated by measuring the displacement fields through spatial and temporal derivatives, respectively. External forces, T, can be measured by load cells, which is not simple to measure when material is required at high strain rates due to inertial effects.

In order to identify the two unknown stiffness components, two independent virtual fields are required. In this study, there is no need to measure the impact force that is exerted on the specimen, only the measurements of the acceleration and deformation fields become necessary. Identification of the two stiffness components for isotropic materials requires the choice of two independent virtual fields in order to nullify external virtual work, such as the virtual fields represented in equations 4.40 and 4.41:

$$\begin{cases} u_x^* = x \\ u_y^* = 0 \end{cases} \quad \begin{cases} \varepsilon_x^* = 1 \\ \varepsilon_y^* = 0 \\ \varepsilon_S^* = 0 \end{cases} \tag{4.40}$$

$$\begin{cases} u_x^* = sin(x) \\ u_y^* = 0 \end{cases} \quad \begin{cases} \varepsilon_x^* = cos(x) \\ \varepsilon_y^* = 0 \\ \varepsilon_S^* = 0 \end{cases} \tag{4.41}$$

In these two virtual fields, the displacement virtual components are null at the sample end where the external force is applied $(x = 0)$, thus the external virtual work of equation 4.39 is

nullified. Substituting the virtual field described in equation 4.40 into equation 4.39 results in the following expression:

$$Q_{xx}\int_S \varepsilon_x \mathrm{d}S + Q_{xy}\int_S \varepsilon_y \mathrm{d}S = -\int_S \rho a_x x \mathrm{d}S \tag{4.42}$$

Similarly, substituting the virtual field of equation 4.41 in equation 4.39 results in the expression:

$$Q_{xx}\int_S \cos(x)\varepsilon_x \mathrm{d}S + Q_{xy}\int_S \cos(x)\varepsilon_y \mathrm{d}S = -\int_S \rho a_x \sin(x) \mathrm{d}S \tag{4.43}$$

External forces are not involved in the previous equations. Since acceleration serves as a load cell in order to obtain the constituent parameters of the material, provided that the density is known. Combining these two equations, it becomes possible to elaborate a system of linear equations given by:

$$\mathbf{AQ} = \mathbf{B} \tag{4.44a}$$

on what,

$$\begin{aligned}
\mathbf{A} &= \begin{bmatrix} \int_S \varepsilon_x \mathrm{d}S & \int_S \varepsilon_y \mathrm{d}S \\ \int_S \cos(x)\varepsilon_x \mathrm{d}S & \int_S \cos(x)\varepsilon_y \mathrm{d}S \end{bmatrix} \\
\mathbf{Q} &= \begin{bmatrix} Q_{xx} \\ Q_{xy} \end{bmatrix} \\
\mathbf{B} &= \begin{bmatrix} -\int_S \rho a_x x \mathrm{d}S \\ -\int_S \rho a_x sin(x) \mathrm{d}S \end{bmatrix}
\end{aligned} \tag{4.44b}$$

The matrices A and B can be calculated by measuring the strain and acceleration fields. The matrix Q can be determined if the matrix A is not singular and admits its inverse: $Q = A - 1B$.

The virtual fields method makes it unnecessary to perform iterative calculations as with the finite element method. This study aims to identify the constituent parameters of materials without measuring external forces applied to the sample. VFM only requires the measurement of strain and acceleration fields derived from the measured displacement field using ultrafast chambers with sufficient spatial and temporal resolution for the study. Nowadays, the latest ultra high speed cameras are already able to provide the level of performance required to perform this analysis. To solve the principle of virtual work equation, there are a multitude of independent virtual fields that can be used. If the measured data in the strain and acceleration fields are accurate, then any set of virtual fields can be used to identify the stiffness components. However, if the data is noisy, ie not accurate, which is inevitable in experimental trials, different virtual fields will yield very diverse results (Zhu, 2015).

4.4.3.2 Identification of constitutive parameters for an orthotropic material

In the orthotropic linear elastic model, it is often considered a case where the fibers are not aligned with the global coordinate system, as illustrated in figure 4.11. In the global coordinate

system of an orthotropic linear model, the relationship between stress and strain can be described as follows:

$$\begin{bmatrix} \sigma_x \\ \sigma_y \\ \sigma_s \end{bmatrix} = \begin{bmatrix} Q_{xx} & Q_{xy} & Q_{xz} \\ Q_{xy} & Q_{yy} & Q_{yz} \\ Q_{xz} & Q_{yz} & Q_{ss} \end{bmatrix} \begin{bmatrix} \varepsilon_x \\ \varepsilon_y \\ \varepsilon_s \end{bmatrix} \tag{4.45}$$

This constitutive equation differs from the constitutive equation in the fiber orientation coordinate system described in equation 4.21, since the stiffness matrix components Q_xz and Q_yz are no longer null. Using the constitutive equations in a global coordinate system, it is difficult to identify six unknowns of the stiffness matrix. Thus, the identification of the constituent parameters of orthotropic materials is performed in a coordinate system with the orientation of the fibres of the material, since only four independent components of the stiffness matrix are involved.

In order to identify the four stiffness components in the fibre orientation coordinate system, all variables of equation 4.9 must be transformed. Virtual fields must be first developed in the global coordinate system and then transformed to the fibre orientation coordinate system. This is because the boundary conditions of the virtual fields are defined in the global coordinate system. The transformation of a virtual field in the global coordinate system to the fibre orientation coordinate system can be accomplished by the expression:

$$\vec{D_f} = C\vec{D_g} \tag{4.46}$$

Considering that $\vec{D_f}$ and $\vec{D_g}$ are vectors that represent the deformation or acceleration fields in the global coordinate and fibre orientation systems, respectively. The matrix C is called transformation matrix and can be described in the following expression:

$$C = \begin{bmatrix} \cos(\theta) & \sin(\theta) \\ -\sin(\theta) & \cos(\theta) \end{bmatrix} \tag{4.47}$$

Thus, if for an orthotropic material virtual fields are used to nullify the external virtual work, equation 4.9 can be described in the fibre orientation coordinate system as:

$$\begin{aligned} Q_{xx}\int_S \varepsilon_x\varepsilon_x^* \mathrm{d}S \; + \; Q_{xy}\int_S (\varepsilon_x\varepsilon_y^* \; + \; \varepsilon_y\varepsilon_x^*)\mathrm{d}S \; + \; Q_{yy}\int_S \varepsilon_y\varepsilon_y^* \mathrm{d}S \; + \; Q_{ss}\int_S \varepsilon_s\varepsilon_s^* \mathrm{d}S \\ = -\int_S \rho a_i u_i^* \mathrm{d}S; \; i \in (x,y) \end{aligned} \tag{4.48}$$

All quantities of equation 4.48 are expressed in the fibre orientation coordinate system. The virtual work of acceleration in the fibre orientation coordinate system is equivalent in the global coordinate system (Zhu, 2015). In order to identify the four components of the stiffness matrix, four independent virtual fields are required, and the following were chosen:

$$\begin{cases} u_x^* = x \\ u_y^* = \cos(y)\log(x+1) \end{cases} \qquad \begin{cases} \varepsilon_x^* = 1 \\ \varepsilon_y^* = -\sin(y)\log(x+1) \\ \varepsilon_S^* = \dfrac{\cos(y)}{x+1} \end{cases} \tag{4.49}$$

$$\begin{cases} u_x^* = \sin(x) \\ u_y^* = xy \end{cases} \quad \begin{cases} \varepsilon_x^* = \cos(x) \\ \varepsilon_y^* = x \\ \varepsilon_S^* = y \end{cases} \tag{4.50}$$

$$\begin{cases} u_x^* = \log(x+1) \\ u_y^* = y^2 \sin(x) \end{cases} \quad \begin{cases} \varepsilon_x^* = \dfrac{1}{x+1} \\ \varepsilon_y^* = 2y \sin(x) \\ \varepsilon_S^* = y^2 \cos(x) \end{cases} \tag{4.51}$$

$$\begin{cases} u_x^* = x^3 \\ u_y^* = \sin(y+1)x^2 \end{cases} \quad \begin{cases} \varepsilon_x^* = 3x^2 \\ \varepsilon_y^* = x^2 \cos(y+1) \\ \varepsilon_S^* = 2x \sin(y+1) \end{cases} \tag{4.52}$$

The virtual fields described above will be used for numerical simulation and experimental analysis of the experimental essay under study. Similar to the isotropic case, these virtual fields are selected in order to nullify the contribution of the virtual work of the external forces, to be cinematically admissible and which matrix A admits in reverse. Applying the virtual fields designated in equation 4.48 results in a system of equations 4.53.

$$\mathbf{AQ} = \mathbf{B} \tag{4.53a}$$

on what,

$$\begin{aligned} \mathbf{A} &= \begin{bmatrix} A_{11} & A_{22} & A_{13} & A_{14} \\ A_{21} & A_{22} & A_{23} & A_{24} \\ A_{31} & A_{32} & A_{33} & A_{34} \\ A_{41} & A_{42} & A_{43} & A_{44} \end{bmatrix} \\ \mathbf{Q} &= \begin{bmatrix} Q_{xx} \\ Q_{xy} \\ Q_{yy} \\ Q_{SS} \end{bmatrix} \\ \mathbf{B} &= \begin{bmatrix} -\int_S \rho(xa_x + \cos(y)\log(x+1)a_y)\mathrm{d}S \\ -\int_S \rho(\sin(x)a_x + xya_y)\mathrm{d}S \\ -\int_S \rho(\log(x+1)a_x + y^2\sin(x)a_y)\mathrm{d}S \\ -\int_S \rho(x^3a_x + \sin(y+1)x^2a_y)\mathrm{d}S \end{bmatrix} \end{aligned} \tag{4.53b}$$

The solution of the system of equations 4.53 goes through a solution similar to that of equation 4.45 for isotropic material. In this system of equations the matrix Q is the direct result of the

inverse of matrix A multiplied by matrix B. In these equations, the coefficients of matrix A are given by the following expressions:

$$
\begin{aligned}
A_{11} &= \int_S \varepsilon_x \mathrm{d}S & A_{12} &= \int_S (-\sin(y)\log(x+1)\varepsilon_x + \varepsilon_y)\mathrm{d}S \\
A_{13} &= \int_S -\sin(y)\log(x+1)\varepsilon_y \mathrm{d}S & A_{14} &= \int_S \frac{\cos(y)}{x+1}\varepsilon_S \mathrm{d}S \\
A_{21} &= \int_S \cos(x)\varepsilon_x \mathrm{d}S & A_{22} &= \int_S (x\varepsilon_x + \cos(x)\varepsilon_y)\mathrm{d}S \\
A_{23} &= \int_S x\varepsilon_y \mathrm{d}S & A_{24} &= \int_S y\varepsilon_S \mathrm{d}S \\
A_{31} &= \int_S \frac{1}{x+1}\varepsilon_x \mathrm{d}S & A_{32} &= \int_S (2y\sin(x)\varepsilon_x + \frac{1}{x+1}\varepsilon_y)\mathrm{d}S \\
A_{33} &= \int_S 2y\sin(x)\varepsilon_y \mathrm{d}S & A_{34} &= \int_S y^2\cos(x)\varepsilon_S \mathrm{d}S \\
A_{41} &= \int_S 3x^2\varepsilon_x \mathrm{d}S & A_{42} &= \int_S (\cos(y+1)x^2\varepsilon_x + 3x^2\varepsilon_y)\mathrm{d}S \\
A_{43} &= \int_S \cos(y+1)x^2\varepsilon_y \mathrm{d}S & A_{44} &= \int_S 2x\sin(y+1)\varepsilon_S \mathrm{d}S
\end{aligned}
\tag{4.53c}
$$

Thus, it is possible to determine the constituent parameters of an orthotropic material by VFM by measuring the strain and acceleration fields. It is feasible to determine the stress-strain curve of the material subjected to high strain rates in the inertial impact test.

4.5 Conclusion

Firstly, the image-based inertial impact test was presented as a new experimental procedure to study the constitutive parameters of materials when subjected to high strain rates. The mode of operation of the test has been described as well as its physical components.

Next, the grid method was characterized as the technique used to measure the displacement, acceleration and strain fields in the inertial impact test. The application of the grid to the surface of the study sample was described. The following was described the ultra high speed cameras currently on the market as well as their mode of operation and the considerations to take into account when setting up an image capture device. The various existing digital image sensors were portrayed, as well as the ultra high speed camera used in the experimental study performed.

Lastly, the principle of virtual work was presented as the basis of the virtual field method, and two methods used to introduce this methodology were described. Then, the constitutive equations of elastic linear behaviour for isotropic and orthotropic materials were explained, and the use of acceleration as a load cell was shown. The method of the virtual fields using inertial forces was exposed in order to identify the constituent parameters of materials without the need for measurements of applied external forces. Next, the rigid body virtual fields are demonstrated that are capable of producing a null virtual deformation field. The procedures for identifying the constituent parameters for isotropic and orthotropic materials were described.

5 | Experimental analysis

5.1 Introduction

This chapter describes the experimental analysis of the inertial impact test performed with *Pinus pinaster* Ait. wood specimens. The experimental tests were conducted at the University of Southampton. In the specimens the grid method was applied to measure the displacement fields in the test. After obtaining the experimental data, they were used in the virtual fields method, for later identification of the constitutive parameters of the wood species under study. For this analysis, two experimental tests were carried out with different specimen orientations, *RT* orientation and *TR* orientation.

First, the entire experimental test will be described, specifying the materials and dimensions of the test components. The ultra high speed Shimadzu HPV-X2 camera will be used for image capture during the impact test. The captured images will later be used in the grid method, the specifications of which will be presented in this chapter.

Next, all maps of the specimen displacements, accelerations and strains with *RT* orientation will be demonstrated for several moments. The results obtained for Young's modulus and the Poisson's ratio, that is, the constitutive parameters, for *Pinus pinaster* Ait. wood will be presented and discussed. In the end the same procedure will be done for the specimen with *TR* orientation.

5.2 Experimental procedure

In the experimental test were studied wood specimens from the *Pinus pinaster* Ait. species. The specimens of the biological material have been properly prepared so as to reduce the presence of natural wood defects and the perfect alignment of the fibers. The specimens were numbered for experimental testing, since not all specimens were used to obtain results due to the presence of defects, such as knots. Thus, the specimens chosen for the experimental tests showed no visible defects and the fibers were well oriented with the desired planes.

The experimental test begins with the transfer of the cross-grid pattern to the surface of the test specimen. This process is described in section 4.3. The fact that the grid is crossed allows to determine the displacement components perpendicular to the horizontal and vertical grid lines. In this optical technique, a grid pattern is placed on the reference surface of the specimen. In this test, the printed grids had a ratio of 5 pixels for each grid period with a 0.67 mm grid. These measurements were selected to maximize the spatial resolution of the measurements.

As shown in figure 5.1, the test consists of waveguide and projectile, both of which consist of aluminum 6061-T6. The test specimen is glued to the waveguide, which is 50 mm long and 45 mm in diameter. The projectile is launched from a gas chamber reservoir and is 25 mm long

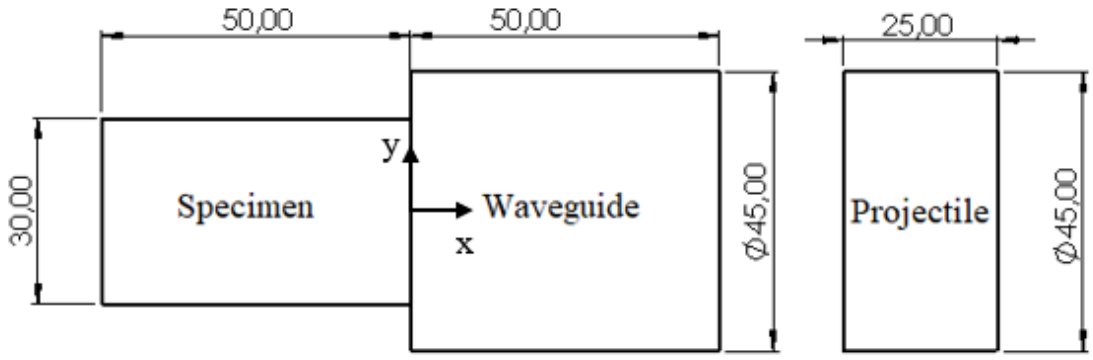

Figure 5.1: Schematic representation of the simulated test.

Table 5.1: Properties of constituent components of the image-based inertial impact test (Xavier, 2003).

	Material	E (GPa)	ρ (kg m^{-3})	ν
Waveguide Projectile	Aluminium 6061-T6	70	2700	0,30
Specimen	*Pinus pinaster Ait.*	E_L=15,10 E_R=1,91 E_T=1,01	626,73	ν_{RT}=0,59 ν_{TL}=0,05 ν_{LR}=0,47

and 45 mm in diameter. The detailed description of the IBII test can be found in section 4.2. The characteristics of these components are described in table 5.1. The density measured on the test pieces tested in the two experimental tests has an average value of 626,73 kg m^{-3}, as the density ranges between 587,73 kg m^{-3} and 671,33 kg m^{-3}. Since the projectile length is the shortest length of the components used in the test, it controls the pulse duration,that is, the pulse duration is twice the time required to travel the projectile length (Fletcher et al., 2019). These component size choices have been made to reduce the possible reflection of the projectile back to the gas chamber barrel and cause damage to it. It is desirable to maximize the input compression stress wave that is reflected as well as the tensile stress wave.

Since the transition time from the impact wave of the projectile to the specimen is quite short, the use of an ultra fast camera with a high acquisition rate is required. A Shimadzu HPV-X2 camera, which has an acquisition rate of 5 Mfps with a Sigma 105 macro lens, was used in the experimental test, previously described in section 4.3.1.

5.3 RT oriented specimen

In this experimental analysis four tests were performed with different specimens. The specimens have a size of 5 mm on the L axis, 50 mm on the R axis and 30 mm on the T axis, so they are oriented according to the RT plane shown in figure 3.6. In this section all maps of displacements, accelerations and deformations are presented. For all maps presented below, specimen 4 was selected as a typical representation of all specimens tested in this experimental test.

5.3.1 Results and discussion

The maps of the x components of the displacements obtained for a specimen with orientation RT are shown in figure 5.2. Figure 5.3 shows the maps of the displacements obtained according to the y direction. In the displacement maps δ_x you can see the one-dimensional wave entering the sample when $t = 19\mu s$ and reflecting on its edge and becoming elastic when $t = 25\mu s$. In both figures 5.2 and 5.3 it is possible to observe discontinuity zones, which are due to the rupture of the specimen that occurs in the experimental test.

The maps of the x component of acceleration for a specimen with RT orientation at various times of the experimental test are shown in figure 5.4. The maps of the y component of acceleration according to y direction are shown in figure 5.5. The accelerations were determined from second order temporal derivatives using the finite difference method.

The map of the strains according to the x direction for a specimen with RT orientation at various times of the experimental test is shown in figure 5.6. The map of the strains according to the xy direction is shown in figure 5.7. The map of the deformations according to the y direction is shown in figure 5.8. The strains were calculated based on the spatial derivatives of the displacements. And as in the accelerations, the strains was also using the finite difference method. Figure 5.9 shows the maps comparing the strains in an RT oriented specimen before and after smoothing for the E_{xx}, E_{xy} and E_{yy} components.The deformation and acceleration fields from the displacement fields were numerically derived after smoothing.

The fields of deformation clearly show the heterogeneous nature of the IBII test. It is possible to observe that different regions of the material present different amplitude of strain rates.

By observing the displacement maps, it is possible to confirm that the magnitude of the deformations in y are significantly smaller than the magnitude of the deformations in x. The deformation maps in y show that the signal is noisier than the deformation signal in x.

When identifying properties of a material at high strain rates, it is important to consider at what strain rate the material is tested. This task may be trivial for quasi-static tests but for dynamic tests at high strain rates it is a complicated task. The strain rate for dynamic tests at high strain rates will inevitably be heterogeneous and transient due to inertial effects, that is stress wave propagation. This is evident in the strain maps.

By examining the maps of the x components of the strain it is possible to verify higher strains in the zone where there are discontinuities. Due to the low anisotropy ratio that exists in the RT plane, in this analysis an isotropic model was used as an approximation.

In this experimental analysis, the data obtained in the image-based inertial impact test are then processed through the VFM, so that the constituent parameters of the material under study can be identified. In the VFM were used the virtual fields presented in equation 5.1 and equation 5.2, which allow to nullify the virtual work of the external force applied to the specimen. Thus, external force measurement using acceleration as a load cell is not required in identifying material constitutive properties as explained in section 4.4.

$$\begin{cases} u_x^* = L - x \\ u_y^* = 0 \end{cases} \quad \begin{cases} \varepsilon_x^* = -1 \\ \varepsilon_y^* = 0 \\ \varepsilon_S^* = 0 \end{cases} \tag{5.1}$$

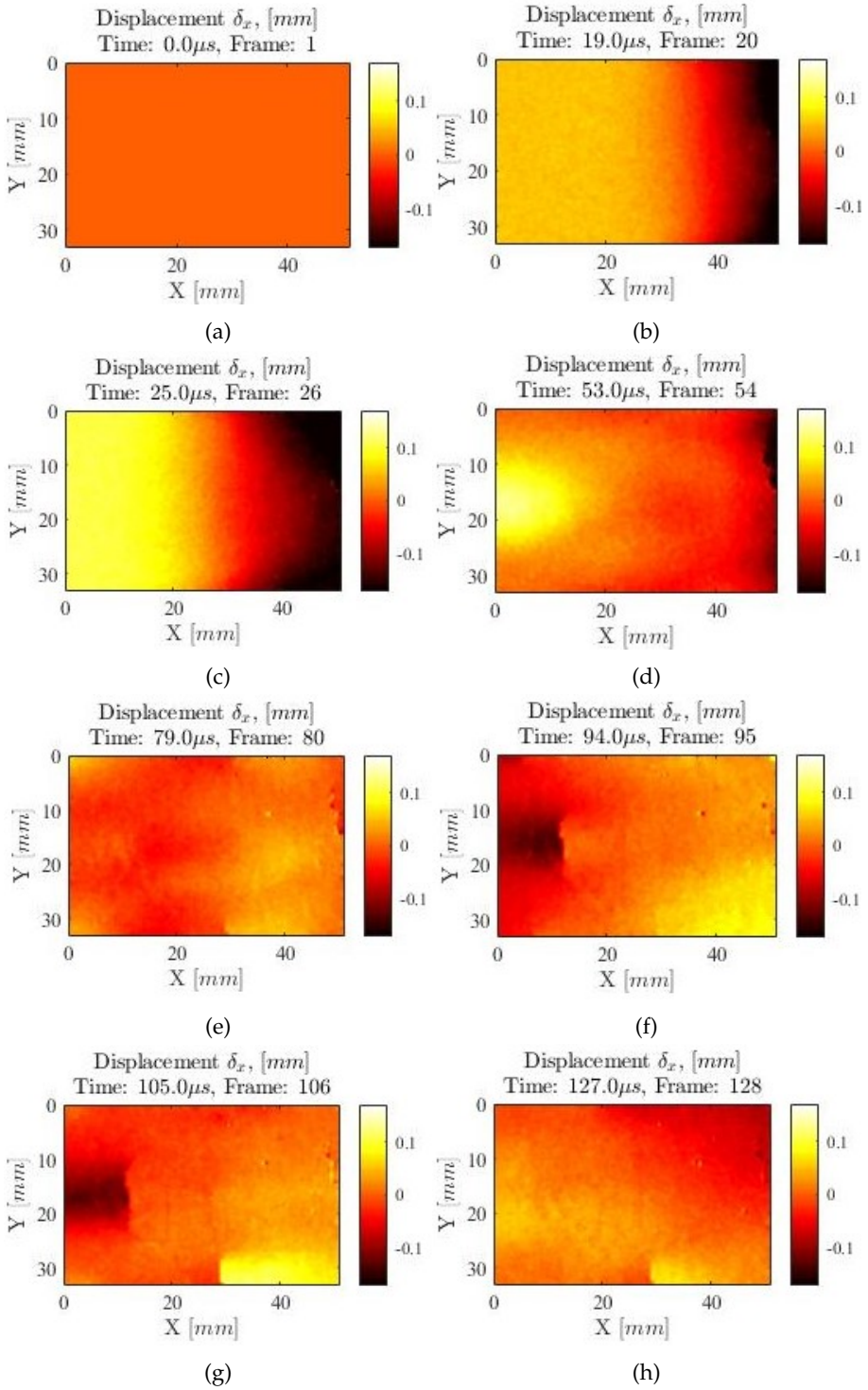

(a) (b) (c) (d) (e) (f) (g) (h)

Figure 5.2: Maps of the x components of the displacements for a specimen with RT orientation at various times. (a) $t = 0\mu s$. (b) $t = 19\mu s$. (c) $t = 25\mu s$. (d) $t = 53\mu s$. (e) $t = 79\mu s$. (f) $t = 94\mu s$. (g) $t = 105\mu s$. (h) $t = 127\mu s$.

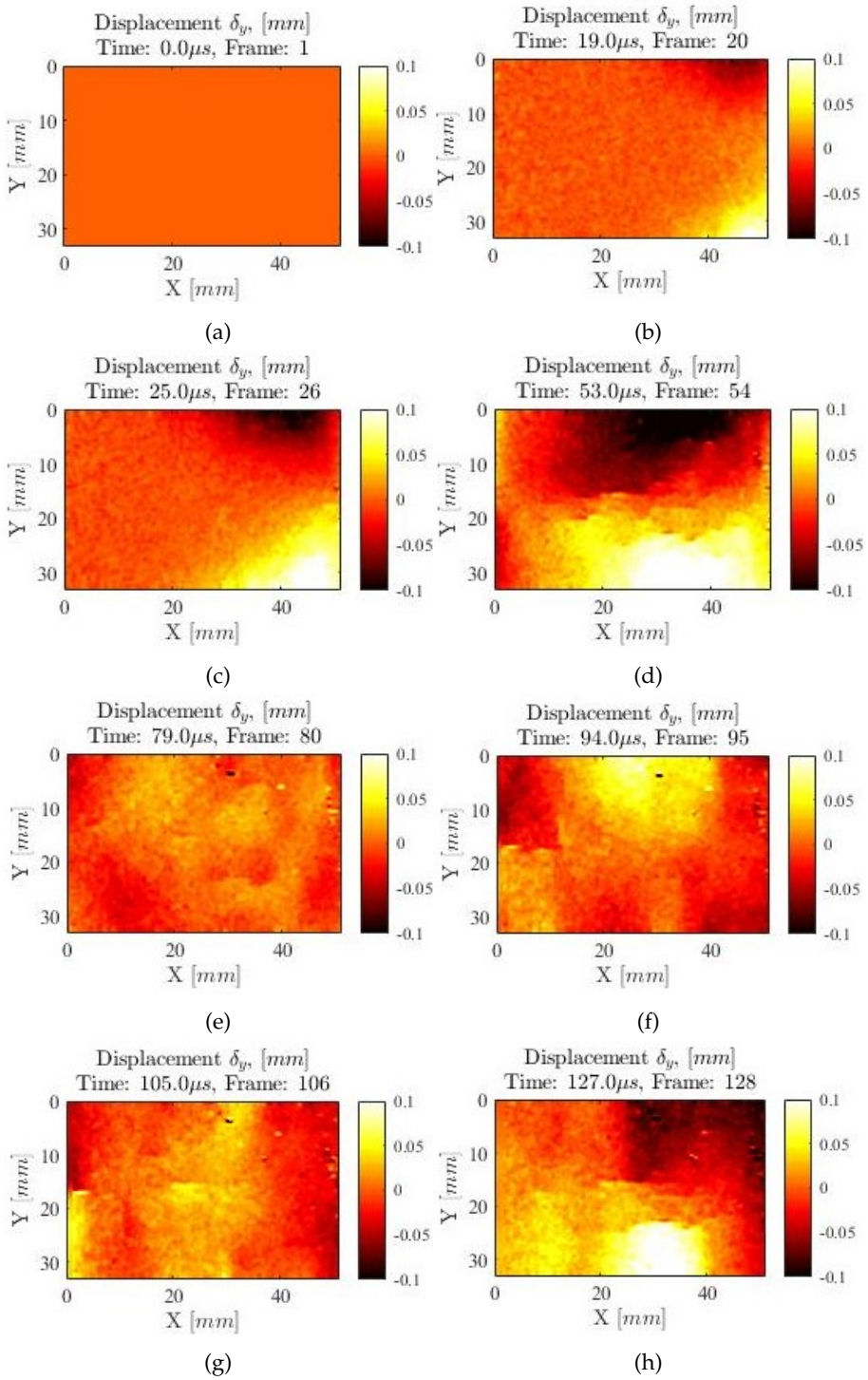

Figure 5.3: Maps of the y components of the displacements for a specimen with RT orientation at various times. (a) $t = 0\mu s$. (b) $t = 19\mu s$. (c) $t = 25\mu s$. (d) $t = 53\mu s$. (e) $t = 79\mu s$. (f) $t = 94\mu s$. (g) $t = 105\mu s$. (h) $t = 127\mu s$.

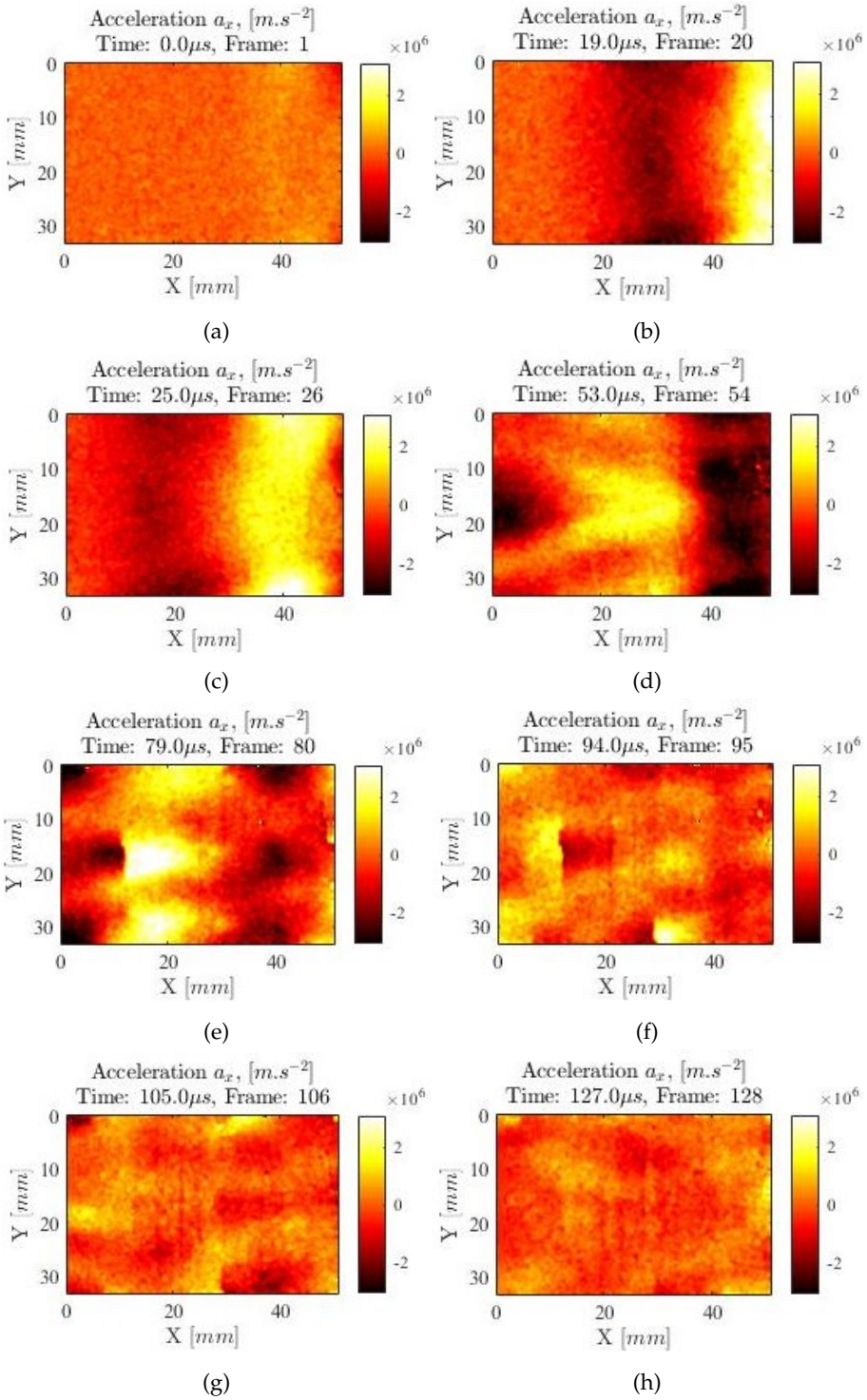

Figure 5.4: Maps of the x components of the accelerations for a specimen with RT orientation at various times. (a) $t = 0\mu s$. (b) $t = 19\mu s$. (c) $t = 25\mu s$. (d) $t = 53\mu s$. (e) $t = 79\mu s$. (f) $t = 94\mu s$. (g) $t = 105\mu s$. (h) $t = 127\mu s$.

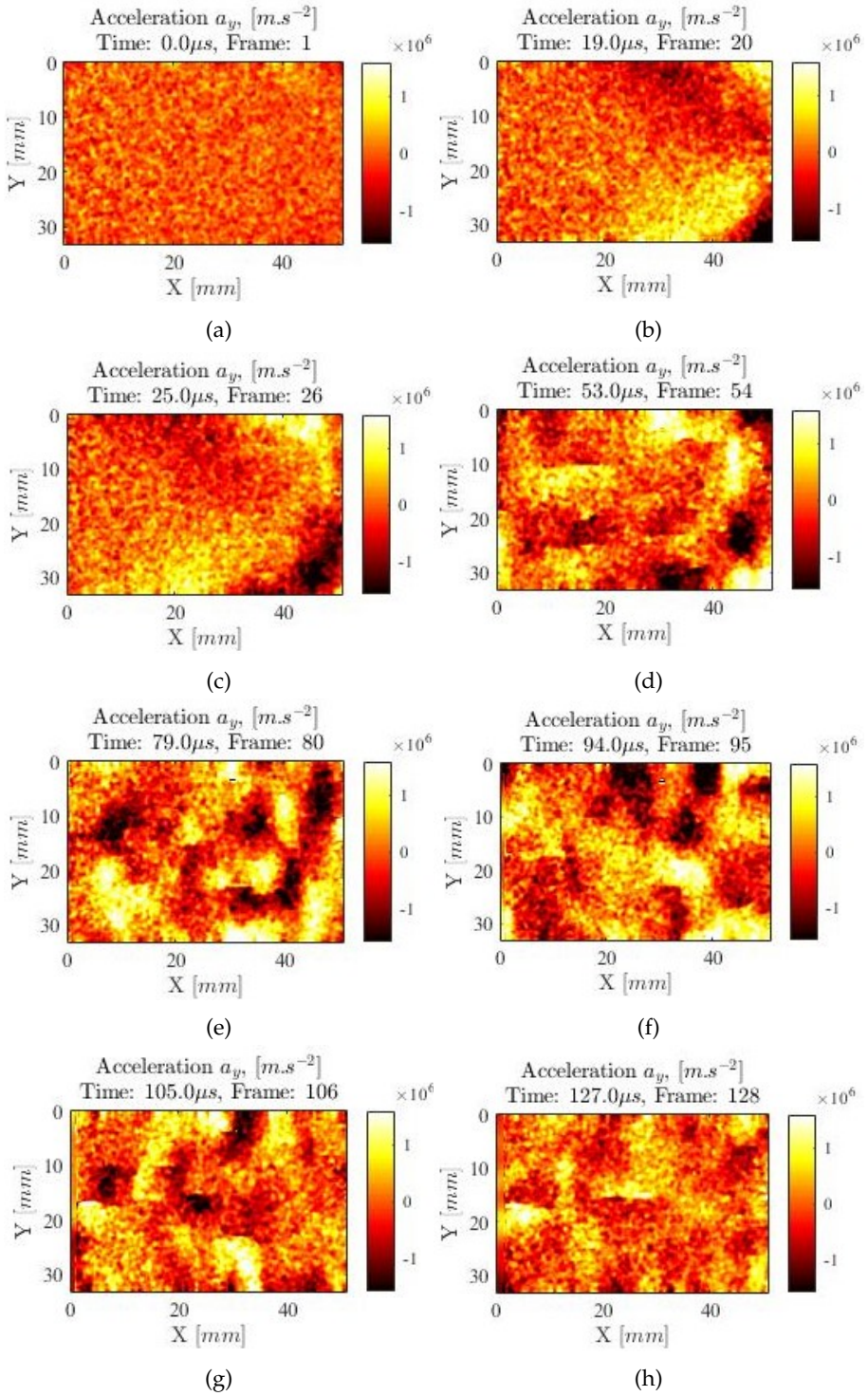

(a) (b) (c) (d) (e) (f) (g) (h)

Figure 5.5: Maps of the y components of the accelerations for a specimen with RT orientation at various times. (a) $t = 0\mu s$. (b) $t = 19\mu s$. (c) $t = 25\mu s$. (d) $t = 53\mu s$. (e) $t = 79\mu s$. (f) $t = 94\mu s$. (g) $t = 105\mu s$. (h) $t = 127\mu s$.

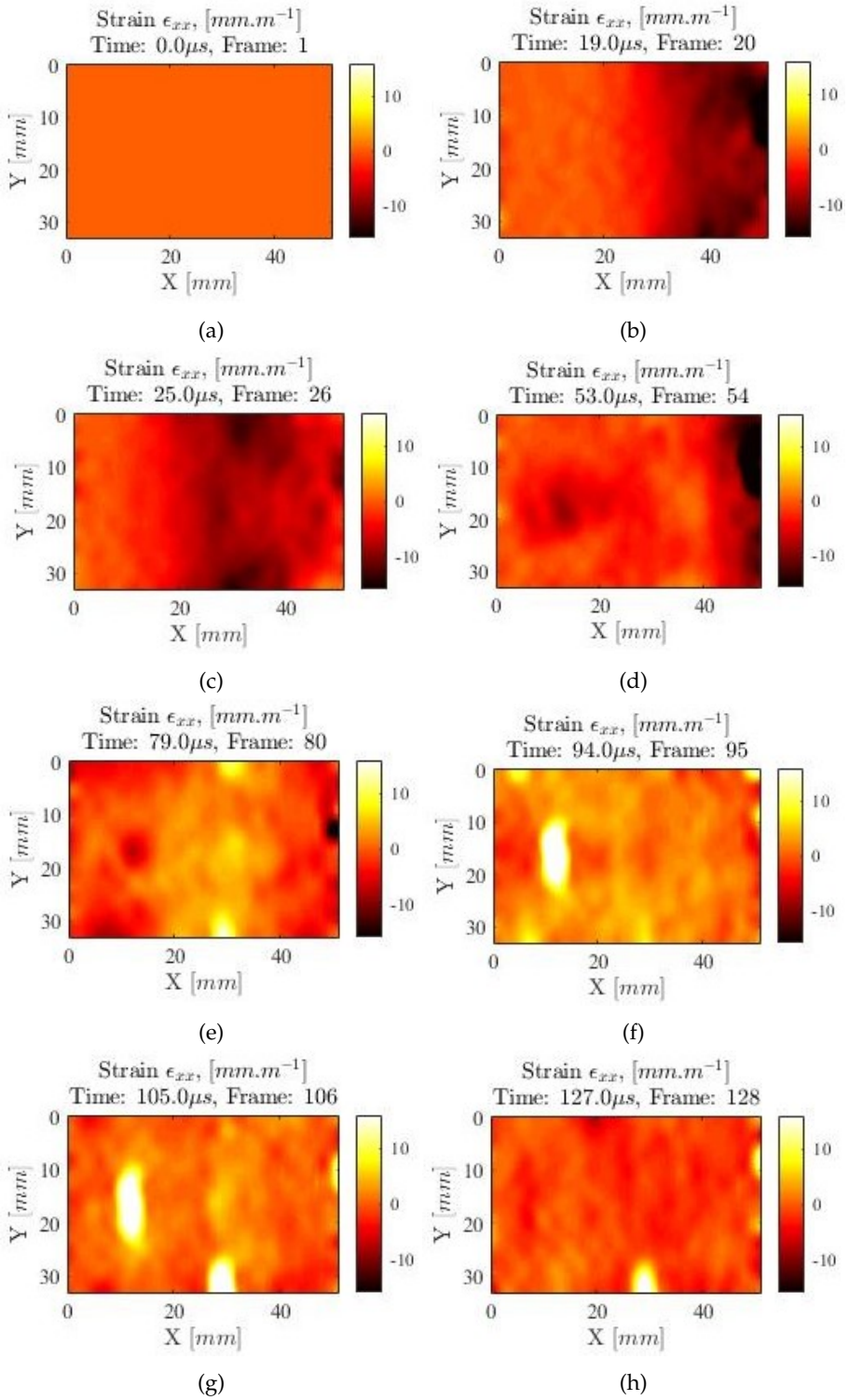

(a) (b) (c) (d) (e) (f) (g) (h)

Figure 5.6: Maps of the x components of the strains for a specimen with RT orientation at various times. (a) $t = 0\mu s$. (b) $t = 19\mu s$. (c) $t = 25\mu s$. (d) $t = 53\mu s$. (e) $t = 79\mu s$. (f) $t = 94\mu s$. (g) $t = 105\mu s$. (h) $t = 127\mu s$.

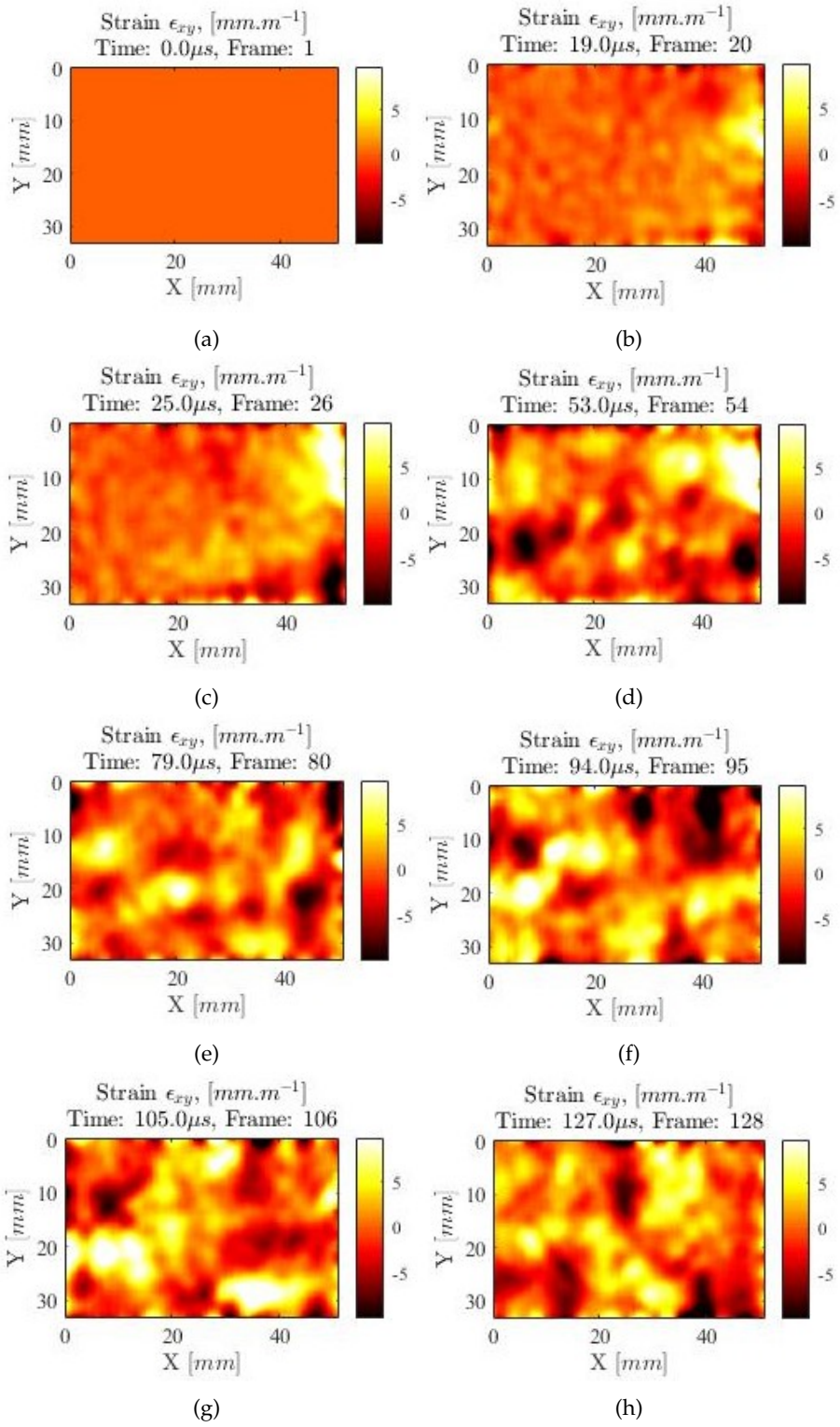

Figure 5.7: Maps of the xy components of the strains for a specimen with RT orientation at various times. ((a) $t = 0\mu s$. (b) $t = 19\mu s$. (c) $t = 25\mu s$. (d) $t = 53\mu s$. (e) $t = 79\mu s$. (f) $t = 94\mu s$. (g) $t = 105\mu s$. (h) $t = 127\mu s$.

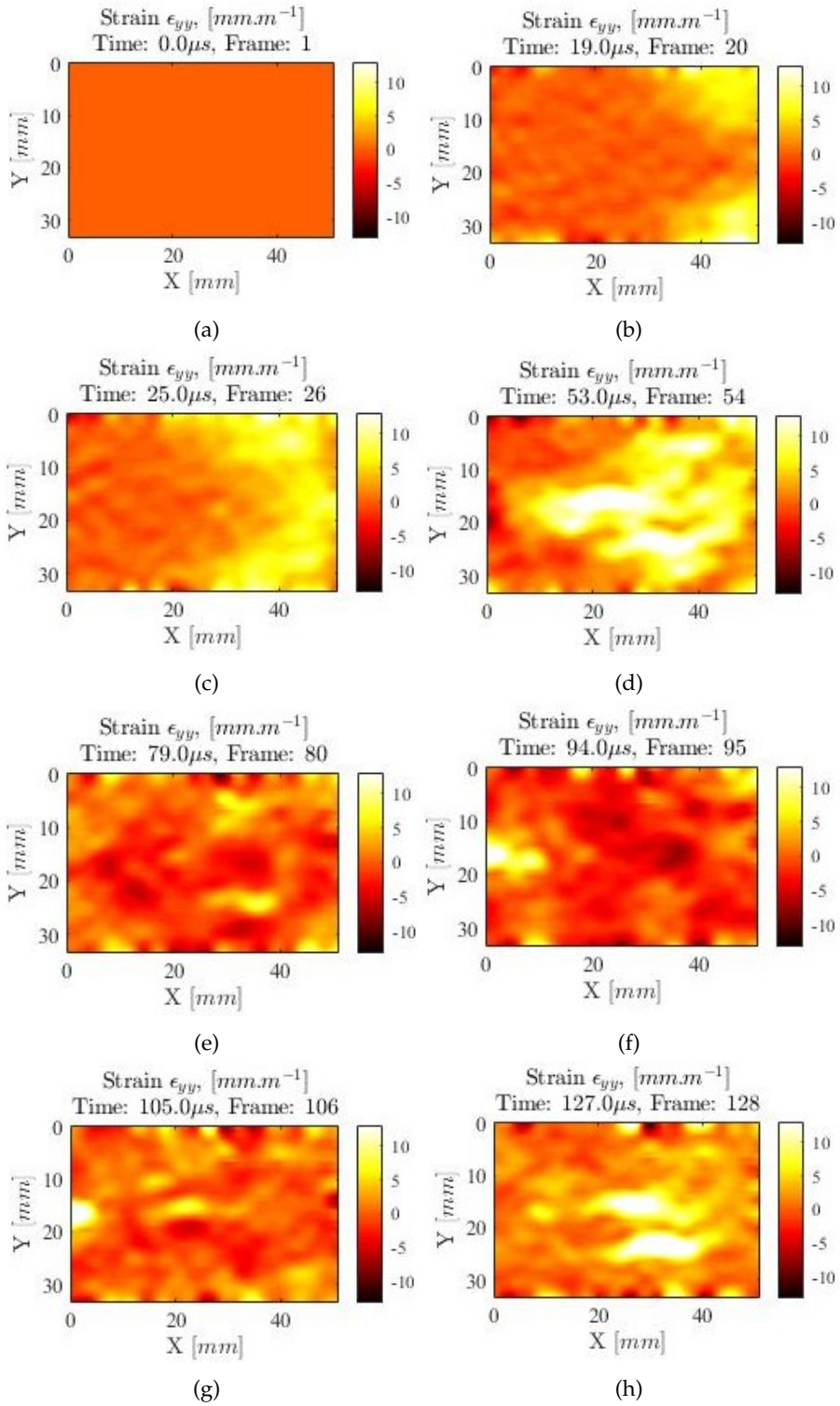

Figure 5.8: Maps of the y components of the strains for a specimen with RT orientation at various times. (a) $t = 0\mu s$. (b) $t = 19\mu s$. (c) $t = 25\mu s$. (d) $t = 53\mu s$. (e) $t = 79\mu s$. (f) $t = 94\mu s$. (g) $t = 105\mu s$. (h) $t = 127\mu s$.

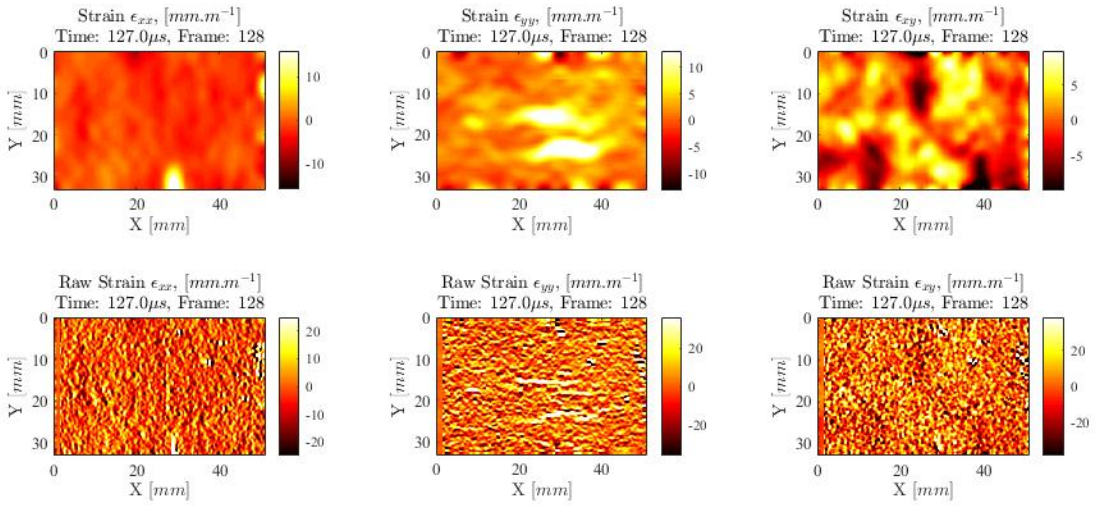

(a)

Figure 5.9: Maps of the comparison of strain on *RT* orientation specimen before and after smoothing at time $t = 180\mu s$.

$$\begin{cases} u_x^* = 0 \\ u_y^* = (L-x)\dfrac{y}{b} \end{cases} \quad \begin{cases} \varepsilon_x^* = 0 \\ \varepsilon_y^* = \dfrac{L-x}{b} \\ \varepsilon_S^* = -\dfrac{y}{b} \end{cases} \tag{5.2}$$

After the acceleration and deformation fields have been processed by the virtual field method, using a code in Matlab [1], it is possible to identify the constitutive properties of the wood. The figures 5.10 and 5.11 show the components of stiffness Q_{xx} and Q_{xy}, respectively, for the *RT* orientation specimen. In these figures it is observed that it is more difficult to identify the stiffness component Q_{xy} than Q_{xx}, as the signal stabilizes first for Q_{xx} than for Q_{xy} . This result happens because the deformation is predominantly axial, having only minor deformations and lateral accelerations.

Taking into account the four test pieces analyzed in this *RT* oriented trial, the average value for the stiffness component Q_{xx} is 2,23 GPa and the average value for the stiffness component Q_{xy} is 0,80 GPa.

Considering the constitutive parameters of the wood of *Pinus pinaster* Ait. species presented in table 5.1, it is considered that the Young's modulus in the radial direction (E_R) is 1,91 GPa and the Poisson's ratio for the transverse plane (ν_{RT}) is 0,59. The values obtained for the specimens analysed in *RT* orientation for the time interval under study are presented in table 5.2. In this analysis, the values of Young's modulus and Poisson's ratio show a variation of 1,571% and variation of 11,667%. These values are in relation to the reference values presented above. The results obtained in the experimental test are very promising for the first application of this methodology to wood of *Pinus pinaster* Ait. species when subjected to high strain rates. Since there is heterogeneity of the previously described kinematic fields, it is difficult to assign a single value to the strain rate at which the dynamic test occurs. It is important to note that high axial

[1] https://eprints.soton.ac.uk/

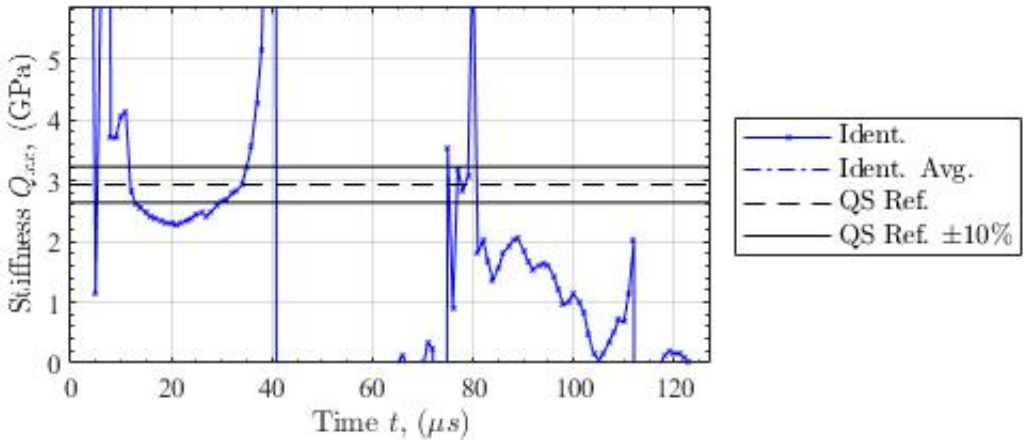

(a)

Figure 5.10: Results obtained for stiffness component Q_{xx} over time t on RT orientation specimen.

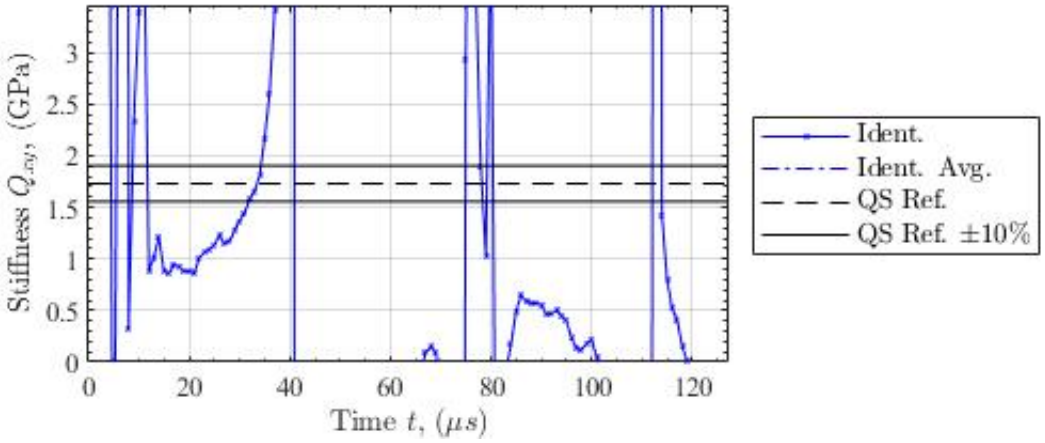

(a)

Figure 5.11: Results obtained for stiffness component Q_{xy} over time t on RT orientation specimen.

strain is also reflected in high strain rates. The virtual fields chosen may not be the best results, as there is no guarantee that they are the best virtual fields to reduce the associated noise in the experimental trial (Blitterswyk et al., 2018).

Figure 5.12 compares the Young's modulus determined for various x positions of the specimen with its reference value and the calculated mean value. In figure 5.13 it is possible to analyse the Young's modulus as a function of time t. In this graph the Young's modulus is compared with its reference value and its mean value determined in the experimental analysis. Figure 5.13 demonstrates that this method only stabilizes approximately $t = 10\mu s$. This is because there is a need for sufficient information in the acceleration and deformation fields to be able to identify the constitutive properties of the material, in this case Young's modulus. This identification only occurs when a significant portion of the stress wave enters the specimen. In this figure it is also possible to observe, through the signal, the compression and traction that happens in the specimen.

Table 5.2: Results obtained for the constitutive parameters of *Pinus pinaster* Ait. wood for different specimens with orientation in the *RT* plane.

Specimens	Young's modulus (E_R) (GPa)	Poisson's ratio (ν_{RT})
1	1,962	0,505
2	1,876	0,595
3	1,903	0,692
4	1,893	0,590
Average	1,909	0,596
Standard deviation	0,032	0,066
Coefficient of variation	1,6 %	11,7 %

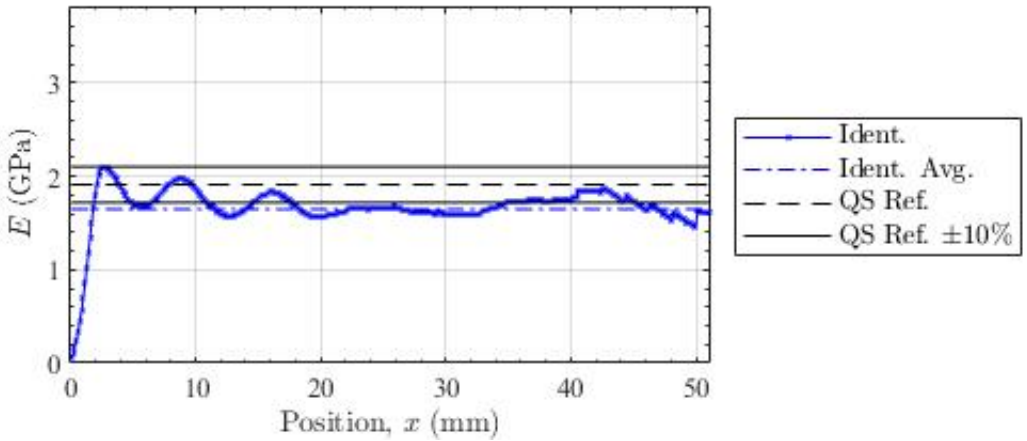

(a)

Figure 5.12: Results obtained for the Young's modulus along x position on *RT* orientation specimen.

In this experimental analysis, an isotropic model was used in the VFM to obtain the constitutive parameters of *Pinus pinaster* Ait. wood when subjected to high strain rates. This is a valid approximation as the *RT* orientation plane has a low anisotropy ratio. However, this approach leads to some error in identifying the constituent parameters of the material. A possible way to improve the results would be to use an orthotropic model in VFM. In this test it would not be possible to successfully identify the constituent parameters due to the lack of heterogeneity that this transverse plane presents.

Since wood is a biological material with a highly complex structure, its properties vary significantly in space. Since in the experimental test only a single value of the constituent parameters is identified for each moment, this methodology may not be appropriate to identify the properties of a material with spatial variations for each moment. The inertial impact test and all the surrounding methodology prove to be very versatile when the objective is to identify the constitutive properties of the material as a function of the analysis time (Blitterswyk et al., 2018). In order to obtain the spatial variations of the constitutive parameters of wood, it would be appropriate to use the load cell acceleration methodology mentioned earlier in section 4.4. This methodology allows the material properties to be measured. in different cross sections along the length of the test piece.

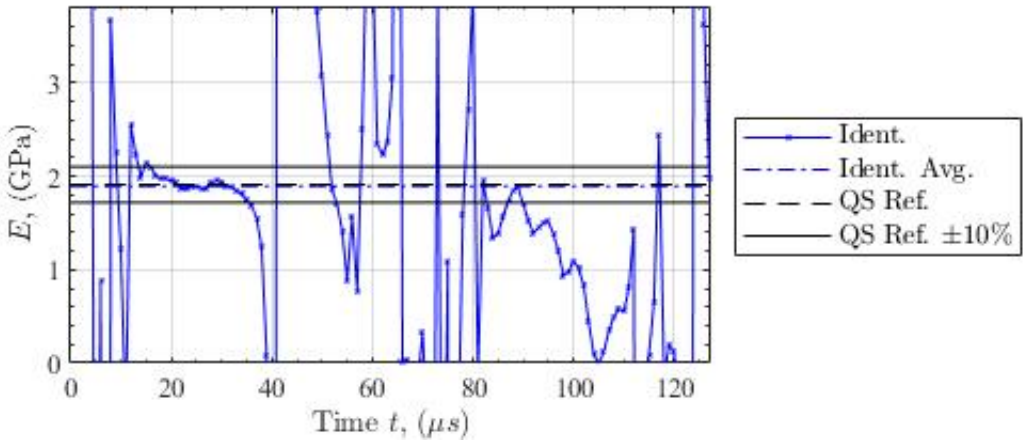

(a)

Figure 5.13: Results obtained for the Young's modulus over time t on RT orientation specimen.

5.4 TR oriented specimen

Similarly to how it was elaborated for the RT orientation specimens, the experimental procedure for the TR orientation specimens was performed. In this experimental analysis, four tests with different specimens were also studied. However, these specimens are 5 mm in dimension on the L axis, 50 mm in the T axis and 30 mm in the R axis, is oriented according to the TR plane shown in figure 3.6. In this section all maps of displacements, accelerations and deformations are presented. For all maps presented below, specimen 1 was selected as a typical representation of all specimens tested in this experimental test.

5.4.1 Results and discussion

Just as it was made in RT oriented specimens, for the analysis of TR oriented specimens, an isotropic model was used in order to identify the constitutive parameters. Like the RT plan, the TR plan also has a low anisotropy ratio.

Figures 5.14 and 5.15 show the maps of the displacements in the x and y components, respectively. In the displacement maps δ_x it can see the one-dimensional wave entering the sample when $t = 20\mu s$ and reflecting on its edge and becoming elastic when $t = 39,5\mu s$. Figures 5.16 and 5.17 show the acceleration maps of the specimen with orientation TR in the components x and y, respectively. The x, xy and y components of the deformations determined on the specimen are shown in figures 5.18, 5.19 and 5.20, respectively. By observing the displacement maps, it is possible to confirm that the magnitude of the deformations in y are significantly smaller than the magnitude of the deformations in xx, as happened in RT oriented specimens. The deformation maps in y show that the signal is noisier than the deformation signal in x. The strain fields clearly show the heterogeneous nature of the IBII test. It is possible to observe that different regions of the material present different amplitude of strain rates. Figure 5.21 shows the comparison maps between the deformations before and after smoothing.

The figures 5.22 and 5.23 show the components of stiffness Q_{xx} and Q_{xy}, respectively, for the TR orientation specimen. In these figures it is observed that it is more to identify the stiffness component Q_{xy} than Q_{xx}, as the signal stabilizes first for Q_{xx} than for Q_{xy}, as happened in RT

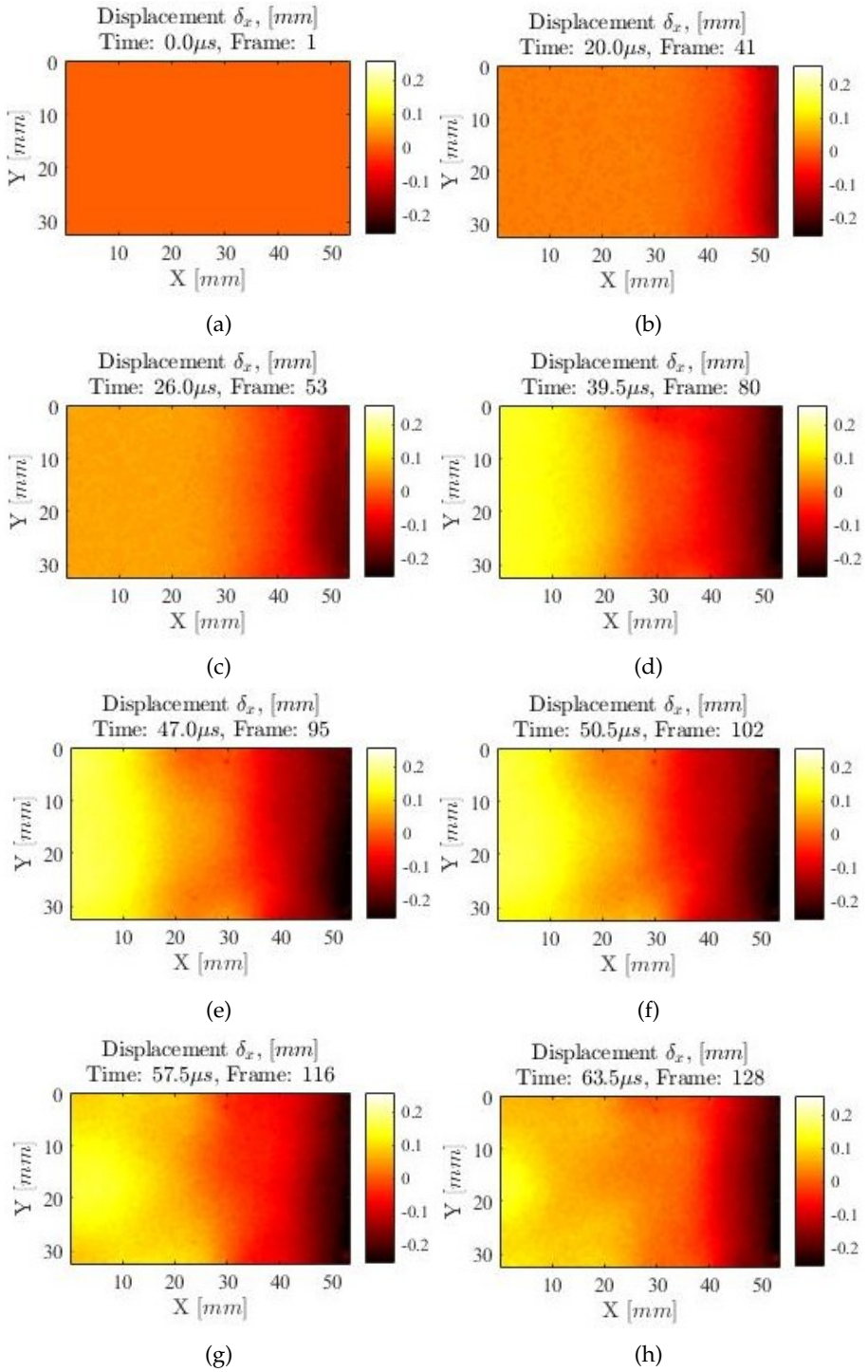

(a) (b) (c) (d) (e) (f) (g) (h)

Figure 5.14: Maps of the x components of the displacements for a specimen with TR orientation at various times. (a) $t = 0\mu s$. (b) $t = 20\mu s$. (c) $t = 26\mu s$. (d) $t = 39\mu s$. (e) $t = 47\mu s$. (f) $t = 50\mu s$. (g) $t = 57,5\mu s$. (h) $t = 63,5\mu s$.

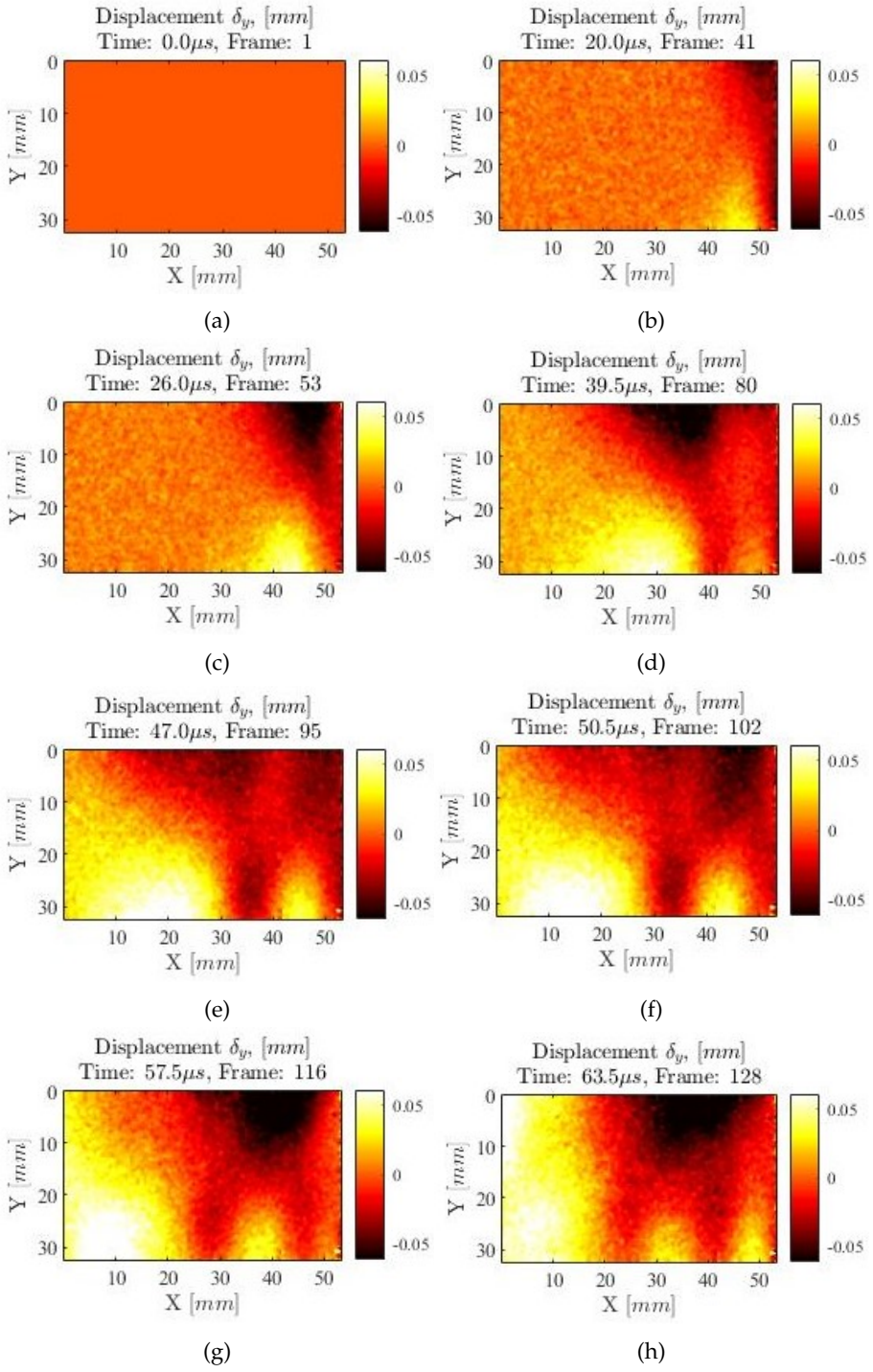

Figure 5.15: Maps of the y components of the displacements for a specimen with TR orientation at various times. (a) $t = 0\mu s$. (b) $t = 20\mu s$. (c) $t = 26\mu s$. (d) $t = 39\mu s$. (e) $t = 47\mu s$. (f) $t = 50\mu s$. (g) $t = 57,5\mu s$. (h) $t = 63,5\mu s$.

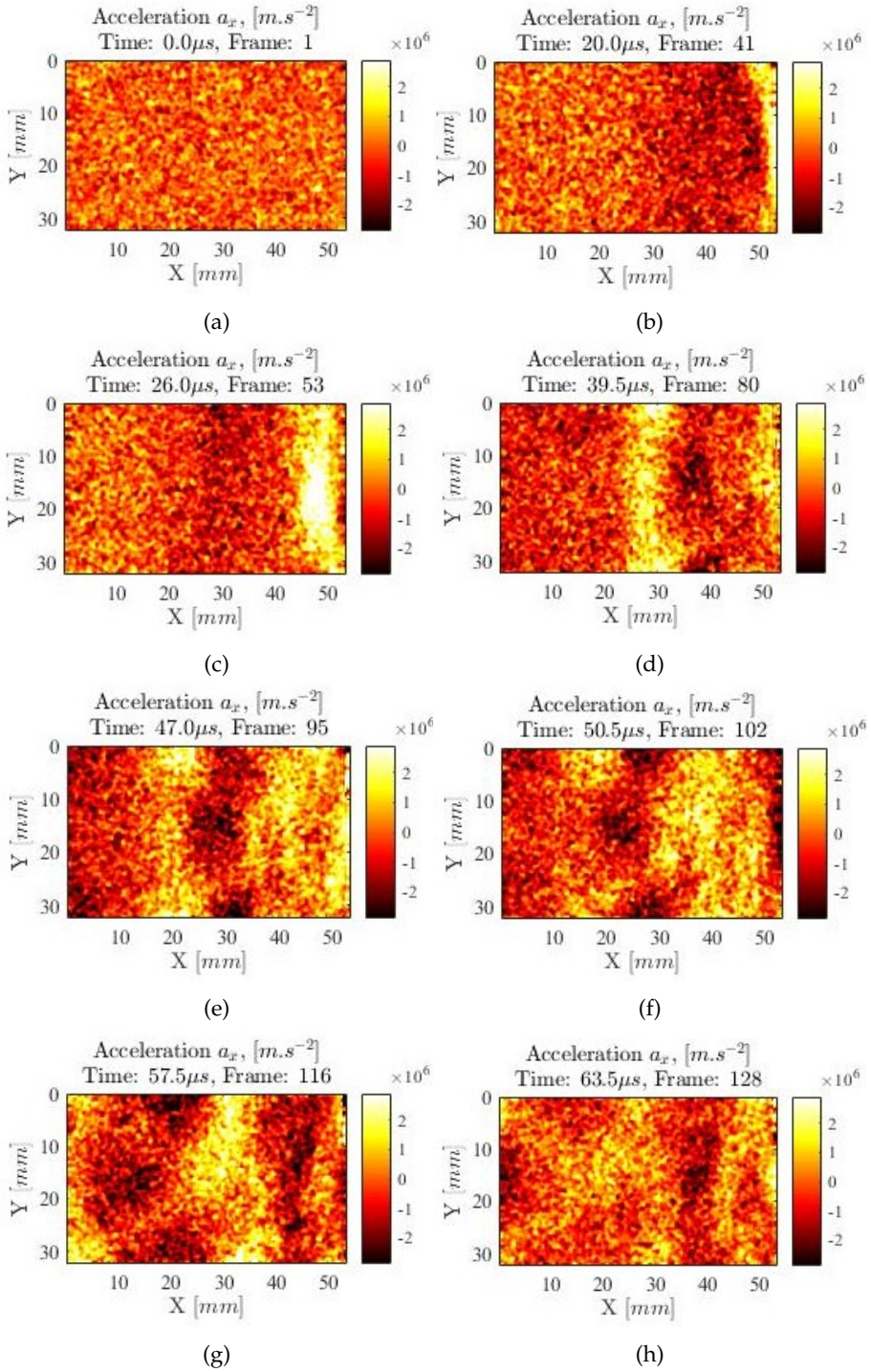

(a) (b) (c) (d) (e) (f) (g) (h)

Figure 5.16: Maps of the x components of the accelerations for a specimen with TR orientation at various times. (a) $t = 0\mu s$. (b) $t = 20\mu s$. (c) $t = 26\mu s$. (d) $t = 39\mu s$. (e) $t = 47\mu s$. (f) $t = 50\mu s$. (g) $t = 57,5\mu s$. (h) $t = 63,5\mu s$.

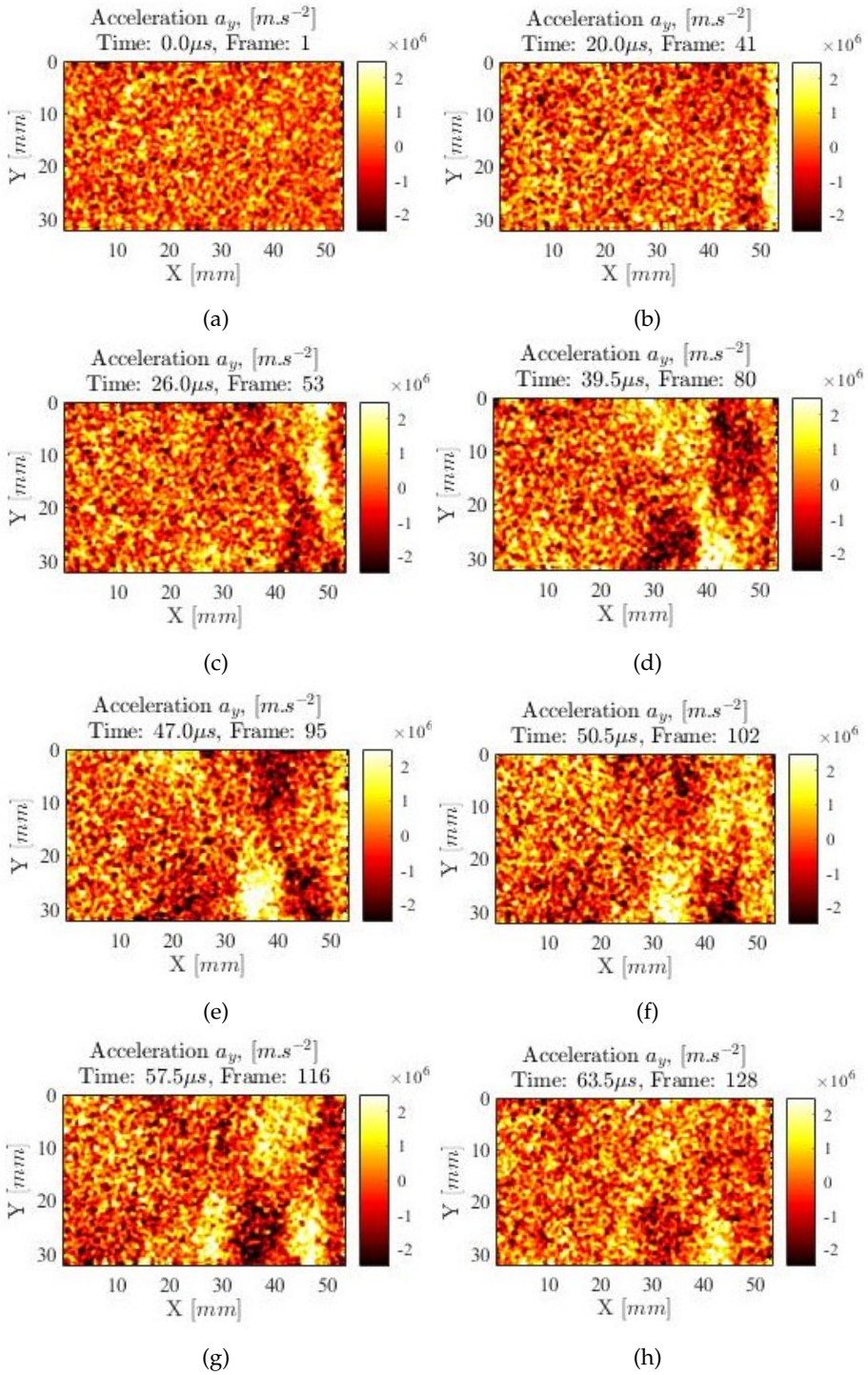

(a) (b) (c) (d) (e) (f) (g) (h)

Figure 5.17: Maps of the y components of the accelerations for a specimen with TR orientation at various times. (a) $t = 0\mu s$. (b) $t = 20\mu s$. (c) $t = 26\mu s$. (d) $t = 39\mu s$. (e) $t = 47\mu s$. (f) $t = 50\mu s$. (g) $t = 57,5\mu s$. (h) $t = 63,5\mu s$.

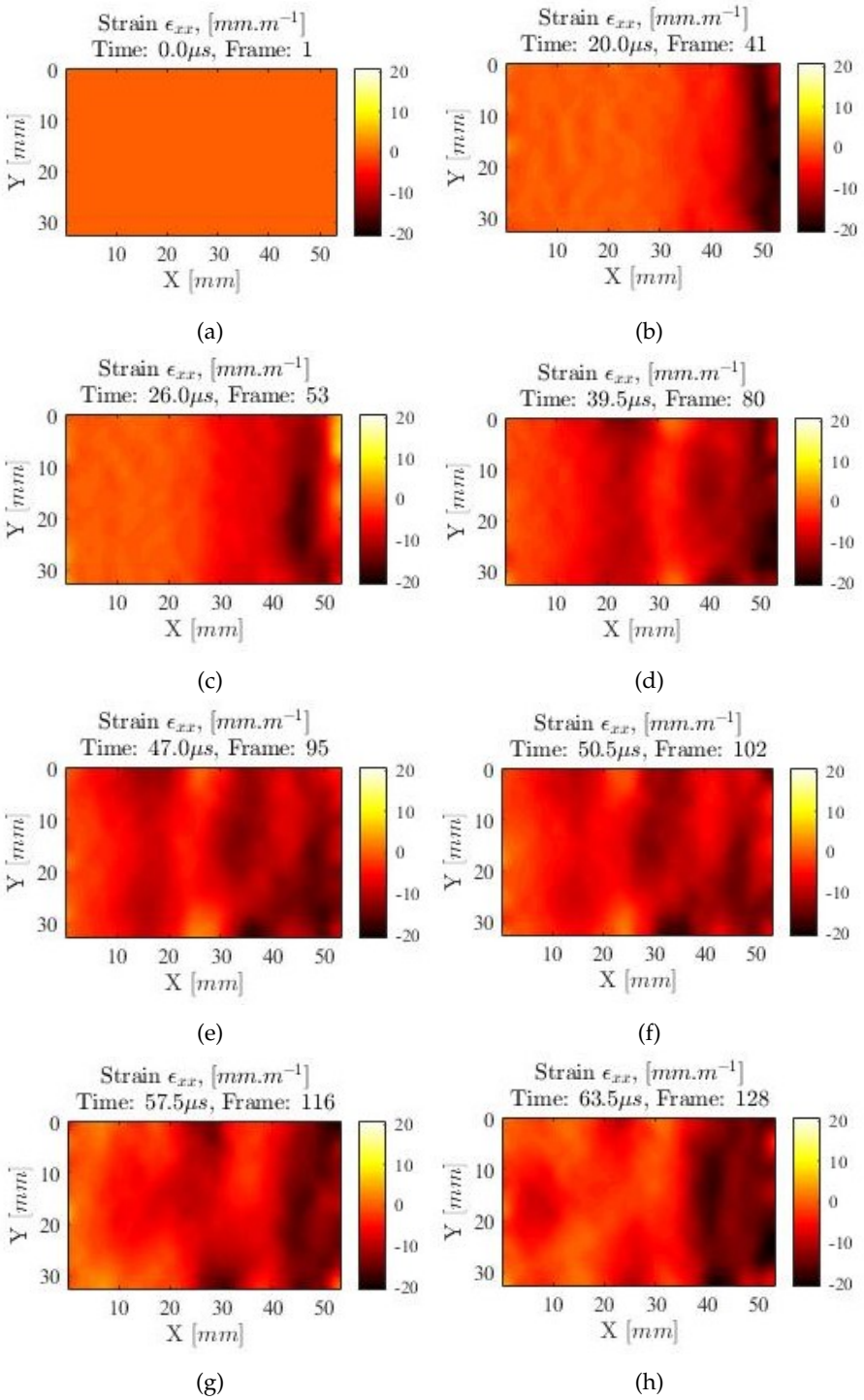

(a) (b) (c) (d) (e) (f) (g) (h)

Figure 5.18: Maps of the x components of the strains for a specimen with TR orientation at various times. (a) $t = 0\mu s$. (b) $t = 20\mu s$. (c) $t = 26\mu s$. (d) $t = 39\mu s$. (e) $t = 47\mu s$. (f) $t = 50\mu s$. (g) $t = 57,5\mu s$. (h) $t = 63,5\mu s$.

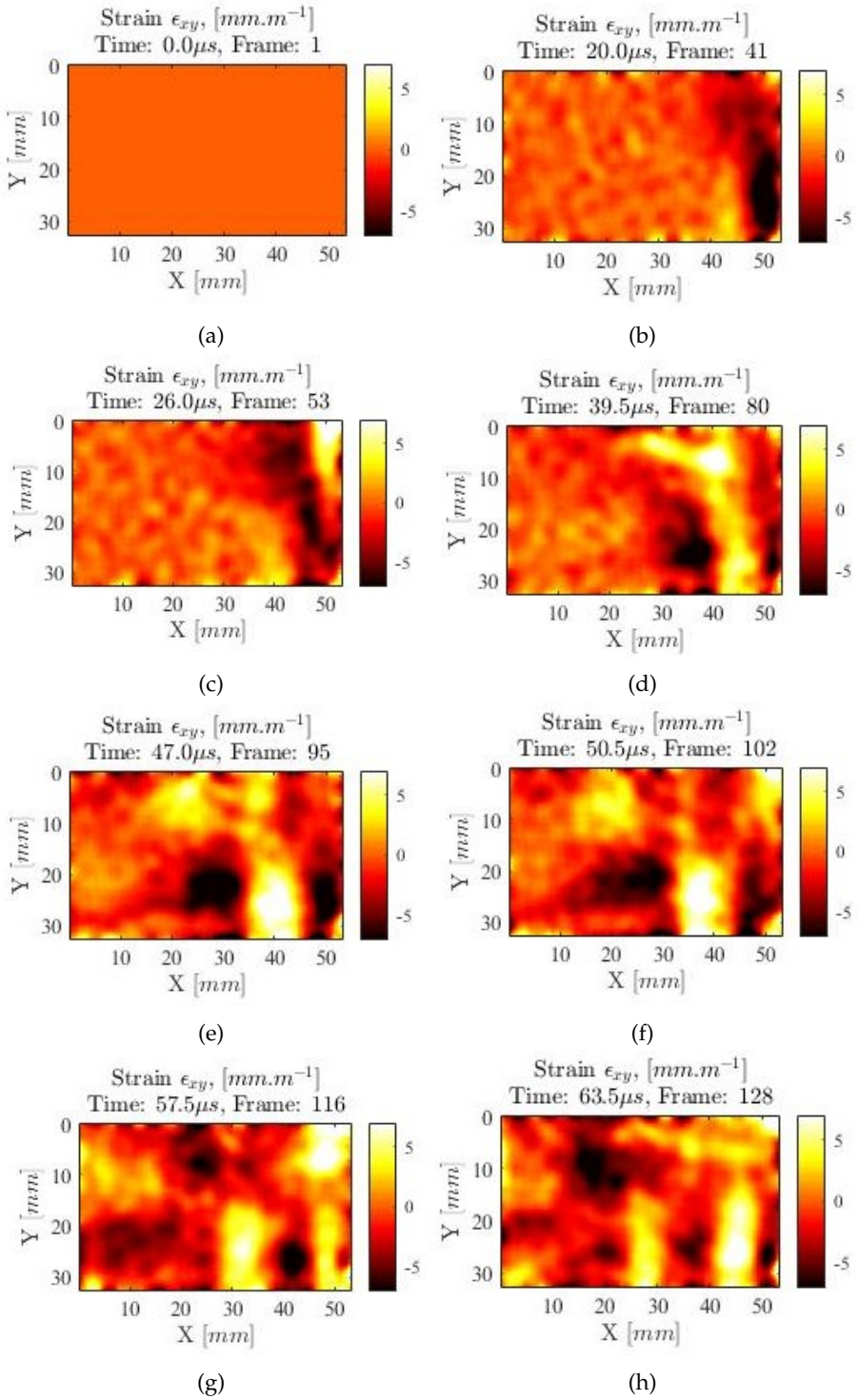

(a) (b) (c) (d) (e) (f) (g) (h)

Figure 5.19: Maps of the xy components of the strains for a specimen with TR orientation at various times. (a) $t = 0\mu s$. (b) $t = 20\mu s$. (c) $t = 26\mu s$. (d) $t = 39\mu s$. (e) $t = 47\mu s$. (f) $t = 50\mu s$. (g) $t = 57,5\mu s$. (h) $t = 63,5\mu s$.

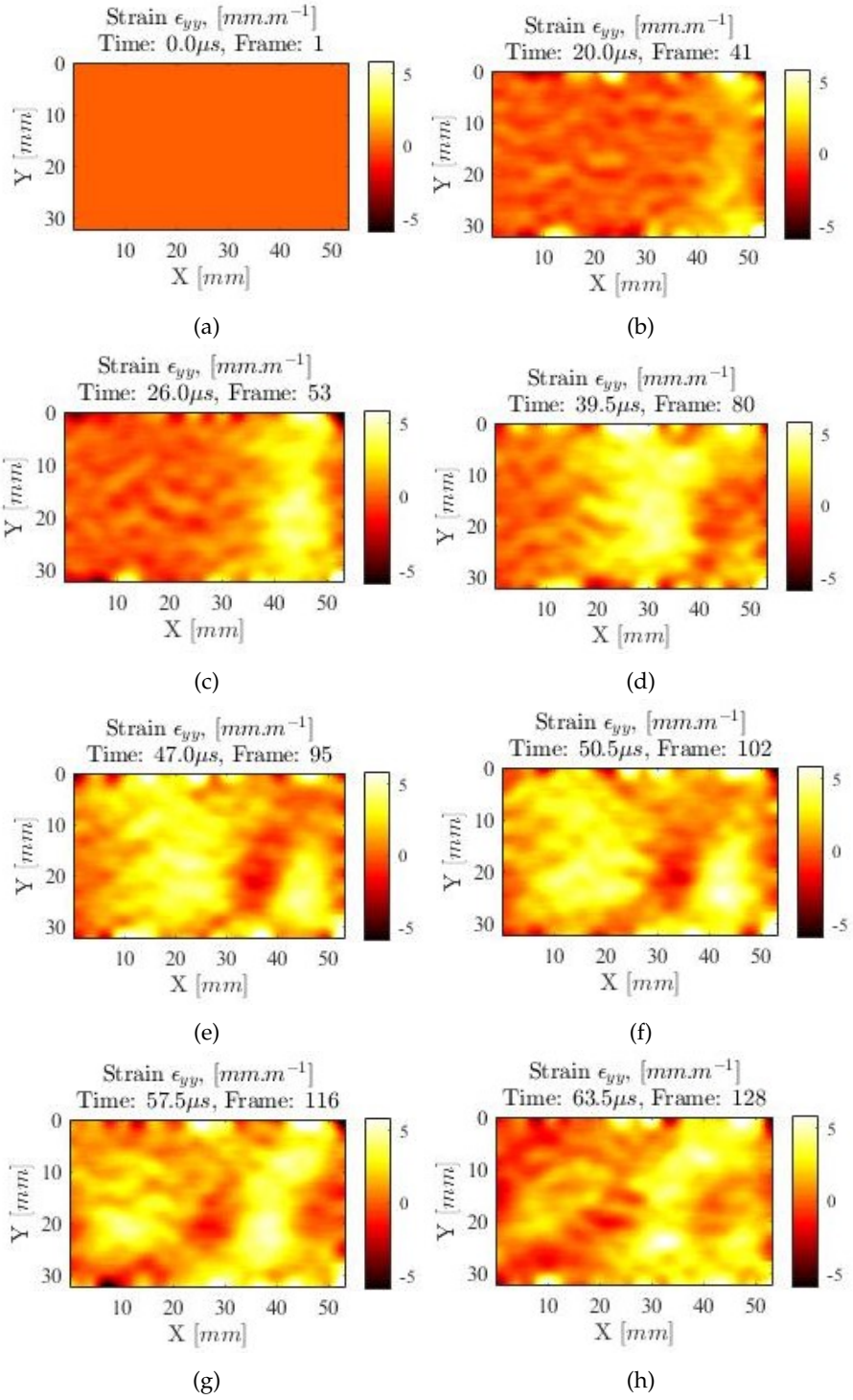

(a) (b) (c) (d) (e) (f) (g) (h)

Figure 5.20: Maps of the y components of the strains for a specimen with TR orientation at various times. (a) $t = 0\mu s$. (b) $t = 20\mu s$. (c) $t = 26\mu s$. (d) $t = 39\mu s$. (e) $t = 47\mu s$. (f) $t = 50\mu s$. (g) $t = 57,5\mu s$. (h) $t = 63,5\mu s$.

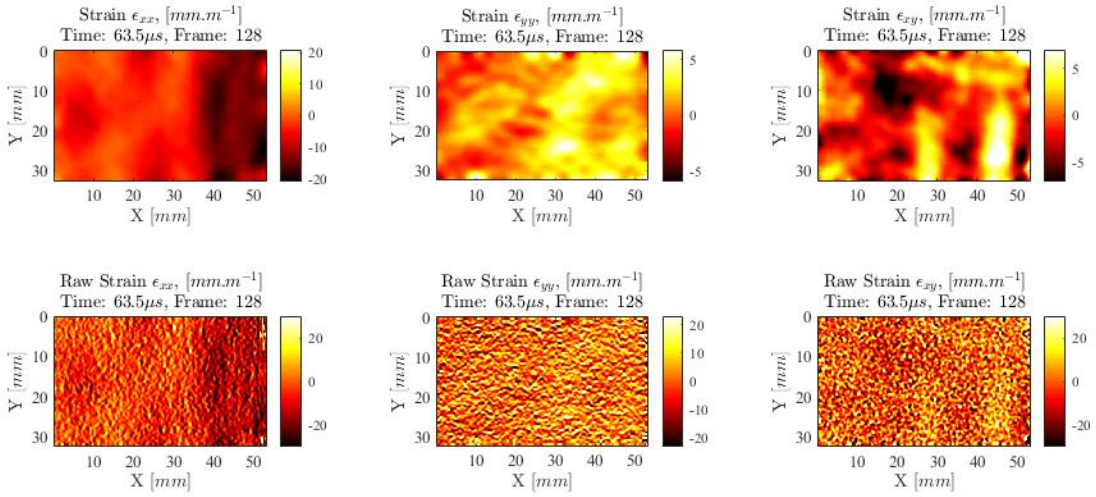

(a)

Figure 5.21: Comparison of deformation cartographies on an TR orientation specimen before and after smoothing at time $t = 180\mu s$.

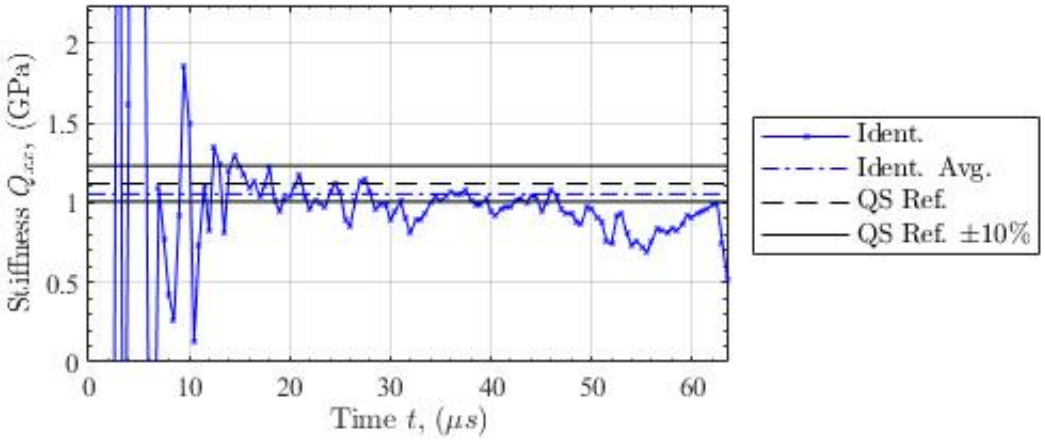

(a)

Figure 5.22: Results obtained for stiffness component Q_{xx} over time t on TR orientation specimen.

oriented specimens. This result happens because the deformation is predominantly axial, having only minor deformations and lateral accelerations.

Taking into account the four test pieces analysed in this TR oriented trial, the average value for the stiffness component Q_{xx} is 0,98 GPa and the average value for the stiffness component Q_{xy} is 0,80 GPa.

In this experimental analysis we used the virtual fields described in equations 5.1 and 5.2, just as they were applied to the experimental test with the specimen oriented to the RT plane.

Table 5.3 shows the mean values of the constitutive parameters determined for the various specimens analysed with the TR orientation. For the TR plane, the values referenced for the Young's modulus (E_T) and the Poisson's ratio (ν_{TR}) are 1,01 GPa and 0,312, respectively. In the time interval under study, the mean value of Young's modulus varies by 10% and the mean

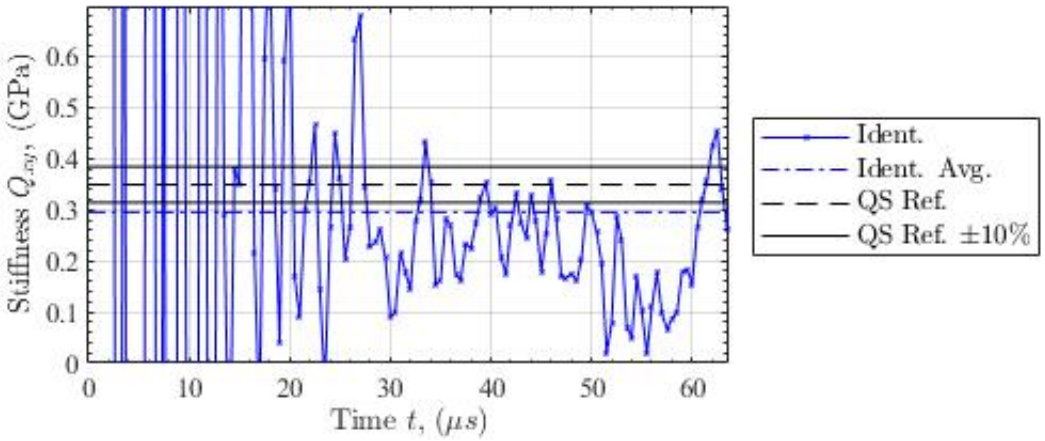

(a)

Figure 5.23: Results obtained for stiffness component Q_{xy} over time t on TR orientation specimen.

Table 5.3: Results obtained for the constitutive parameters of *Pinus pinaster* Ait. wood for different specimens with orientation in the TR plane.

Specimens	Young's modulus (E_R) (GPa)	Poisson's ratio (ν_{RT})
1	0,932	0,290
2	0,713	0,046
3	0,786	0,208
4	0,752	0,191
Average	0,795	0,191
Standard deviation	0,083	0,080
Coefficient of variation	10,0 %	42,1 %

value of the Poisson's ratio varies by 42,105%. The results obtained in this experimental analysis show variations very similar to the variations achieved in the analysis of test pieces with RT orientation. Both results achieved in the two experimental analyses are adequate considering the approximations made, such as the use of an isotropic VFM model to identify the constituent parameters of the material under study, as this TR plan also has a low anisotropy ratio, as was done with the RT plan.

Figures 5.24 and 5.25 show the comparisons between the Young's modulus determined in the experimental analysis as a function of position x and time t, respectively, with its reference value and the calculated mean value.

Figure 5.24 analyses the Young's modulus determined for various x positions of the specimen with its reference value and the calculated mean value. This figure describes that this method only stabilizes approximately $t = 20\mu s$. In the same way as for experimental test with specimens with RT orientation, this occurs because there is a need for sufficient information in the acceleration and deformation fields to be able to identify the constitutive properties of the material, in this case Young's modulus. This identification only happens when a significant portion of the stress wave enters the specimen.In this figure it is also possible to observe, through the signal, the compression and traction that happens in the specimen. In figure 5.25 it is possible to analyse the Young's modulus as a function of time t. In this graph the Young's modulus is compared

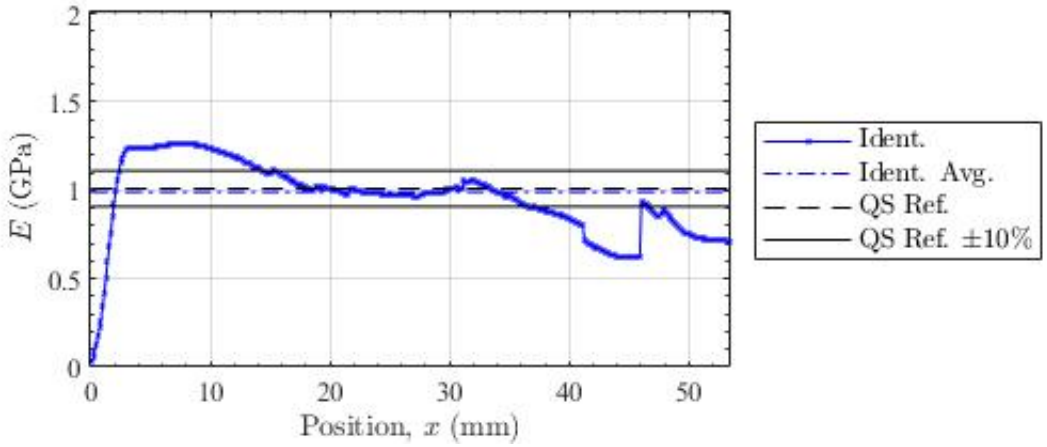

(a)

Figure 5.24: Results obtained for the Young's modulus along x position on TR orientation specimen.

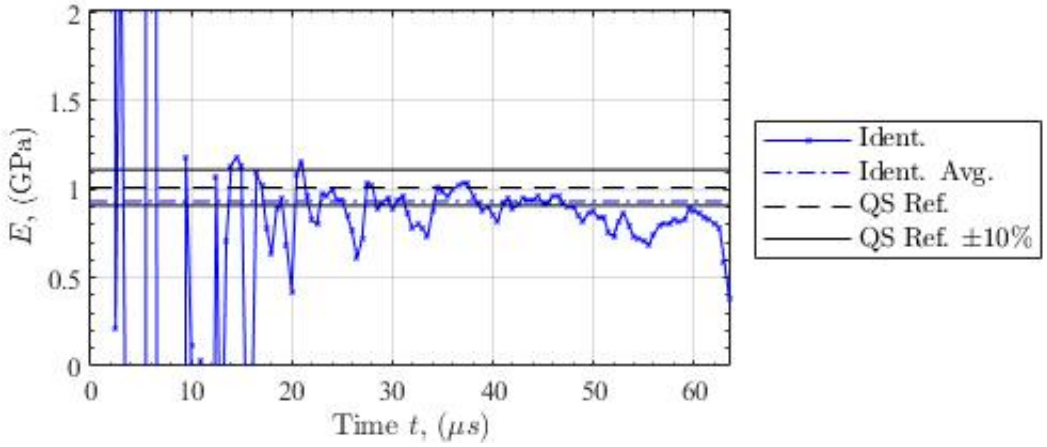

(a)

Figure 5.25: Results obtained for the Young's modulus over time t on TR orientation specimen.

with its reference value and its mean value determined in the experimental analysis.

As stated and concluded for the analysis performed on RT oriented specimens, for this analysis to have a good identification of the constituent properties using an orthotropic model, a more heterogeneous experimental setup would have to be used. Thus, it would be necessary to develop different test configurations to identify all parameters of an orthotropic material in a single experimental test.

In addition to these aspects, the choice of virtual fields has been made according to boundary conditions, may lead to uncertainties regarding the minimization of noise in the experimental test.

5.5 Conclusion

This chapter describe two experimental analysis of the inertial impact test applied to *Pinus pinaster* Ait. wood, when it is subjected to high strain rates, in order to identify the constitutive parameters of the material. The first analysis consists of a specimen oriented according to the *RT* plane and the second analysis consists of a specimen oriented according to the *TR* plane.

First a description of the experimental test was made, with all the characterization of the materials and the dimensions of the components. Then all the results were presented, showing all the maps of the displacements, accelerations and strains calculated for the specimen in the *RT* plane and in the *TR* plan at various times. Finally, several conclusions were drawn about the dynamic test under study and the constitutive properties of wood of *Pinus pinaster* Ait. species when it is subjected to high strain rates.

The results obtained in these experimental analyses confirm the methodology that uses inertial tests to identify the constitutive parameters of materials subjected to high strain rates. Thus, there is no need to measure applied external forces, acceleration is used as the load cell. This is one of the strengths of this methodology, as it is very difficult to measure external forces applied to a specimen. It is possible that this method will revolutionize the way experimental testing of materials at high strain rates. Although there is some work needed to fill in the existing gaps, it is feasible to use this methodology in performing inertial tests.

6 | Conclusions and future work

In this dissertation, a new methodology was studied to address the mechanical behaviour of *Pinus pinaster Ait.* wood, on the transverse (Radial–Tangential) plane, when loaded at high strain rates. In particular, the image-based inertial impact (IBII) test was used to identify the linear elastic constituent parameters. Through this new dynamic test it was possible to overcome some difficulties of other experimental tests, such as the measurement of external forces applied to the specimens. This new methodology enables the use of relatively simple experimental test configurations when compared to other tests such as the split-Hopkinson pressure bar test. Moreover, the restrictive assumptions of quasi-static stress equilibrium (neglecting inertia effects) and 1D wave propagation theory (no dispersion effects) can be relaxed. The inverse material identification approach rely on the Virtual Fields Method (VFM). The identification is fully obtained from full-field measurements using ultra high speed cameras. Displacement, strain and acceleration fields are reconstructed from grid images recorded during the dynamic test. In the IBII test successive images of the specimen deformation were recorded by an ultra high speed camera. Displacement fields are determined by phase-shifting techniques from the grid images. The strain and acceleration fields were obtained afterwords by, respectively, spatial and temporal derivation algorithms. According to the VFM, the proper selection of trial functions enables to write the equilibrium equations of the Principle of Virtual Work, so the material parameters can be extracted directly as a function of image-based measurements. This identification was performed using acceleration fields over the specimen as a load cell, taking into account non-negligible inertial forces during the dynamic test.

The IBII test was validated in this dissertation through the experimental analysis of specimens with orientation RT and TR material planes. The following main conclusions can be drawn from this work:

- This type of experimental test allows the identification of the constitutive parameters of *Pinus pinaster* Ait. wood when subjected to high strain rates, using acceleration as the load cell. The results obtained are very promising since they are in agreement with reference values in the literature.
- Optical techniques, such as the grid method, are an alternative methodology to conventional experimental test methods. With these techniques it is possible to obtain the specimen displacement fields accurately. With the advancement of ultra high speed camera technology, a greater application of these optical techniques in experimental tests has been possible to study materials subjected to high strain rates.
- By applying VFM to the data from the experimental analysis it was possible to identify the stiffness components Q_{xx} and Q_{xy} of the material for the two tests conducted with

specimens oriented on RT and TR material planes. For the RT orientation test, the stiffness components Q_{xx} and Q_{xy} averaged 2.23 GPa and 0.80 GPa, respectively. Similarly, for the TR orientation test, the stiffness components Q_{xx} and Q_{xy} show the average values of 0.98 GPa and 0.80 GPa, respectively.

- The stiffness components can be conveniently written in terms of engineering constants, in particular the modulus of elasticity and the Poisson's ratio. In the RT orientation, the mean values of Young's modulus and Poisson's ratio were 1.909 GPa and 0.596, respectively. Comparing to reference values obtained from quasi-static tests, the dynamic properties presented a variation of 1,571% and a variation of 11,667%, respectively, to the modulus of elasticity and Poisson's ratio. In turn, for the TR specimen orientation, the mean values of Young's modulus and Poisson's ratio were 0.795 GPa and 0.191, respectively. In comparison to reference quasi-static data for this species a variation of 10% and a variation of 42,105% was obtained, respectively, for the dynamic modulus of elasticity and Poisson's ratio. Nevertheless, taking into account the natural variability of wood, it can be concluded that the elastic properties are not significant effected by high strain rate loading for the species and material planes studies in this work.

Although the IBII dynamic test was proven as a current alternative to investigate wood properties at high strain rates, it is important to discuss the limitations that this study presents in order to improve the methodology in the future. Thus, some limitations of the IBII test will be presented, as well as ideas for future work:

- The linear elastic isotropic constitutive material was considered in a first approach to implement the VFM in this analysis. However, the linear elastic orthotropic behaviour could be considered in further analysis.

- In this work, virtual fields were selected by the user as simple mathematical expression of the kinematic fields which were VFM-admissible (*i.e.* they cancel out the contribution of the external virtual work) and respected the prescribed boundary conditions. It was proven however that optimised special virtual fields would lead to a more robust optimisation (Avril et al., 2004c). Therefore, this approach should be considered in further analysis.

- The proposed approach relies on a set of assumption, including that the material is in a plane stress state and density and stiffness are constant through the volume. This assumption can be verified though explicit finite element simulations of the IBII test considering the material heterogeneities at the growth ring level by including physical and mechanical properties of earlywood and latewood tissues.

- To develop a simulation tool to simulate both the measurement and inverse identification methodologies. This virtual tool will allow to address camera effects such as noise, spatial and temporal resolution, and the identifiability of the constitutive parameters. The robustness of the VFM approach is significantly affected by digital camera spatial and temporal resolution factors, the algorithms that are used to reconstruct the strain and acceleration fields from the displacements provided by the optical techniques, as well as, the selected virtual fields for the identification. Errors resulting from measurement and identification chains could be therefore systematically studies.

- For the identification process used in this study, it is assumed that the strain and acceleration fields are uniform across the thickness. Any deviations from the uniform total thickness will generate errors in the identified properties. In the future it will be necessary to perform the experimental tests using two cameras in a consecutive configuration to evaluate the errors generated from the thickness dispersion.
- One of the technologies that can still be improved is the ultra high speed camera technology. This technology can improve by increasing pixel matrices, increasing frame rates and having longer recording times. These characteristics can reduce measurement errors, which will allow more complex experimental tests.
- From an experimental point of view, it would be important to study other planes of material symmetry. The *RT* and *TR* planes of *Pinus pinaster* Ait. wood, considered in this work, have typically a low anisotropic ratio when compared to the longitudinal-transversal (radial or tangential) material planes.
- Since wood is a biological material with a complex structure and its mechanical properties can vary in space, it can be interesting to further address the VFM identification considering a spatial parametrisation for the material properties.

References

Aloui, S., R. Othman, A. Poitou, P. Guégan, and S. El-Borgi (2008). "Non-parametric identification of the non-homogeneous stress in high strain-rate uni-axial experiments." In: *Mechanics Research Communications* 35.6, pp. 392 –397.

Ashby, M. (2005). *Materials Selection in Mechanical Design*. 3rd ed. Butterworth-Heinemann.

Avril, S., E. Ferrier, A. Vautrin, P. Hamelin, and Y. Surrel (2004a). "A full-field optical method for the experimental analysis of reinforced concrete beams repaired with composites." In: *Composites Part A: Applied Science and Manufacturing* 35.7-8, pp. 873–884.

Avril, S., A. Vautrin, and Y. Surrel (2004b). "Grid method: Application to the characterization of cracks." In: *Experimental Mechanics* 36.1, pp. 37–43.

Avril, S., M. Grédiac, and F. Pierron (2004c). "Sensitivity of the virtual fields method to noisy data." In: *Computational Mechanics* 34.6, pp. 439–452.

Bardenheier, R. and G. Rogers (2006). "Dynamic impact testing with servohydraulic testing machines." In: *Journal de Physique IV (Proceedings) France* 134, pp. 693–699.

Blitterswyk, J. V., L. Fletcher, and F. Pierron (2018). "Image-Based Inertial Impact Test for Composite Interlaminar Tensile Properties." In: *Journal of Dynamic Behavior of Materials* 4.4, pp. 543–572.

Carlsson, L., D. Adams, and R. Pipes (2014). *Experimental Characterization of Advanced Composite Materials*. Taylor & Francis.

Chen, W. and B. Song (2011). *Split Hopkinson (Kolsky) Bar. Design, Testing and Applications*. Springer US.

Dinwoodie, J. (2000). *Timber: Its nature and behaviour*. Van Nostrand Reinhold.

Falk, R. H., M. C. Wiemann, and A. Wiedenhoeft (2010). *Wood Handbook - Wood as an Engineering Material*. Centennial Edition.

FAO (2009). *State of the World's Forests–2009. Global demand for wood products.* Pages 62–96.

Fernando Sanz, S. L., E. B. Mário Neves, G. P. Didier Pischedda, J. L. Thierry Gauthier, A. M. Christian Plantier, J. A. S. Jean-Denis Lanvin, F. P. Manuel Touza, D. R. Jacques Parrot, and e. C. Faria (2006). *Industrial Applocations of Pinus Pinaster*. Tech. rep. Centro de Innovación e Servizos Tecnolóxicos da Madeira de Galicia.

Field, J., S. Walley, W. Proud, H. Goldrein, and C. Siviour (2004). "Review of experimental techniques for high rate deformation and shock studies." In: *International Journal of Impact Engineering* 30.7. 5th International Symposium on Impact Engineering, pp. 725 –775.

Fletcher, L. and F. Pierron (2018). "An Image-Based Inertial Impact (IBII) Test for Tungsten Carbide Cermets." In: *Journal of Dynamic Behavior of Materials* 4.4, pp. 481–504.

Fletcher, L., J. Van-Blitterswyk, and F. Pierron (2019). "A Novel Image-Based Inertial Impact Test (IBII) for the Transverse Properties of Composites at High Strain Rates." In: *Journal of Dynamic Behavior of Materials* 5.1, pp. 65–92.

García-Iruela, A., L. Esteban, P. de Palacios, F. García-Fernández, Álvaro de Miguel Torres, E. V. Iriarte, and C. Simón (2016). "Resinous Wood of Pinus pinaster Ait.: Physico-mechanical Properties." In: *BioResources* 11.2, pp. 5230–5241.

Garrido, N. (2004). "Identificação do comportamento ao corte da madeira através do ensaio de tração fora dos eixos de simetria." Master's thesis. Universidade de Trás-os-Montes e Alto Douro.

Gibson, L. J. and M. F. Ashby (1999). *Cellular Solids. Structure and Properties*. Cambridge University Press.

Grédiac, M., F. Pierron, S. Avril, and E. Toussaint (2006). "The Virtual Fields Method for Extracting Constitutive Parameters From Full-Field Measurements: a Review." In: *Strain* 42.4, pp. 233–253.

Grédiac, M., F. Sur, and B. Blaysat (2016). "The grid method for in-plane displacement and strain measurement: A review and analysis." In: *Strain* 52.3, pp. 205–243.

Grediac, M, F Sur, and B Blaysat (2018). *The Grid Method*. URL: http://www.thegridmethod.net/home (visited on 01/13/2019).

Green, A. (1983). "Computer-aided engineering. CAE in historical perspective." In: *Electronics and Power* 29.1, p. 81.

Koerber, H., J. Xavier, and P. Camanho (2010). "High strain rate characterisation of unidirectional carbon-epoxy IM7-8552 in transverse compression and in-plane shear using digital image correlation." In: *Mechanics of Materials* 42.11, pp. 1004–1019.

Kollman, F. and W. Côté Jr. (1984). *Principles of wood science and technology – Solid wood*. Springer-Verlag, Berlin.

Kollmann, F. F. P. and W. Côté (1968). *Principles of Wood Science and Technology Solid Wood*. Springer New York.

Kondo, Y., K. Takubo, H. Tominaga, R. Hirose, N. Tokuoka, Y. Kawaguchi, Y. Takaie, A. Ozaki, S. Nakaya, F. Yano, and T. Daigen (2013). "Development of " HyperVision HPV-X " High-speed Video Camera." In:

Lecompte, D, A Smits, S Bossuyt, H Sol, J Vantomme, D. V. Hemelrijck, and A. M. Habraken (2006). "Quality assessment of speckle patterns for digital image correlation." In: *Optics and Lasers in Engineering* 44.11, pp. 1132–1145.

Lewin, M. and I. Goldstein (1991). *Wood structure and composition*. International Fiber Science and Technology Series, Vol. 11.

Longana, M. L. (2014). "Intermediate strain rate testing methodologies and full-field optical strain measurement techniques for composite materials characterisation." Doctoral dissertation. University of Southampton.

Meyers, M. (2007). *Dynamic Behavior of Materials*. John Wiley & Sons, Ltd.

Pereira, J., J. Xavier, J. Morais, and J. Lousada (2014). "Assessing wood quality by spatial variation of elastic properties within the stem: case study of P. pinaster in the transverse plane." In: *Canadian Journal of Forest Research* 44.2, pp. 107–117.

Pereira, J. (2013). "Assessing wood quality by spatial variability of transverse elastic properties within the stem: Case study on P. pinaster at the meso scale." Doctoral dissertation. University of Beira Interior, Covilhã, Portugal.

Pierron, F. and P. Forquin (2012). "Ultra-High-Speed Full-Field Deformation Measurements on Concrete Spalling Specimens and Stiffness Identification with the Virtual Fields Method." In: *Strain* 48.5, pp. 388–405.

Pierron, F. and M. Grédiac (2012). *The Virtual Fields Method: Extracting Constitutive Mechanical Parameters from Full-field Deformation Measurements*. Springer New York.

Pierron, F., M. Sutton, and V. Tiwari (2011). "Ultra High Speed DIC and Virtual Fields Method Analysis of a Three Point Bending Impact Test on an Aluminium Bar." In: *Experimental Mechanics* 51.4, pp. 537–563.

Pierron, F, H Zhu, and C Siviour (2014). "Beyond Hopkinson' s bar Subject Areas." In: *Philosophical Transactions of the Royal Society A: Mathematical, Physical and Engineering Sciences*.

Polocoser, T, B Kasal, and F Stöckel (2017). "State-of-the-art: intermediate and high strain rate testing of solid wood." In: *Wood Science and Technology*, pp. 1479–1534.

Ramesh, K. (2008). "High Rates and Impact Experiments." In: *Springer Handbook of Experimental Solid Mechanics*. Ed. by W. Sharpe. Boston, MA: Springer US, pp. 929–960.

Reu, P. L. (Sept. 2011). "High/Ultra-High Speed Imaging as a Diagnostic Tool." In: *Advances in Experimental Mechanics VIII*. Vol. 70. Applied Mechanics and Materials. Trans Tech Publications Ltd, pp. 69–74.

Reu, P. and T. Miller (2008). "The application of high-speed digital image correlation." In: *The Journal of Strain Analysis for Engineering Design* 43.8, pp. 673–688.

Rossi, M. and F. Pierron (2012). "International Journal of Solids and Structures On the use of simulated experiments in designing tests for material characterization from full-field measurements." In: *International Journal of Solids and Structures* 49.3-4, pp. 420–435.

Sanz, Fernando Latour, S., M. Neves, E. Bastet, D. Pischedda, G. Piñeiro, T. Gauthier, J. Lesbats, C. Plantier, A. Marques, J.-D. Lanvin, J. A. Santos, M. Touza, F. Pedras, J. Parrot, D. Reuling, and C. Faria (2006). "Aplicações Industriais do Pinheiro Bravo." In: *CIS Madeira*.

SIEMENS (2018). *Computer-Aided Engineering*. URL: https://www.plm.automation.siemens.com/global/cz/our-story/glossary/computer-aided-engineering-cae/13112 (visited on 01/13/2019).

Smith, I., E. Landis, and M. Gong (2003). *Fracture and fatigue in wood*. John Wiley and Sons.

Sudheera, Y. Rammohan, and M. Pradeep (2018). "Split Hopkinson Pressure Bar Apparatus for Compression Testing: A Review." In: *Materials Today: Proceedings* 5.1, Part 3. International Conference on Advanced Materials and Applications (ICAMA 2016), June 15-17, 2016, Bengaluru, Karanataka, INDIA, pp. 2824 –2829.

Teixeira-Dias, F., J. P. da Cruz, R. F. Valente, and R. A. de Sousa (2018). *Método dos Elementos Finitos: Técnicas de Simulção Numérica em Engenharia*. Lisboa: ETEP.

Xavier, J. (2003). "Caracterização do comportamento ao corte da madeira usando o ensaio de Iosipescu." Master's thesis. Universidade de Trás-os-Montes e Alto Douro.

— (2007). "Characterisation of the wood stiffness variability within the stem by the virtual fields method: application to *P. pinaster* in the *LR* plane." Doctoral dissertation. Art et Métiers ParisTech Châlons-en-Champagne.

Yuan, F., V. Prakash, and J. J. Lewandowski (2007). "Spall strength and Hugoniot elastic limit of a zirconium-based bulk metallic glass under planar shock compression Spall strength and Hugoniot elastic limit of a zirconium-based bulk metallic glass under planar shock compression." In: *Journal of Materials Research* 22.February, pp. 402–411.

Zhu, H. (2015). "A Novel Methodology for High Strain Rate Testing Using Full-field Measurements and the Virtual Fields Haibin." Doctoral dissertation. Université de Technologie de Troyes.

Zhu, H. and F. Pierron (2016). "Exploration of Saint-Venant's Principle in Inertial High Strain Rate Testing of Materials." In: *Experimental Mechanics* 56.1, pp. 3–23.